ISSN 1726-5479

SENSORS & TRANSDUCERS

vol. 213
6 /17

Electronic version. Not for distribution.

Nanosensors, Chemical Sensors and Sensor Networks

International Frequency Sensor Association Publishing
IFSA

Sensors & Transducers

International Official Open Access Journal of the International Frequency Sensor Association (IFSA) Devoted to Research and Development of Sensors and Transducers

Volume 213, Issue 6, June 2017

IFSA Publishing: Barcelona • Toronto

Published by International Frequency Sensor Association (IFSA) Publishing. Printed in the USA.

Sensors & Transducers

Volume 213, Issue 6,
June 2017

www.sensorsportal.com

e-ISSN 1726-5479
ISSN 2306-8515

Sensors & Transducers journal is an open access, peer review international journal published monthly by International Frequency Sensor Association (IFSA).
Available in both: print and electronic (printable pdf) formats.

Sensors & Transducers Journal

Contents

Volume 213
Issue 6
June 2017

www.sensorsportal.com

ISSN 2306-8515
e-ISSN 1726-5479

Research Articles

Sensor Node Deployment Approach in Wireless Sensor Network Based on Multi-objective Flower Pollination Algorithm
Faten Hajjej, Ridha Ejbali and Mourad Zaied 1

Deployment Strategies and Clustering Protocols Efficiency
Chérif Diallo 9

E-nose and E-tongue: an Analytical Tool for Quality Control and Management in the Pet Food Industry
Federica Cheli, Valentino Bontempo and Vittorio Dell'Orto 24

Comparative Analysis of Shift Registers in Different Nanometer Technologies
Rajesh Mehra, Ayushi Gagneja and Priya Kaushal 30

Study of Propylene Glycol, Dimethylformamideand Formaldehyde Vapors Sensors Basedon MWCNTs/SnO_2 Nanocomposites
Zaven Adamyan, Artak Sayunts, Vladimir Aroutiounian,Emma Khachaturyan, Arsen Adamyan, Martin Vrnata,Přemysl Fitl and Jan Vlček 38

Nanostructured Sensors for Detection of Hydrogen Peroxide Vapours
Vladimir Aroutiounian, Valeri Arakelyan, Mikayel Aleksanyan, Artak Sayunts, Gohar Shahnazaryan, Petr Kacer, Pavel Picha, Jiri Kovarik, Jakub Pekarek and Berndt Joost 46

Development of Quantum Dot-based Nanobiosensors against Citrus Tristeza Virus (CTV)
Mohammad Reza Safarnejad, Fatemeh Samiee, Meisam Tabatabie and Afshin Mohsenifar 54

Implantable Medical Device for Measuring Electrocardiogram to Improve Human Wellness
Jong-Ha Lee 61

Authors are encouraged to submit article in MS Word (doc) and Acrobat (pdf) formats
by e-mail: editor@sensorsportal.com. Please visit journal's webpage with preparation instructions:
http://www.sensorsportal.com/HTML/DIGEST/Submition.htm

International Frequency Sensor Association (IFSA).

Sensors & Transducers
Published by IFSA Publishing, S. L., 2017
http://www.sensorsportal.com

Sensor Node Deployment Approach in Wireless Sensor Network Based on Multi-objective Flower Pollination Algorithm

Faten Hajjej, Ridha Ejbali and Mourad Zaied
Research Team in Intelligent Machines (RTIM),
Omar Ibn El Khattab Street, Zrig Eddakhlania, 6072, Gabes, Tunisia
E-mail: hajjej.faten.tn@ieee.org, ridha_ejbali@ieee.org, mourad.zaied@ieee.org

Received: 5 May 2017 /Accepted: 5 June 2017 /Published: 30 June 2017

Abstract: Wireless Sensor Network (WSN) is one of the most dominant technology trends in the upcoming decades. Due to the lack of communication infrastructure, designing a WSN has posed a real challenge to the designers. WSNs should capture information from the environment, acquired, receive and retransmit them while having enough lifetime to reach many decades without external intervention. Thus, optimizing some objective functions, like energy consumption and coverage at the levels of nodes deployment is required to enhance the performances. In this work, deployment issue has been modeled as a constrained multi-objective optimization (MOO) problem. The aim of this work was to find the optimal sensor nodes positions in the area of interest in terms of coverage, energy consumption and network connectivity. A new multi-objective optimization approach based on Flower Pollination Algorithm (FPA) was introduced. The simulation results show that the proposed approach improve both coverage and energy consumption compared with other multi objective approaches.

Keywords: WSN, Deployment problem, Multi objective optimization, Energy consumption, FPA.

1. Introduction

Over the last few decades, fields of microelectronics, micromechanics and wireless communication technologies have made a noticeable progress that allows the production of cost-effective components of a few cubic millimeters in volume. Therefore, wireless sensor networks (WSNs) have arisen as a new area of research to provide more economical solutions, an easy to deploy remote monitoring and processing of data in complex environments. WSNs consist of a large number of nodes deployed in a region of interest (RoI) to collect and transmit environmental data to one or more collection points autonomously. These networks are of interest especially for military applications, environmental applications, home automation, medical and many of the applications related to the surveillance of critical infrastructure. These applications often require a high level of security and characteristics sharing because of the lack of infrastructure, limited energy and dynamic topology. Sensor nodes have limited resources, namely the energy resources and the calculation capabilities as well as the storage capacity. Thus, most studies and researches on WSN have dealt with resources optimization problems in order to enhance the performances and meet the quality of service (QoS) requirements.

The deployment of a sensor in the RoI is a crucial issue for any WSN designers especially with the limitations of sensor nodes. In fact, WSN performances are greatly influenced by the placement strategies since they directly affect QoS metrics, such as energy consumption, sensor lifetime and sensing coverage equally [1]. Hence, a powerful sensor deployment strategy will obviously improve performance and resource management. The deployment strategies can be classified according to three criteria: the first is the placement methodology that can be either random placement or grid-based placement (deterministic placement).the second is the optimization of performance metrics such as connectivity, sensing coverage, energy consumption and lifetime. Finally, the roles the deployed node, which can be regular, relay, cluster-head, or base-station plays [2]. The placement techniques can be further categorized into static and dynamic according to whether the optimization is performed at the time of deployment or when the network is working, respectively. The choice of the deployment schema depends on many properties [2].

The coverage problem is one of the most basic issues in wireless sensor networks, it directly affects the capability and the performances of the sensor network [3]. The quality of coverage is immediately influenced by the choice of the deployment strategy. Most of the applications using WSN, especially those requiring permanent measurements collection, demand a low-energy consuming network. Also, for the sensors network itself, energy consumption is a critical issue since sensor nodes rely on limited power resources. As a result, an optimal deployment topology should achieve a trade-offs between the coverage requirement and the energy constraint. In general, there exist conflicts between minimizing energy dissipation and maximizing coverage. To maximize the area of coverage, sensor nodes must be placed far away from the sink node (data collection point) which means that the sensor signals need higher power in order to reach farther distances. Multi-objective optimization approaches (MOOAs) are generally used to solve optimization problems with conflicting objectives. The multi-objective optimization (MOO) works on several objective function vectors simultaneously. Unlike, the single-objective optimization, the solution of MOO is a set of solutions, known as the set of Pareto optimal solutions [4].

The connectivity metric in WSN is satisfied if, and only if, there exists at least one path between each pair of nodes. This requirement is at the same level of importance with the coverage requirement. Actually, these two metrics should be strongly related in order to ensure wider monitored area without connectivity holes.

Nature constantly inspires research in the field of optimization. While genetics, ants and particle swarm algorithms are famous examples, other nature inspired optimization algorithms emerge regularly. Flower Pollination Algorithm (FPA) is a novel global optimization algorithm inspired from pollination process of flowers. FPA is simple and very powerful; in fact, it can outperform both genetic algorithm (GA) and particle swarm optimization (PSO) according to [5].

In this work, we proposed a new deployment approach based on the multi objective version for FPA (MOFPA) [6] for WSN. Our approach aimed to find the optimal deployment topology taking into account the aforementioned objectives, i.e., minimizing energy consumption and maximizing total coverage while maintaining connectivity constraints.

The remainder of this paper is organized as follows. In Section 2, the related work is outlined. The problem formulation is presented in Section 3. Section 4 introduces the proposed approach. In Section 5, simulation results and discussion are given. Finally, Section 6 concludes the paper.

2. Related Work

Over the last years, the published approaches related to nodes deployment for WSN attempted to tackle this problem through mathematical programming and nature-inspired algorithm. A node placement approach based on genetic algorithm (GA) with new normalization method was proposed in [7]. The proposed approach used the Monte Carlo method to design the evaluation function in order to maximize coverage area for WSN with lower computation time compared with random deployment [7]. The authors in [8] proposed an improved version of Artificial Bee Colony algorithm to maximize the coverage rate in WSN. This algorithm modified the updating equation of onlooker bee and scout bee. In fact, some new parameters, such as forgetting, neighbor factor and probability of mutant were introduced to enhance coverage rate and accelerate the convergence speed.

Sengupta, *et al.* [9] achieved an optimal trade-offs between coverage, energy consumption and lifetime in WSN using the multi-objective evolutionary algorithm (MOEA). They developed an enhanced version of Multi-objective evolutionary algorithm based on differential evolution (MOEA/D-DE) known as MOEA/DFD, which includes the fuzzy dominance. The authors in [10] proposed three algorithms, specifically integer linear programming models, a local search algorithm and a genetic algorithm in order to solve the deployment problems of WSNs. Theirs approaches aimed at finding the optimal deployment in terms of area of coverage and number of wireless sensor nodes by taking into account the connectivity constraint. Likewise, they compared the three models with some regular sensor deployment patterns. The problem of the probability node deployment is less important than the distribution of the asymmetrical nodes.

In [11], the authors tackled the problem of coverage holes for mobile WSN. Their algorithm named, Holes detection and healing (HEAL), run in two steps. The first step consisted in the detection of coverage holes characteristics like the center position using Gabrial Graph of the WSN, geometric form and size. In the second step, the authors seek the best target mobile sensors in term of mobility and messaging cost in order to be re-deployed in the detected coverage holes.

Abo-Zahhad, *et al.* presented a centralized node deployment algorithm that uses the multi-objective approach based on immune algorithm and the Voronoi Diagram in order to find an optimal nodes placement topology in terms of both coverage and energy consumption for WSN. The authors used two different sensing models. The first is based on binary model. The second is based on probabilistic models [12]. Ni, *et al.* enhanced the QoS of mobile WSN while finding the optimal positions of sensor nodes in the RoI. The authors presented a dynamic multi-objective approach based on PSO to optimize both of coverage rate and moving distance of mobile nodes [13]. The authors in [14] proposed three algorithms, specifically integer linear programming models, a local search algorithm and a genetic algorithm in order to solve the deployment problems of WSNs. Theirs approaches aimed at finding the optimal deployment in terms of area of coverage and number of wireless sensor nodes by taking into account the connectivity constraint. Likewise, they compared the three models with some regular sensor deployment patterns. Zhang, *et al.* [15] addressed the sensor nodes deployment issues for Directional Sensor Networks (DSNs). They proposed a novel placement approach based on PSO in order to enhance the coverage probability of the monitoring field. The probability coverage model was adapted as a sensing model.

Table 1 provides a summary of related works to the deployment optimization problem in WSN.

3. Problem Formulation

Considering the severe resources constraints of sensor nodes and the levels of QoS required for the WSNs, an optimal placement process has to be considered. In this work, we aimed at finding the coordinates of the sensor nodes in a two−dimensional sensing area that insure the maximal coverage rate and minimal energy dissipation. The deployed sensors should be connected in an efficient way so that each deployed sensor can find a connection path to reach the sink node. Consequently, our deployment problem was modeled as a multi-objective optimization problem with two objective functions, namely total coverage ratio and energy consumption, and one problem constraint, namely the network connectivity.

3.1. Preliminary Definitions

Sensor nodes in WSN are characterized by their positions in the 2D plane (x, y), sensing radius Rs and communication radius Rc. Given a multi-hop WSN, where all nodes collaborate in order to ensure cooperative communication such network, can be defined as a linked graph, G = {V, E}, where V is the set of vertices representing sensors and E is the set of edges representing links between the sensors. Let u ϵ V and v ϵ V, (u, v) belongs to E if, and only if, u can directly send a message to v (we say that v is neighbor of u).

Table 1. Summary of related work.

Refe-rence	Placement methodology	Objective function
[7]	Genetic algorithm	Coverage
[8]	Artificial bee colony	Coverage & Convergence speed
[9]	Multi-objective evolutionary algorithm & Decomposition	Coverage & Energy consumption & Lifetime
[10]	Integer linear programming models & Local search algorithm & Genetic algorithm	Coverage & Number of sensor nodes
[11]	Virtual forces-based local healing approach	Coverage
[12]	Immune algorithm & Voronoi diagram	Coverage Energy consumption
[13]	Particle swarm optimization	Coverage Moving distance
[14]	Integer linear programming models & Local search algorithm & Genetic algorithm	Coverage Number of wireless sensors nodes
[15]	Particle swarm optimization	Coverage

We assume that Rc is identical for all nodes. Let d(u, v) be the distance between the nodes u and v, the set E can be defined as follows:

$$E = \left\{ (u,v) \in V^2; \quad \mathrm{d(u,v)} \le \mathrm{R}_c \right\} \tag{1}$$

The network coverage is defined by the sensing radius of the sensor node, whereas the network connectivity is specified by the communication radius of the nodes.

3.2. Multi Objective Optimization

Formulating an optimization problem as a multi objective problem is necessary in some cases, especially when the problem involves more than one objective functions and several constraints. The objective functions are typically conflicting; the task of MOOA is to find a trade-offs between the conflicted objectives. Unlike single-objective problem optimization, the results of MOOA are usually a set of solutions [4].

Definition 1. Multi-objective optimization problem.

A multi-objective optimization problem is a problem of the following form:

$$\begin{cases} \text{Minimize / Maximize } f(x) = \left[f_1(x),\ f_2(x),\ \ldots f_n\right], \\ \text{Subject to } q_j(x) \geq 0, \quad j = 1, 2, \ldots, m, \\ h_d(x) = 0, \quad d = 1, 2, \ldots, l, \end{cases} \tag{2}$$

where x ϵ E_n is the decision variables, n is the number of objective functions, l is the number of equality constraints and m is the number of inequality constraints [4].

Definition 2. Pareto optimality.

MOO problem has actually many solutions in the feasible region that all fit a predetermined definition for an optimum solution [16]. The predominant concept in defining an optimal point is that of Pareto optimality. This is specified as follows:

A point, y* ϵ Y, is Pareto optimal if there is not another solution point y ϵ Y, such that f(y) ≤ f(y*) for at least one function [4].

Definition 3. Non-dominated solution.

A feasible solution is non-dominated if there is not another feasible solution better than the current one in some objective function [4, 17].

3.3. Energy Model

The energy consumed by WSN is considered as the first objective function. Here, our purpose was to minimize the total energy consumed by the network. Supposing that E0 is the initial energy capacity for each sensor and e_i is the energy consumed by each node i, e_i can be formulated as follows:

$$e_i = ME_i + TE_i \times P_{si} + RE_i \times \alpha_i, \tag{3}$$

where MEi is the maintenance energy, TEi is the transmission energy, Psi refers to the cost of minimum path from a sensor node i to the sink node, REi is the reception energy and αi represents the number of sensors in which node i receives data and transfers it to the sink node in multi-hop communication.

The network total energy consumed is defined as the sum of the energy consumed by each node. So, our first objective function is given as follows:

$$f_1 = \text{Minimize}\left(\sum_{i=1}^{N_s} e_i\right), \tag{4}$$

where N is the number of sensor nodes.

3.4. Coverage Model

Coverage in WSN can be defined as the total area covered by a collection of sensor nodes deployed in the region of interest (RoI). Coverage problems are commonly classified into two types: target coverage problem and area coverage problem. The former ensures the monitoring of only certain specific points which have fixed positions in the area of interest, while the latter is concerned with the supervision of the whole deployment area. In this paper, an area coverage problem was considered. The sensing area was considered as m × n grids, each grid point size was equal to 1 and denoted as G(x, y). The zone covered by a sensor node was a disk with a radius equal to the sensing radius of the sensor (Rs) (Fig. 1). The binary sensing model was considered. For this model each grid point within the sensing radius of a node can be taken as covered with probability equal to "1" and point out of the sensing range was set as "0" since it cannot be covered.

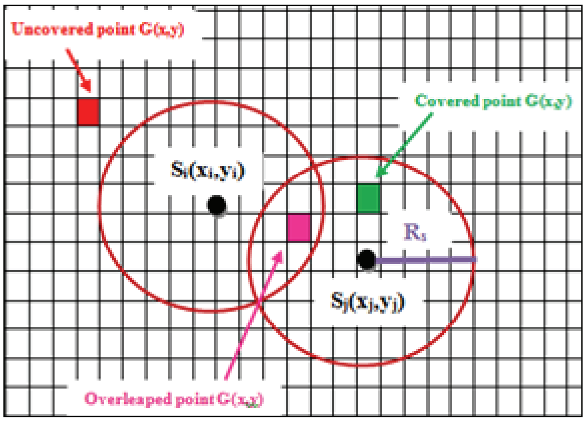

Fig. 1. Sensor coverage in sensing field.

Thus, the coverage of the whole area is proportional to the grid points that can be covered by at least one sensor $S_i(x_i, y_i)$ [18].

$$P(x, y, S_i) = \begin{cases} 1, & \text{if } \sqrt{\left(x - x_i\right)^2 - \left(y - y_i\right)^2} \leq R_s \\ 0, & \text{otherwise} \end{cases} \tag{5}$$

Supposing that a WSN consists of N_S sensor nodes, the probability that a point G(x, y) is covered can be given by:

$$P(x, y, S) = 1 - \prod_{i=1}^{Ns} \left(1 - P(x, y, S_i)\right) \tag{6}$$

And the Coverage Ratio (R_{cov}) is given by:

$$R_{cov} = \frac{\sum_{x=1}^{m}\sum_{y=1}^{n} P(x,y,S)}{m*n} \quad (7)$$

The second objective function is to maximize the total coverage area. But, since energy consumption has to minimized, coverage metric should be modeled as a minimizing problem. So, our objective function has to be expressed as minimizing the non-coverage ratio which is equal to 0 in case of full coverage.

$$f_2 = Minimize\left(1 - R_{cov}\right) \quad (8)$$

3.5. Connectivity Constraint

The network connectivity is satisfied if there exists, at least, one path from the sensor node to the sink node. Here, connectivity is considered as a problem constraint.

Definition 1. Node Degree.

Given an undirected graph G, the degree Deg (u) of a vertex u ϵ V is specified as the number of neighbors of u [19].

Definition 2. k-Node Connectivity.

A graph is considered to be connected if for every pair of nodes, there exists a single hop or a multi-hop path connecting them otherwise the graph is called disconnected. A graph is considered to be Q-connected if for any pair of nodes there are at least Q reciprocally separate paths connecting them [19].

4. Proposed Approach

Our objective was to enhance the performances of WSN by optimizing both coverage [20] and energy consumption metrics without affecting the network connectivity. Here, we dealt with area coverage problem for a centralized random placement topology with a predefined number of sensors. The proposed approach is a multi-objective approach based on FPA. This section presents the different rules and steps of the proposed approach [21].

4.1. Multi-Objective Flower Pollination Algorithm

Meta-heuristics algorithms are often inspired from nature and designed to solve challenging optimization problems. Here, we considered one of the most recent meta-heuristic algorithms named FPA, developed by Xin-She Yang in 2012 [5] for the global optimization problems. FPA inspired from the flower pollination process of flowering plants. In nature, flowers pollination process resulting from the transfer of pollen, typically, by pollinators such as insects, birds, bats and other animals. In this work, we presented a multi objective approach based on MOFPA [6] to solve deployment problems for WSN. FPA has the following four rules:

1. Cross-pollination is a global pollination process with pollen carrying pollinators doing Lévy flights.

2. Self-pollination is considered as local pollination.

3. Flower constancy can be defined as the reproduction probability proportional to the similarity of the two flowers involved.

4. Global and local pollination is controlled by a switch probability p ϵ [0, 1].

The fitness function used for this work is given by the following equation:

$$f = \text{Minimize}\,(f_1, f_2) \quad (9)$$

With f_1 and f_2 described above.

The pseudo-code of the proposed approach is presented as follow:

Algorithm 1: MOFPA

Begin

Read Ns, Switching probability p, Max Iteration Max_t, ε, p, Iteration count t, Flower count F_{count} and Solution space.

Step 1: Create initial population (Algorithm 2)

Step 2: Find fitness of each flower using the fitness function f, then find the Global Flower g* which have minimum fitness value.

Step 3: For each flower except the g* generate a random number r.

if (r<p) **then**

Pollinate current flower with global flower g*:

$F_i^{t+1} \leftarrow F_i^t + L(g^* + F_i^t)$

else

Pollinate current flower with any other flower in the population:

$F_i^t+1 \leftarrow F_i^t + \varepsilon\,(F_k^t + F_j^t)$

end if

$F_{count} \leftarrow F_{count} + 1$

Step 4: if new solution F_i^{t+1} is better than current solution F_i^t then update them in the population, if new solution F_i^{t+1} is better than g* update the global solution.

Step 5: **if** ($t < Max_t$) **then** t=t+1

else

Go to Step 3

end if

End

Where Nf represents the number of flower, ε is the scaling factor, p is the switching probability, Fti is solution vector F_i at iteration t and g* is the current best solution found among all solutions at the current generation/iteration. Thus, to imitate the movement of the pollinator, FPA uses Lévy flight. Therefore, we draw L > 0 from a Lévy distribution:

$$L \sim \frac{\lambda\Gamma(\lambda)\sin(\frac{\pi\lambda}{2})}{\pi}\frac{1}{s^{1+\lambda}} \quad (s \gg s_0 \gg 0) \quad (10)$$

4.2. Initial Population

To implement the proposed approach, we needed to create an initial population for FPA. In this work, we considered that each individual or flower represented the vector of all sensor nodes position (x, y) in RoI.

To create the initial population, we began by generating the position of the sink node at the centre of RoI for each flower. Then, we deployed the remaining sensors randomly after verifying the connectivity constraint. Actually, the network connectivity is assumed to be full if the distance between two sensors is less than the communication radius (Rc) of the sensor. Rc is set at 2RS to guarantee the network connectivity [22]. The distance is defined as the Euclidean distance between two sensors. In addition, to ensure a sufficient distribution in RoI, we controlled the number of neighbors of each deployed node that should be less than a predefined number Ne. Here, Ne was set to 1. So, we dealt with 1-connected network.

The pseudo-code of the initial population is presented as follow:

Algorithm 2: Initial population
Begin
Read N_f, Ns, Solution space, Flower count F_{count}, Sensor count S_{count} and Neighbors Ne.
Step 1: For each flower F_i **Deploy**($Sink_i$)
S_{count} ← 0
While ($S_{count} \leq$ Ns)
Generate-Random-Position(S_k)
if ∃ S_j **While** ($D_{kj} < R_c$) **then**
  if Neighbors(S_k) <= Ne **then**
Deploy(S_k)
k ← k+1
end if
end if
End

With S_i is the sensor node i, Nf is number of flowers, Rc is the node communication radius and Ne is the maximum number of neighbors.

5. Simulation and Results

To validate the performances of the proposed approach, some simulations were performed. Here, the binary sensing model was taken and sensor nodes of the initial population were randomly distributed.

The network is homogeneous, i.e., all sensors have the same deployment parameters such as the sensing and communication radius. Simulations were carried out using MATLAB R2016a. The algorithm was run a maximum number of iterations of 1500 for 5 runs.

Fig. 2 presents all solutions (dominated and non-dominated) obtained over five runs of the proposed algorithms. The simulation shows that 90 % of non-dominated solutions (see Fig. 2) offered the following pairs of values: (217.09, 0.166) and (199.36, 0.168), for Energy Consumption and non-Coverage Ratio, respectively.

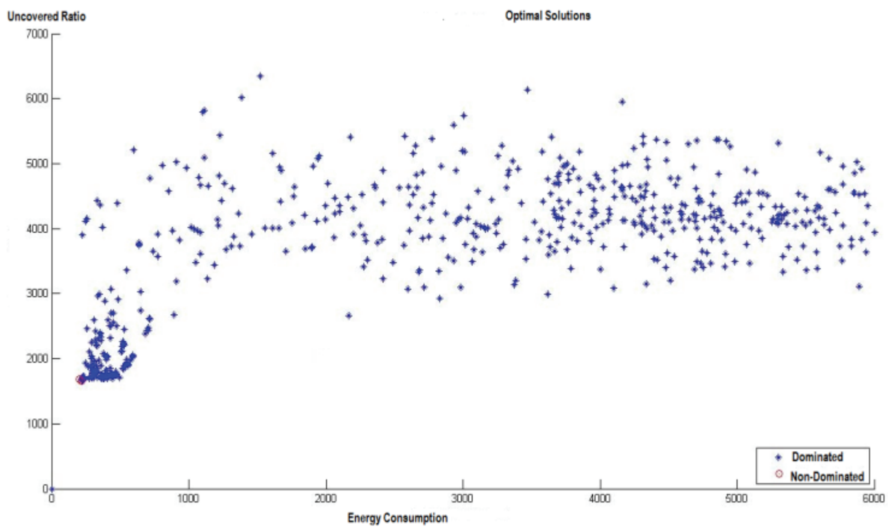

Fig. 2. Non-dominated solutions of MOFPA.

Table 2 presents the definitions and the values of simulation parameters. The non-dominated solutions were close but not overlapping. Comparing the simulation results with the initial values, i.e. those of initial population, we can notice the amelioration offered by our approach in terms of the considered objective functions. Actually, the proposed approach was 38.62 and 2.86 times better in minimizing energy consumption and non-covered area, respectively.

In this work, the simulation results of MOFPA were compared with those of PSO algorithm [23] in different instances. PSO was tested by considering the same initial simulation parameters (See Table 2). Fig. 3 and Fig. 4 show the results of MOFPA compared with those of PSO algorithm.

Table 2. Definition and value of simulation parameters.

Parameter	Definition	Value
x_m	Maximum width of RoI	100 m
y_m	Maximum length of RoI	100 m
R_c	Communication radius	30 m
R_S	Sensing radius	15 m
N_S	Number of sensors	15
Ne	Maximum number of neighbours	1
IE	Initial energy for each sensor	1 Ah
ME_i	Maintenance energy for node i	13 mA
TE_i	Transmission energy for node i	20 mA/m
RE_i	Reception energy	2 mA
N_f	Number of flower	20
p	Switching probability	0.8
$NCov_{pop0}$	Non-coverage ratio of initial population	0.4777
E_{pop0}	Energy consumption of Initial population	8042 mA

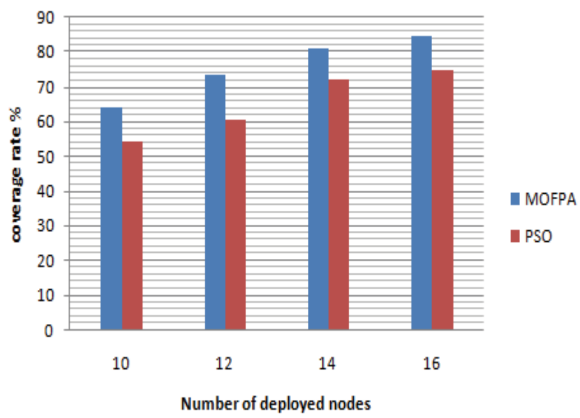

Fig. 3. Average of Coverage rate of non-dominated solutions.

Fig. 3 presents the average of coverage rate of non-dominated solutions found after 1500 iterations of the two algorithms for different instances. We notice that the total coverage rate of RoI increases when the number of deployed nodes increases. The proposed approach outperforms the PSO in all instances and produces maximum coverage area.

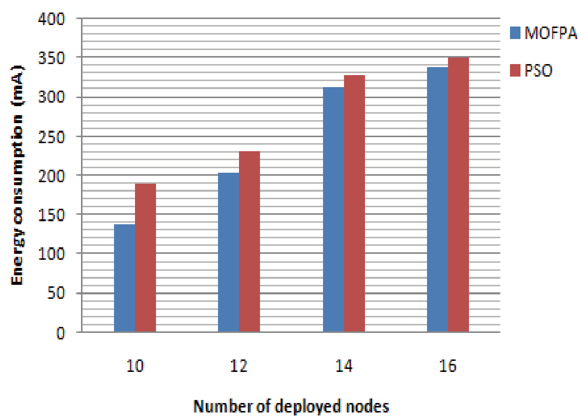

Fig. 4. Average of energy measure of non-dominated solutions.

Fig. 4 presents the average of energy consumption of non-dominated solutions found after 1500 iterations of the two algorithms for different instances. We notice that the total energy consumption increases when the number of deployed nodes increases. The proposed approach outperforms the PSO in all instances and consumes minimum net energy.

Fig. 5 shows samples of sensor nodes topologies in the ROI for MOFPA. The best solution simulation results of MOFPA are plotted in Fig. 5 (a) for 10 nodes and in Fig. 5 (b) for 12. Also, with growing number of nodes more node were placed closer to the sink node to maintain lower energy.

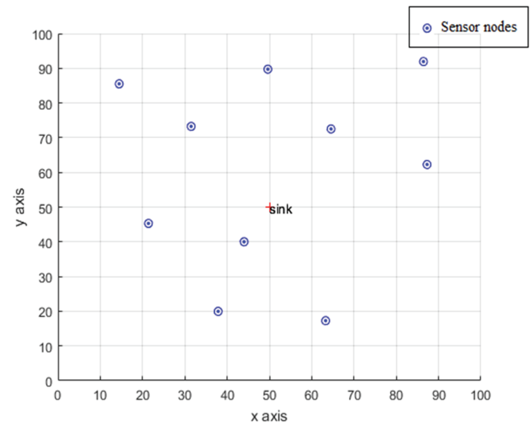

(a)

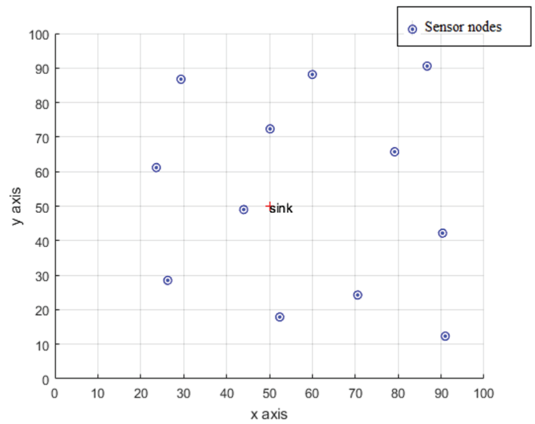

(b)

Fig. 5. (a) Sample node topology for10 node setup with MOFPA and (b) sample node topology for 12 node setup with MOFPA.

6. Conclusions

The main aim of multi-objective optimization algorithms is to find an approximate trade-offs between the computational objective functions. This paper presented a new multi-objective approach for node deployment problem in WSN. The proposed approach tried to deploy sensor nodes in the RoI while maximizing coverage area, minimizing energy consumption and maintaining net connectivity. Simulation results show that MOFPA produce better network topology than PSO in terms of both coverage and energy consumption. In a future work, we will incorporate other QoS metrics like sensor lifetime.

Acknowledgements

The authors would like to acknowledge the financial support of this work by grants from General Direction of Scientific Research (DGRST), Tunisia, under the ARUB.

References

[1]. F. Oldewurtel, P. Mhnen, Analysis of enhanced deployment models for sensor networks, in *Proceedings of the IEEE 71st Conference on Vehicular Technology Conference (VTC'10)*, 16-19 May 2010, pp. 1-5.

[2]. M. Younisa, K. Akkayab, Strategies and techniques for node placement in wireless sensor networks: A survey, *Ad Hoc Networks*, Vol. 6, Issue 4, 2008, pp. 621-655.

[3]. S. Meguerdichian, F. Koushanfar, M. Potkonjak, M. B. Srivastava, Coverage problems in wireless ad-hoc sensor networks, in *Proceedings of the IEEE Twentieth Annual Joint Conference of the Computer and Communications Societies (INFOCOM'01)*, Vol. 3, 22-26 April 2001, pp. 1380-1387.

[4]. R. T. Marler, J. S. Arora, Survey of multi-objective optimization methods for engineering, *Structural and Multidisciplinary Optimization*, Vol. 26, Issue 6, 2004, pp. 369-395.

[5]. X. S. Yang, Flower pollination algorithm for global optimization, *Unconventional Computation and Natural Computation*, Vol. 7445, 2012, pp. 240-249.

[6]. X. S. Yang, M. Karamanoglu, X. He, Multi-objective flower algorithm for optimization, *Procedia Computer Science*, Vol. 18, 2013, pp. 861-868.

[7]. Y. Yoon, Y. H. Kim, An Efficient Genetic Algorithm for Maximum Coverage Deployment in Wireless Sensor Networks, *IEEE Transactions on Cybernetics,*Vol. 43, Issue 5, 2013, pp. 1473-1483.

[8]. X. Yu, J. Zhang, J. Fan, T. Zhang, A faster convergence artificial bee colony algorithm in sensor deployment for wireless sensor networks, *International Journal of Distributed Sensor Networks*, Vol. 9, Issue 10, 2013, pp. 2-9.

[9]. S. Sengupta, S. Das, M. D. Nasir, B. K. Panigrahi, Multi-objective node deployment in WSNs: In search of an optimal trade-off among coverage, lifetime, energy consumption, and connectivity, *Engineering Applications of Artificial Intelligence*, Vol. 26, Issue 1, 2013, pp. 405-416.

[10]. M. R. Senouci, A. Mellouk, Localized Movement-Assisted Sensor Deployment Algorithm for Hole Detection and Healing, *IEEE Transaction on Parallel and Distributed Systems*, Vol. 25, Issue 5, 2014, pp. 1267-1277.

[11]. M. Rebai, M. L. Berre, H. Snoussi, F. Hnaien, L. Khoukhi, Sensor deployment optimization methods to achieve both coverage and connectivity in wireless sensor networks, *Computers & Operations Research*, Vol. 59, Issue C, 2015, pp. 11-21.

[12]. M. Abo-Zahhad, N. Sabor, S. Sasaki, S. M. Ahmed, A centralized immune-Voronoi deployment algorithm for coverage maximization and energy conservation in mobile wireless sensor networks, *Information Fusion*, Vol. 30, Issue C, 2016, pp. 36-51.

[13]. Q. Ni, H. Du, Q. Pan, C. Cen, Y. Zhai, An improved dynamic deployment method for wireless sensor network based on multi-swarm particle swarm optimization, *Natural Computing*, Vol. 16, Issue 1, 2017, pp. 5-13.

[14]. M. Rebai, M. L. Berre, H. Snoussi, F. Hnaien, L. Khoukhi, Sensor deployment optimization methods to achieve both coverage and connectivity in wireless sensor networks, *Computers & Operations Research*, Vol. 59, Issue C, 2015, pp. 11-21.

[15]. J. Zhang, Y. Lei, C. Chen, F. Lin, Directional Probability Perceived Nodes Deployment Based on Particle Swarm Optimization, *International Journal of Distributed Sensor Networks*, Vol. 13, Issue 3, 2016, pp. 1-6.

[16]. R. Ejbali, M. Zaied, C. Ben Amar, Multi-input Multi-output Beta Wavelet Network: Modeling of Acoustic Units for Speech Recognition, *International Journal of Advanced Computer Science and Applications*, Vol. 3, Issue 4, 2012, pp. 38-44.

[17]. O. Jemai, R. Ejbali, M. Zaied, C. Ben Amar, A speech recognition system based on hybrid wavelet network including a fuzzy decision support system, in *Proceedings of the Seventh International Conference on Machine Vision (ICMV)*, 14 May 2015, pp. 503-944.

[18]. A. Ghosh, S. K. Das, Coverage and connectivity issues in wireless sensor networks: A survey, *Pervasive and Mobile Computing*, Vol. 4, Issue 3, 2008, pp. 303-334.

[19]. D. B. West, Introduction to Graph Theory, *Prentice-Hall*, 2003.

[20]. F. Hajjej, R. Ejbali, M. Zaied, An efficient deployement approach for improved coverage in wireless sensor networks based on flower pollination algorithm, in *Proceedings of the Conference on International Conference on Applications of Graph Theory in Wireless Ad Hoc Networks and Sensor Networks (GRAPH-HOC),* 23-24 Dec. 2016, pp. 117-129.

[21]. F. Hajjej, R. Ejbali, M. Zaied, International Conference on Advances in Sensors, in *Proceedings of the Conference on Actuators, Metering and Sensing (ALLSENSORS)*, 19-23 March 2017.

[22]. A. Ghosh, S. K. Das, Coverage and connectivity issues in wireless sensor networks: A survey, *Pervasive and Mobile Computing*, Vol. 4, Issue 3, 2008, pp. 303-334.

[23]. R. Poli, J. Kennedy, T. Blackwell, Particle swarm optimization, *Swarm Intelligence*, Vol. 1, Issue 1, 2007, pp. 33-57.

[24]. R. Ejbali, M. Zaied, C. Ben Amar, Intelligent approach to train wavelet networks for Recognition System of Arabic Words, in *Proceedings of the International Conference on Knowledge Discovery and Information Retrieval*, October 25-28 Oct 2010, pp. 518-522.

Published by International Frequency Sensor Association (IFSA) Publishing, S. L., 2017 (http://www.sensorsportal.com).

Sensors & Transducers, Vol. 213, Issue 6, June 2017, pp. 9-23

Sensors & Transducers

Published by IFSA Publishing, S. L., 2017
http://www.sensorsportal.com

Deployment Strategies and Clustering Protocols Efficiency

Chérif Diallo
Laboratoire Algébre, Cryptographie, Codes et Applications (ACCA)
UFR Sciences appliquéeset de Technologies (UFR SAT)
Université Gaston Berger, BP 234 Saint-Louis, Sénégal
Tel.: +221339612340, fax: +221339615338
E-mail: cherif.diallo@ugb.edu.sn

Received: 22 April 2017 /Accepted: 31 March 2017 /Published: 30 June2017

Abstract: Wireless sensor networks face significant design challenges due to limited computing and storage capacities and, most importantly, dependence on limited battery power. Energy is a critical resource and is often an important issue to the deployment of sensor applications that claim to be omnipresent in the world of future. Thus optimizing the deployment of sensors becomes a major constraint in the design and implementation of a WSN in order to ensure better network operations. In wireless networking, clustering techniques add scalability, reduce the computation complexity of routing protocols, allow data aggregation and then enhance the network performance. The well-known MaxMin clustering algorithm was previously generalized, corrected and validated. Then, in a previous work we have improved MaxMin by proposing a Single-node Cluster Reduction (SNCR) mechanism which eliminates single-node clusters and then improve energy efficiency. In this paper, we show that MaxMin, because of its original pathological case, does not support the grid deployment topology, which is frequently used in WSN architectures. The unreliability feature of the wireless links could have negative impacts on Link Quality Indicator (LQI) based clustering protocols. So, in the second part of this paper we show how our distributed Link Quality based d-Clustering Protocol (LQI-DCP) has good performance in both stable and high unreliable link environments. Finally, performance evaluation results also show that LQI-DCP fully supports the grid deployment topology and is more energy efficient than MaxMin.

Keywords: Wireless sensor network, Deployment strategy, Multihop Clustering, LQI, MaxMin, LQI-DCP.

1. Introduction

The deployment strategy of sensor nodes in a control zone is cited among the critical points in the design of sensor applications. It tightly depends on the nature of the WSN application and its main objectives [1-4]. The nodes are often either distributed in a predefined manner or randomly (dropped from a mobile system such as an airplane for example).

For some applications precise distribution of the nodes is a requirement for properly functioning. The nodes must be deployed in predetermined positions to ensure efficient network operations as the application results rely on node locations: home medical monitoring of a patient, roads monitoring, operation supervision of industrial systems, etc.

Other applications do not require accurate distribution of the nodes. This is the case of such applications where the sensor nodes could be deployed randomly. This could be due to the environment difficulties (geographical, climatic, etc.): military surveillance of the enemy zone, forest fire monitoring systems, etc.

In a cold chain monitoring application, due to the size of a warehouse which hosts large numbers of pallets, provided each with a temperature sensor, the Wireless Sensor Network (WSN) can reach several hundreds of nodes which collaborate for sending alarms towards the Base Station (BS). This application specifically collects rare events (alarms) to ensure the proper monitoring of the system. If the temperature is over a threshold, an alarm will be generated; this "interesting event" is then sent towards the BS. In such a context, network clustering techniques add scalability feature and then reduce the computation complexity of data gathering and routing protocols [5].

The more often WSN architecture used in cold chain monitoring applications is the grid deployment topology. So, in this paper, we show that one should be careful with the MaxMin clustering heuristic in such a topology.

In [2] and [6], we have shown how it is important to sufficiently outspread clusterheads in order to reduce cluster overlaps, the amount of channel contention between clusters and energy wastefulness due to overhearing phenomenon. The MaxMin clustering heuristic, as proposed in [7-8], has the drawback of not taking into account this problem. In order to solve this issue, we have proposed LQI-DCP in [3]. LQI-DCP is energy efficient LQI based protocol which aims to construct multihop clusters by producing clusters of which each clusterhead has a better positioning regarding the locations of other clusterheads. The clusterheads resulting from LQI-DCP are sufficiently outspread. LQI-DCP also reduces the density of clusterheads and then improves the WSN energy efficiency, while each sensor still remains at most d-hops away from its own clusterhead.

In a cold chain monitoring application, the warehouse hosts hundreds of pallets, one upon the other. This environment is subjected to some unreliability of the wireless links. So, it is important for LQI based clustering schemes to fully support such an environment. This is the main objective of the second part of this paper which completes discussions related in [2] and [3] where the grid deployment topology were not been taken into account. Moreover, our works in [1] did not include energy efficiency analysis which is the third objective of this paper.

Previous works [2, 7-8] present details on MaxMin, whereas LQI-DCP is described in [3]. All clusterhead selection criteria used in this paper are defined in [2-3]. As in [2-3] we indifferently use caryomme(s) or clusterhead(s).

To carry out our work, this paper is organized as follows: in the next section we will present few WSN deployment strategies before describing the MaxMin Pathological Case is in the section III. Consequently, we will explain, in the section IV, why MaxMin does not support the grid deployment topology. Then, in the sections V, we will show how LQI-DCP is well adapted for the grid deployment topology. Finally, the last two parts present performance results pertaining to MaxMin and LQI-DCP clustering protocols when one takes into account the unreliability feature of the wireless links (sections VI & VII) and the energy efficiency of network operations (section VIII).

2. WSN Deployment Strategies

2.1. Random Deployment without Constraint

The sensor deployment on a well-defined collection target could be done randomly, in which case the density might be very different from one location to another [9]. This type of deployment occurs during a bulk jet of the sensors from a helicopter or missile. Many sensor applications use a random deployment without constraint, due either to the hostility of the monitored area or its large size [10].

The use of the random deployment strategy creates the challenge of ensuring good connectivity quality in the network. Wireless links connectivity would be significantly degrading with poor distribution of the sensor nodes over the target area. Thus with this deployment type, some sensor nodes might have been isolated or disconnected. A sufficient quality of connectivity obviously helps ensuring packets routing under right conditions: low transmissions delay, low rate of packet losses, low energy consumption and high rate of successful delivery of messages to the base station.

The random deployment is also well suited for dense sensor networks where the redundancy of the sensors on the monitored area is a required for application accuracy. In such sensor systems, this could help in enhancing network lifetime by putting a certain number of redundant sensors on standby mode while ensuring a full coverage of the monitored area and maintaining a good network connectivity rate [10].

This type of deployment often requires a good clustering protocol to better guarantee good network performance. However, given the density of the network and the number of formed clusters, care should be taken to avoid the creation of single-node clusters which could annihilate network performance [2]. Furthermore, the protocol must be designed to produce clusterheads far enough away to maximize the network lifetime [3].

2.2. Deployment with Remoteness Constraint between Nodes

Another deployment strategy is the deployment with remoteness constraint between nodes. In this type of deployment, the minimum distance separating two nodes is at least equal to $\lambda * R$, where R is the communication radius and λ, $0 \leq \lambda \leq 1$, is the remoteness parameter [9]. If $\lambda = 0$, then this is the case of random deployment without constraint.

This type of deployment could be used in applications where sensors are equipped with GPS, or in indoor industrial applications where node locations are predetermined. Thus the remoteness parameter λ could be chosen in a manner to reduce network density. This will helps in reducing energy losses due to overhearing phenomenon [9].

Another variant of this type of deployment is the deployment of sensors run in a direction with remoteness constraint between nodes [9] which is common for many (military, agricultural, environmental, etc.) applications where nodes are deployed by a robot, vehicle, helicopter or plane in hostile environment where human presence is not easy [9]. In such applications, the remoteness parameter λ and the direction could be tuned according to the speed of the robot, vehicle, helicopter or plane.

This type of deployment responds to the same clustering constraints as the previous one. Except that in this case, the clustering protocol does not have to have as objective to produce clusterheads rather distant from each other because, given the parameter λ, the relative remoteness of the nodes is already ensured in the initialization phase of the network.

2.3. Grid Topology

The grid deployment topology is the most common topology for indoor sensor network architectures, particularly in cold chain monitoring or sensor based security applications. The grid may be uniform or not according to the values of steps used in the abscissa axis and that of the ordinates. Moreover, the positions of the sensors are often predetermined in the grid. Therefore, the clusterheads could be chosen according to their coordinates. This could facilitate the deployment of heterogeneous networks where some sensors, intended to be clusterheads, would have better hardware resources and greater computational capabilities. This would allow them to be positioned from the network start at locations that ensure better network performance. On the other hand, in the case of a homogeneous network with a clustering protocol, this one must be designed to be compatible with the inherent specificities of the grid topology. This is what we shall see in the following.

3. The MaxMin Pathological Case

The MaxMin algorithm is improved by \cite{ADelye},\cite{MMarot} as a generalization of the earlier MaxMin algorithm proposed by \cite{ADAmis}. It takes place in 2d+1 rounds. The first round consists of information exchanges to initialize the algorithm. The following d-rounds are the floodmax phase, which is followed by the floodmin phase composed of last d rounds.

Given the similarities with Linked Cluster Algorithm (LCA) [13] and LCA2 [14], MaxMin naturally inherits the same pathological case. Thus, in the original paper [8] which revealed MaxMin to the scientific research community, the authors reported the pathological case for which MaxMin fails in the process of cluster formation. We reproduce here the figure (Fig. 1) and the argument as they were stated in [8]: *"There is a known configuration where the proposed heuristic fails to provide a good solution. This configuration is when node ids are monotonically increasing or decreasing in a straight line. In this case, the **d+1** smallest node ids belong to the same cluster as shown in Fig. 1. All other nodes become clusterheads of themselves only. Again, while this is not optimal it still guarantees that no node is more than d-hops away from a clusterhead. Furthermore, this configuration is highly unlikely in a real world application. However, this is a topic of future work to be performed with this heuristic."*

Fig. 1. Worse case performance scenario for MaxMin [8].

In the next section, we will show how this pathological case has negative impacts on the grid deployment topology. Indeed, the authors of [8] said that: *"Furthermore, this configuration is highly unlikely in a real world application"*. This is obviously wrong because the grid deployment topology is more often encountered in real WSN applications, especially in a cold chain monitoring application.

4. MaxMin Incompatibility with the Grid Deployment Topology

To better understand the consequences of the MaxMin pathological case on the grid deployment topology, let us consider the representation in Fig. 2, where N nodes are deployed on a rectangular area of length L and width l. Considering a grid where each side of the area is subdivided with a constant step λ. Then, the coordinates $x(i)$ and $y(i)$ of the i^{th} node $i \in [| 1, N |]$ are obtained as follows:

$$n = \left\lfloor \frac{L}{\lambda} \right\rfloor, m = \left\lfloor \frac{l}{\lambda} \right\rfloor, N = ((n+1)*(m+1)) - 1,$$

where $\left\lfloor \frac{L}{\lambda} \right\rfloor$ denotes the integer part of $\frac{L}{\lambda}$

$$x(i) = \lambda * \left\lfloor \frac{i}{m+1} \right\rfloor, y(i) = \lambda * i \; mod(n+1)$$

If we assume that all nodes have the same transmission range ***R = 2*λ***. Consequently, the sensors 1, 3, 9, 19, 23, 21, 15 and 5 are equidistant from the node 12 and located exactly at the distance $\lambda * \sqrt{5}$ from the node 12, that is to say, outside the vicinity of the node 12. The same is true for the sensors 9, 13, 11 and 5 with respect to the node 2.Then, by running MaxMin algorithm with the parameter ***d = 1*** and the function criteria ***f(x) = id(x)*** for the WSN example in (Fig. 2), where ***id(x)*** is the number of the node ***x***:

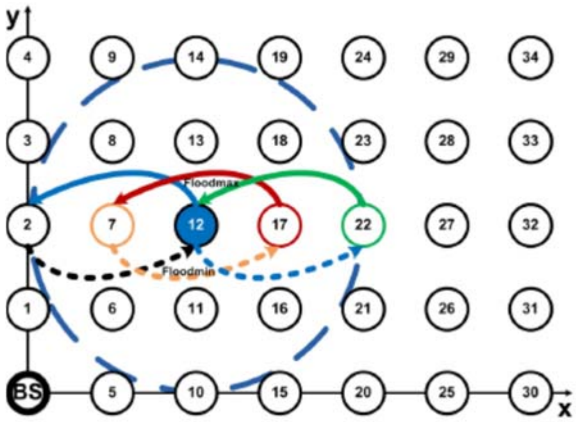

Fig. 2. MaxMin run in a grid deployment topology.

- During ***floodmax*** phase, the node 2 receives the value 12 from 12th node because the node 13 is not in the vicinity of the node 2.

- During ***floodmax*** phase, the node 1 receives the value 11 from 11th node because the node 12 is not in the vicinity of the node 1.

- Next, the node 12 receives this value 12 from 2nd node during the ***floodmin*** phase as the node 1 is not in the vicinity of the node 12.

- Accordingly, the 12th node is selected as clusterhead.

- As far as that goes, all the ith nodes, i ϵ [10, 34], are selected as clusterheads (Fig. 3).

- More generally, it's easy to show that all the ith nodes i ϵ [2(m+1),N] are selected as clusterhead by MaxMin.

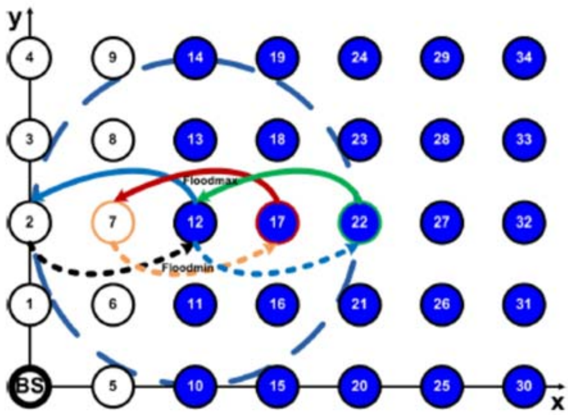

Fig. 3. Consequences of the MaxMin pathological case on the grid topology: with R = 2*λ, from the 3rd column, all nodes are elected caryommes.

The two tables above (Table 1 and Table 2) summarize MaxMin's computation for this network (Fig. 2). Here again we are using the same notations as in [2].

Table 1. MaxMin results with d = 1 for the WSN (Fig. 2).

Node ID	0	1	2	3	4	5	6	7	8	9	10	11	12	13	14	15	16	17	18	19
Floodmax W_1	10	11	12	13	14	14	16	17	18	19	20	21	22	23	24	25	26	27	28	29
Floodmax S_1	10	11	12	13	14	14	16	17	18	19	20	21	22	23	24	25	26	27	28	29
Floodmin W_2	10	10	10	11	12	10	10	11	12	13	10	11	12	13	14	15	16	17	18	19
Floodmin S_2	0	0	0	1	2	0	0	1	2	3	0	1	2	3	4	5	6	7	8	9
Caryomme	10	11	12	13	14	14	16	17	18	19	10	11	12	13	14	14	16	17	18	19

Table 2. MaxMin results with d = 1 for the WSN (Fig. 2) (continuous).

Node ID	20	21	22	23	24	25	26	27	28	29	30	31	32	33	34
Floodmax W_1	30	31	32	33	34	31	32	33	34	34	32	33	34	34	34
Floodmax S_1	30	31	32	33	34	31	32	33	34	34	32	33	34	34	34
Floodmin W_2	20	21	22	23	24	25	26	27	28	29	30	31	32	33	34
Floodmin S_2	10	11	12	13	14	14	16	17	18	19	20	21	22	23	24
Caryomme	20	21	22	23	24	25	26	27	28	29	30	31	32	33	34

Because of this, given the proximity of the clusterheads produced by MaxMin in this case, it is clear that most of the clusters are single node clusters. We have shown in [2] that this phenomenon of single node clusters is detrimental to the network performance because it considerably increases the energy consumption and thus reduces the lifetime of the network.

Thus, it is important to be careful when one chooses the criteria used to select the MaxMin clusterheads in the context of a grid deployment topology. Indeed, the "degree of connectivity" and "MinLQI" criteria also suffer the same effects because of the smoothness of the grid topology. These criteria are monotonically increasing in each row and each column of the grid when one moves from the edge toward the center of the deployment area.

Thus, MaxMin run with the Single-Node cluster reduction mechanism (SNCR) [2] leads to the following results for criteria: "Node id" (Fig. 4), "Degree of connectivity" (Fig. 5), and "MinLQI" (Fig. 6). These results are explained by the neighbourhood relationship (transmission range) between the selected clusterheads.

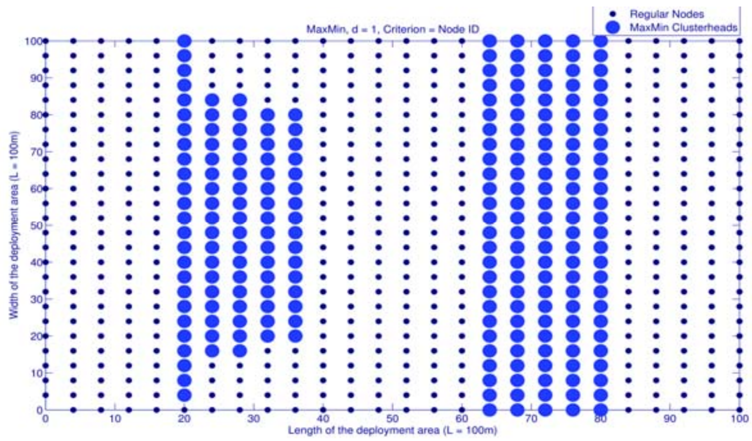

Fig. 4. MaxMin: Average clusterhead locations, Node ID criterion, d = 1.

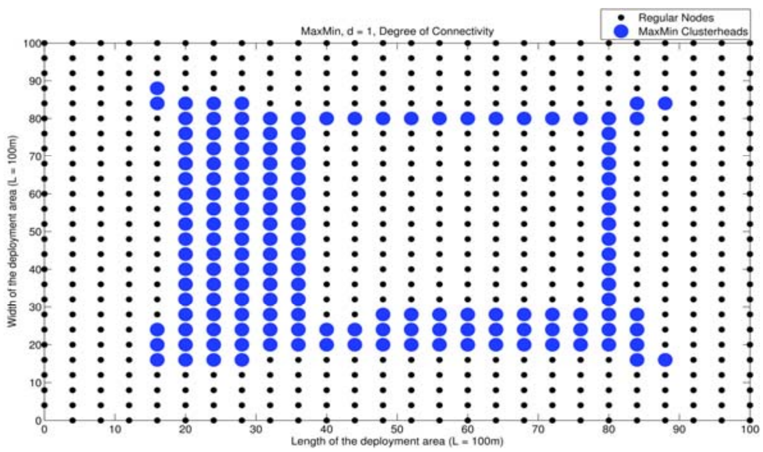

Fig. 5. MaxMin: Average clusterhead locations, Degree of Connectivity criterion, d = 1.

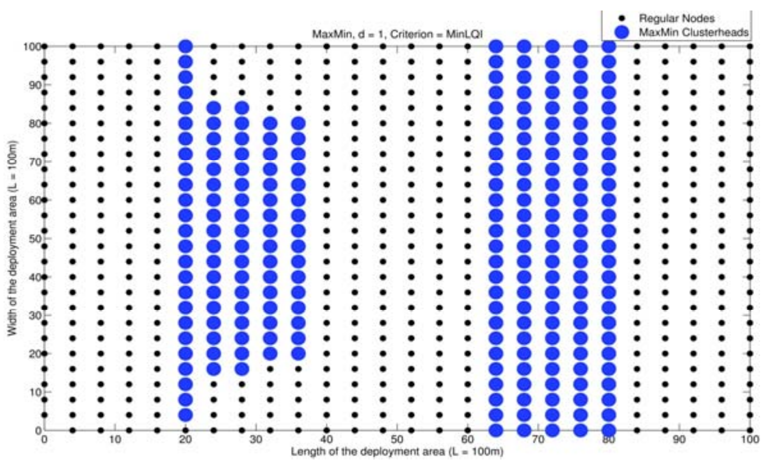

Fig. 6. MaxMin: Average clusterhead locations, MinLQI criterion, d = 1.

So, we obtain a series of clusterheads located in adjacent columns which are periodically separated by adjacent columns composed of regular nodes (Fig. 6).

To overcome this issue of MaxMin pathological case in a grid deployment topology, one should choose a criterion function of which the values are randomly distributed to the nodes. This helps avoiding a function which is monotonically increasing (or decreasing) along the lines of the grid. This randomization of the criterion overcomes the problem of MaxMin pathological case (Fig. 7) but also has the disadvantage of leading to unpredictable results. Indeed, the benefit of choosing a particular criterion rather than another one is to promote optimal results with respect to the main objectives of the application according to its operational conditions. (Fig. 7) shows the location of caryommes obtained for a randomized function criterion. As we can see, this result is not optimal because some clusterheads are too closely located. Therefore, this leads to high energy consumption because of overhearing, channel contention and overlaps between clusters [2].

The MaxMin pathological case is also a big drawback for multihop clusters, $d \geq 2$, as shown in (Fig. 8).

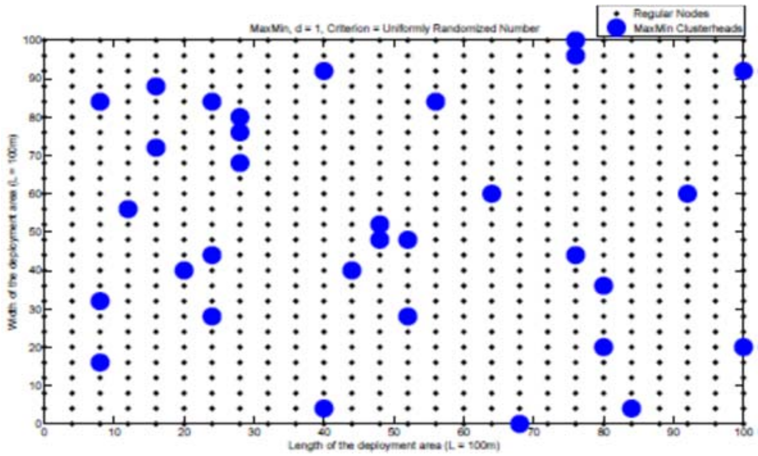

Fig. 7. MaxMin: Average clusterhead locations, Randomized Criterion, d = 1.

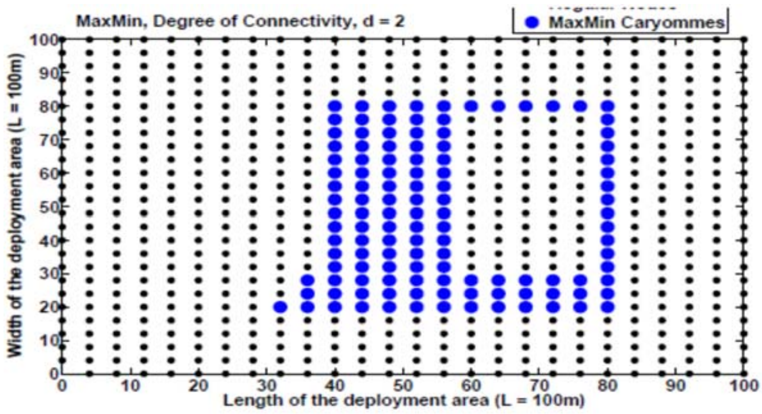

Fig. 8. MaxMin: Average clusterhead locations, degree of connectivity criterion, d = 2.

According to these results, we tend to conclude that MaxMin is not suitable for the grid deployment topology which is by far the most common topology encountered in cold chain monitoring applications.

5. LQI-DCP in the Grid Deployment Topology

The LQI-DCP protocol that we have proposed in [3] is a distributed multihop clustering protocol. LQI-DCP is based on the quality of links in order to swerve locations of the selected clusterheads. In a homogeneous network where all the sensors have the same transmission power, and in the absence of obstacles that can cause high interference, the LQI depends only on the distance separating the nodes. Intended for dense WSNs, its basic idea is to improve the efficiency of the network by caring about to sufficiently swerve the produced clusterheads. LQI-DCP takes place in two rounds. The first round comprises a series of information exchanges making it possible to initialize the algorithm and to preselect the nodes having the greatest criterion value within their neighborhood (i.e. the Preselected Nodes (PN)). Each Preselected Node (PN) designates its emissary nodes among its neighbors (Fig. 9). The emissary nodes allow identifying the neighbors that would be undesirable as clusterhead if the Preselected Node were to be finally elected as clusterhead. These undesirable nodes are called Whipping boy nodes. In the second round, the clusterheads are preferably chosen among the nodes that are not yet belonging to a cluster. A whipping boy node would only become clusterhead as a last resort.

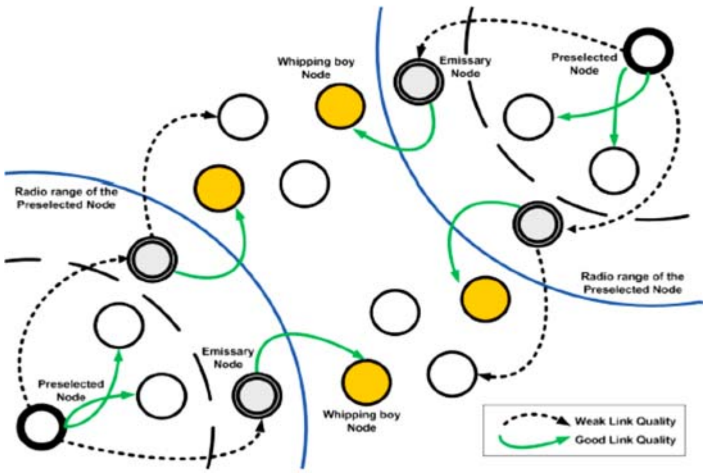

Fig. 9. Preselected, emissary and whipping boy nodes in LQI-DCP.

The first point to note is the redefinition of the notion of the "emissary node" in relation to the definition used in [6], where an additional condition imposed on the emissary node to have a neighbor outside the neighborhood of its "Preselected node" (PN). Removing this condition saves CPU resources and then improves the computation speed of the algorithm.

Then, as we can see in the Figs. 10, 11 and 12 related to the node transition states:

- An emissary node has necessarily a clusterhead.

- A node could be a Whipping boy node if and only if it is not in a cluster or if it is a Preselected Node (PN).

- In the case if a Preselected Node (PN) becomes a Whipping boy node, all the clustered nodes that were attached to it become unclustered.

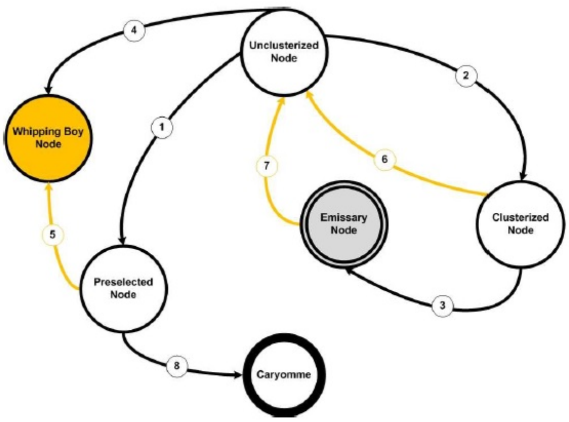

Fig. 10. LQI-DCP: Node transition states in 1st round.

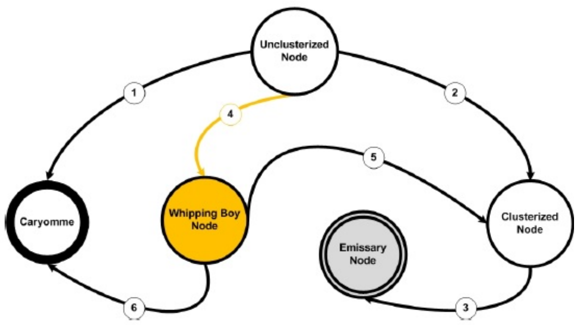

Fig. 11. LQI-DCP: Node transition states in 2nd round.

To overcome the grid topology issue for MaxMin, as we stated in Section IV, one should choose a criterion function of which the values are randomly distributed to the nodes. This helps avoiding a function which is monotonically increasing (or decreasing) along the lines of the grid. Even in this case, LQI-DCP (Figs. 15, 18) is more efficient than MaxMin (Figs. 16, 17) by sufficiently outspreading selected clusterheads.

Conversely our LQI-DCP protocol fully supports the grid deployment topology both for 1-hop and for multihop WSN clustering (Figs. 13, 14, 15, 19).

For LQI-DCP, the results make it possible to distinguish the clusterheads elected after the first round of those who are elected in the second round. The specificity of the Proximity-BS criterion is that it gives only one node elected as a clusterhead in the first round (Fig. 18). This result is explained by the fact that each node has, in its vicinity, at least one other node which is closer to it than the base station; With the exception of the only node of the network which is the closest to the base station. It is precisely this sensor that is the only node to be elected clusterhead in the LQI-DCP first round.

As for the Proximity-BS criterion, the result (Fig. 19) shows that there is only one selected clusterhead in the first round of LQI-DCP when the degree of connectivity is used as selection criterion.

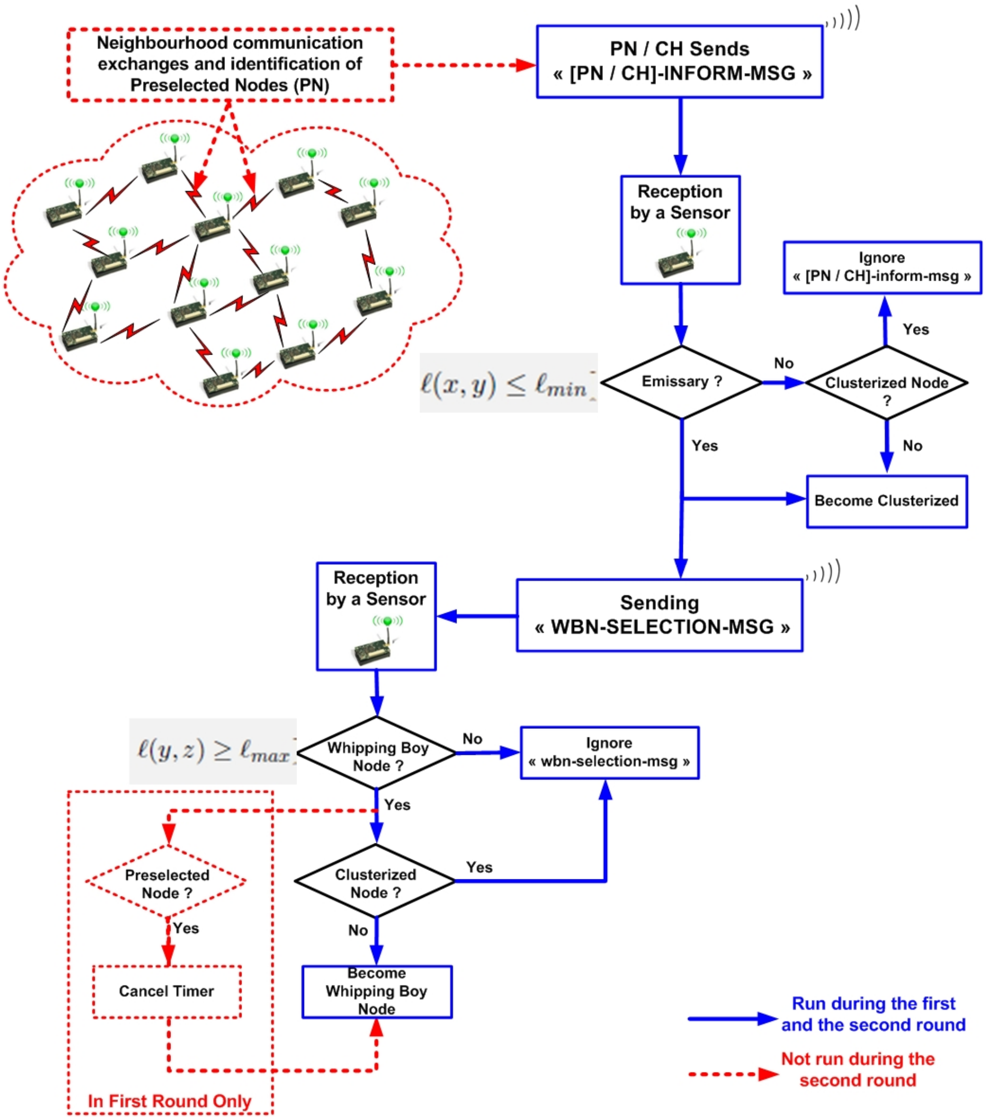

Fig. 12. The LQI-DCP Protocol Flowchart: 1st and 2nd Round. Contrary to the PN-INFORM-MSG, the CH-INFORM-MSG messages are firstly sent during the 2nd Round by the non clusterized nodes and then by the Whipping boy nodes.

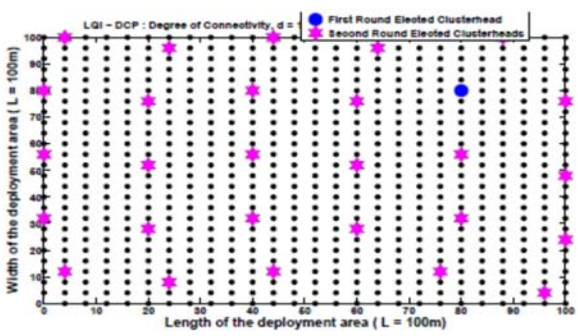

Fig.13. LQI-DCP: Average clusterhead locations, degree of connectivity criterion, d = 1.

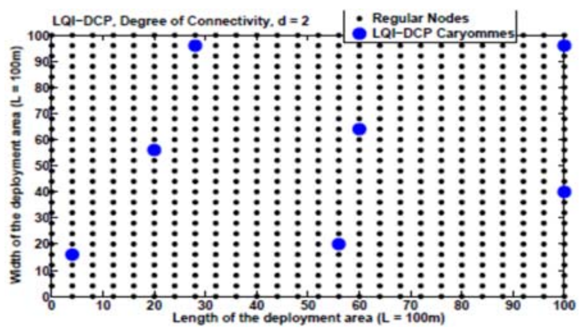

Fig.14. LQI-DCP: Average clusterhead locations, degree of connectivity criterion, d = 2.

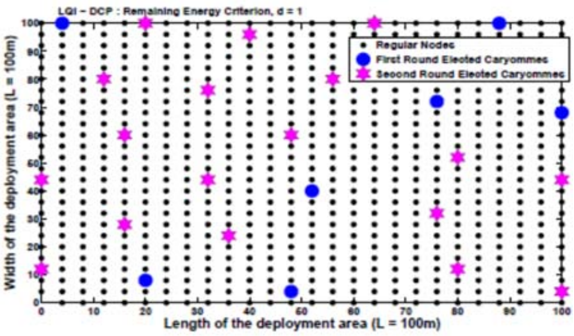

Fig. 15. LQI-DCP: Average clusterhead locations, Remaining Energy criterion, d = 1.

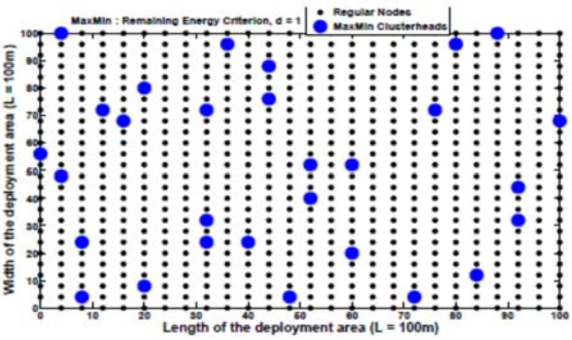

Fig. 16. MaxMin: Average clusterhead locations, Remaining Energy criterion, d = 1.

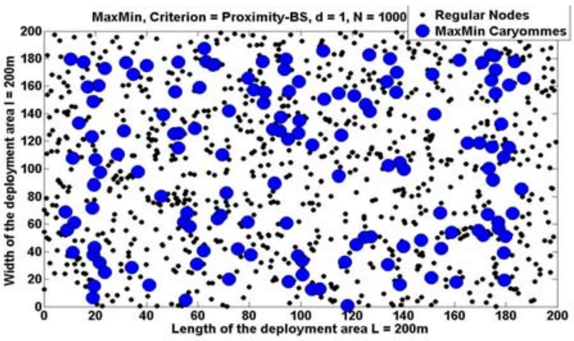

Fig. 17. MaxMin: Average clusterhead locations (Proximity-BS, d=1).

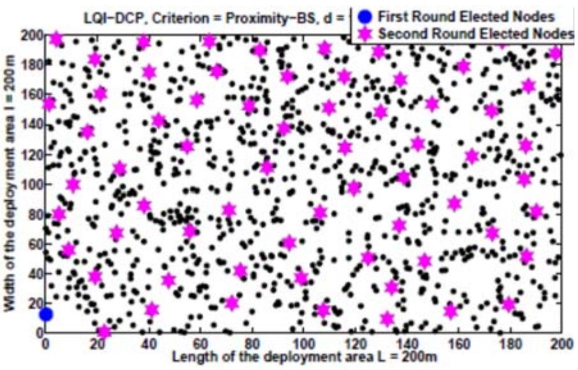

Fig. 18. LQI-DCP: Average clusterhead locations (Proximity-BS, d=1).

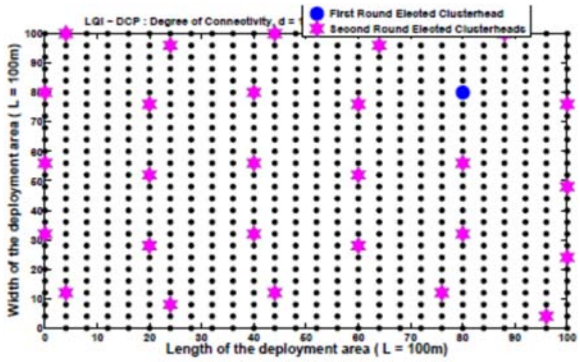

Fig. 19. LQI-DCP in grid topology: Average clusterhead locations (Degree of connectivity, d = 1). For R = 20 m, this result shows that the locations of the clusterheads produced by LQI-DCP is efficient. Moreover, there is only one elected clusterhead after the first round as explained above.

As far as that goes, the explanation is that, in the grid topology, each node has, in its neighborhood, at least another node which has as many as neighbors. The nodes having the same degree of connectivity as per their tie "node IDs" because of the total order relation in V defined by the equation:

$$\forall\, x \in V, v(x) = \big(f(x), id(x)\big),$$

Where ***f(x)*** is the criterion function (such as the Proximity-BS, the degree of connectivity) and ***id(x)*** returns the address of the node ***x***. The total ordering in V is defined as follows:

$$\forall x, y \in V, v(x) > v(y) \Leftrightarrow \big(f(x) > f(y)\big) \\ or\ (f(x) = f(y) and\ id(x) > id(y))$$

So there is finally a single node ***x ϵ V*** in the network that has the highest degree of connectivity that all its neighbors (due to its address value ***id(x)***). This is the node which is logically the only one elected after the first round (Fig. 19).

6. LQI Model for Performance Evaluation Purposes

At each given time ***t***, the LQI value of the link formed by any pair ***(x, y)*** of nodes is calculated by using the ***ℓ(x, y, t)*** function defined below:

$$\ell(x; y, t) = f(x, y, t) * g(x, y),$$
$$f(x, y, t) = 1 - Pr\,[link(x, y, t) = Unreliable],$$
$$g(x, y) = \alpha + \frac{\beta * \log(1 + (\gamma(x, y) - \gamma\min(x)))}{\log(1 + \gamma\max(x))},$$
$$\gamma(x, y) = \frac{1}{d(x,y)},$$
$$\gamma\min(x) = \min_{y \in N1(x)} \gamma(x, y),$$
$$\gamma\max(x) = \max_{y \in N1(x)} \gamma(x, y),$$

where α = 50, β = 255 and ***d(x, y)*** is the distance separating ***y*** from ***x***. ***N1(x)*** is the 1-hop neighborhood of the node ***x***.

In the context of a cold chain monitoring application, the warehouse hosts hundreds of pallets, one upon the other. Each pallet is provided with a temperature sensor. This environment is subjected to some unreliabilities of the wireless links. So, in the formula, ***Pr[link(x,y,t) = Unreliable]*** denotes the probability that the link ***link(x,y,t)*** becomes unreliable at time ***t***. This probability is used in some simulation scenarios, in order to evaluate the behavior of our LQI-DCP protocol with respect to the unreliability feature of the wireless links.

The choice of this model is guided by experimental results shown in [15] and [16], which stated that the LQI decreases when the distance between nodes increases in ZigBee-based WSN.

As we can see, $\ell(x,y,t) \neq \ell(y,x,t)$. Hence, the model allows taking into account asymmetrical aspects of the wireless links.

For moteiv's Tmote Sky [17] sensors equipped with chipcon's CC2420 [18], the LQI values range from 50 to 110. Even so, we stick with the ZigBee standard [19-20] because some manufacturers, such as Sun-SPOT [21] and WiEye [22], are still using the standard LQI values. Then, we use the standard values (i.e., [0, 255]) increased by $\alpha = 50$, instead of those of CC2420. The use of $\alpha = 50$ allows to keep the null value, $\ell(x,y,t) = 0$, only for the two cases where the node ***y*** is not in the transmission range of the node ***x***, or when the $\ell(x,y,t)$ becomes unreliable i.e., ***Pr[link(x,y,t) = Unreliable] = 1***.

This LQI model is only used for simulation purposes, so sensor nodes do not compute these above formulas.

Simulations, using Matlab, are run for a network size ranging from 200 to 4000 nodes. The performance results presented here are obtained by averaging the results for 100 different simulations for the two scenarios (Figs. 20, 21). As for others scenarios 80 different simulations were run. For each simulation, a new random node layout is used.

In all simulation results presented below, $\ell_{max} = 230$ and $\ell_{min} = 70$ as defined in [3].

The MinLQI clusterhead selection criterion is also defined in [2]. For a node, the MinLQI value represents the minimum LQI value beyond a given threshold which is set to 100, in all simulation scenarios.

7. Impacts of the Unreliability Feature of the Wireless Links on LQI-DCP Operations

In the context of a cold chain monitoring application, the warehouse hosts hundreds of pallets, one upon the other. Each pallet is provided with a temperature sensor. This environment is subjected to the unreliability feature of the wireless links. In this section we take into account such a phenomenon. For a sensor S_i, its unreliable links with some neighbors are modeled by the Bernoulli distribution of parameter ***p*** which takes the value "unreliable" with the probability defined as follows:

$$Pr[link(x,y,t) = Unreliable] = 1, \quad if\ \delta(i,j,t) \leq p,$$

where δ(i,j) is a random generated number which is uniformly distributed in]0,1] for each neighbor S_j of the sensor S_i. If ***Pr[link(x,y,t) = Unreliable] = 1***, then at time ***t***, $\ell(x,y,t) = 0$ and the node S_j would not become a whipping boy node related to the emissary node S_i even if S_j is too closely located to S_i.

Before inspecting the impacts of the unreliability feature of the wireless links, it is useful to examine the average ratio of the whipping boy nodes finally elected as clusterheads in the scenario where all links are considered reliable, i.e.:

$$\forall t, \forall x \in V, Pr[link(x,y,t) = Unreliable] = 0, \forall y \in N1(x)$$

Then, the Fig. 20 plots the average number of the whipping boy nodes finally selected as clusterheads divided by the overall number of clusterheads produced by LQI-DCP. For all studied criteria, this ratio is too low. For the proximity with respect to the BS, around ***1 %*** of clusterheads are chosen from the whipping boy nodes. This ratio is between ***1 %*** and ***2,5 %*** for the degree of connectivity criterion and between ***3 %*** and ***4 %*** for the MinLQI criterion.

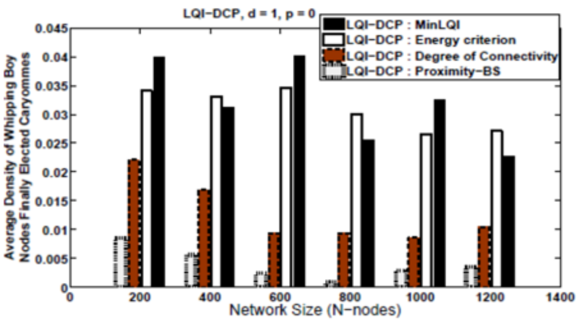

Fig. 20. LQI-DCP: Average density of whipping boy nodes finally selected as clusterheads, d = 1, p = 0.

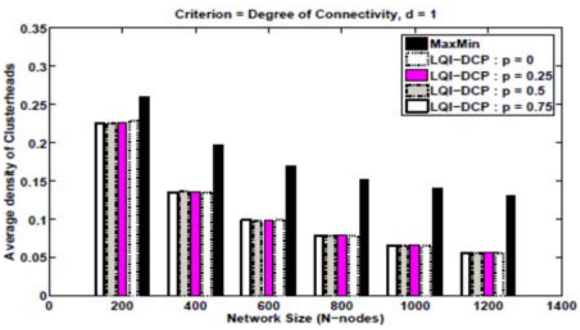

Fig. 21. LQI-DCP: Average density of clusterheads, degree of connectivity criterion, d = 1.

Fig. 21 shows that the unreliability of the wireless links has negligible effects on the average density of clusterheads by comparing results for ***p = 0*** (all links are reliable), ***p = 0.25, p = 0.5 and p = 0.75*** (high unreliability), when the degree of connectivity is used as criterion. Fig. 22 displays the average positions of clusterheads for ***p = 0.75***.

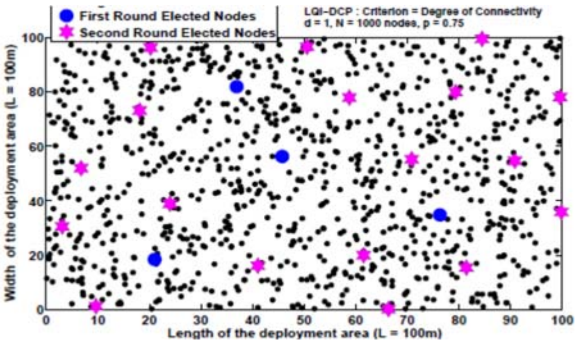

Fig. 22. LQI-DCP: Average clusterhead locations, degree of connectivity criterion, d = 1, p = 0:75.

In these scenarios, no link unreliability is taken into account for the MaxMin clustering scheme. The unreliability feature of the wireless links is only considered for the LQI-DCP clustering protocol.

This result (Fig. 23) is remarkable, because for ***R = 20 m and d=2,*** it means that high unrelibilities of the wireless links ***(p = 0.75)*** do not have negative impacts on LQI-DCP.

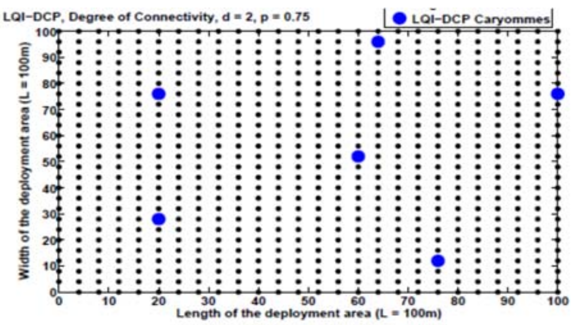

Fig. 23. LQI-DCP: Average clusterhead locations, degree of connectivity criterion, R = 20 m, p = 0:75, multihop clusters d = 2.

For MaxMin protocol, in the results (Fig. 21, 24, 26), the unreliability feature of the wireless links is not taken into account. Then for all scenario in this paper, ***p=0***, for MaxMin protocol. The unreliability feature of the wireless links is taken into consideration only for LQI-DCP.

The Fig. 22, 23, 25 and 27 plot, for LQI-DCP, the average clusterheads location when the WSN is subjected to high unreliability phenomenon of the wireless links, i.e., ***p = 0.75***.

These results show that the unreliability of the wireless links also has negligible effects on the locations of clusterheads selected by LQI-DCP: caryommes are sufficiently outspread. If a link were to be unreliable, the only effect on LQI-DCP is to decrease the number of whipping boy nodes in both first and second round of the LQI-DCP process. As a neighbor of a first round elected node cannot become a clusterhead. Then unreliability of the wireless links has low impact on the LQI-DCP clustering scheme.

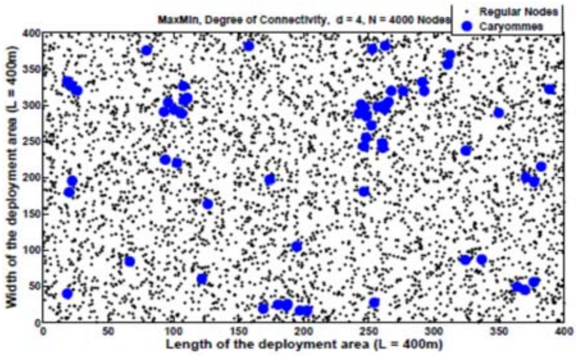

Fig. 24. MaxMin: Average clusterhead locations, degree of connectivity criterion, N = 4000 Nodes, R = 20 m, p = 0, multihop clusters d = 4.

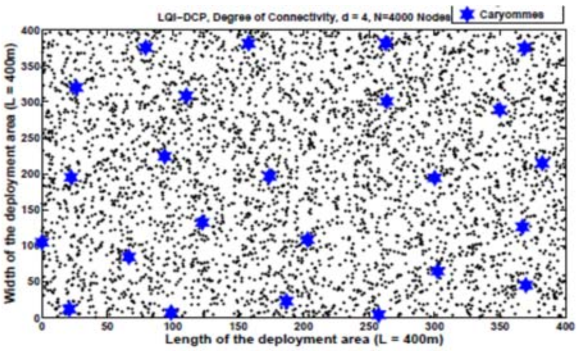

Fig. 25. LQI-DCP: Average clusterhead locations, degree of connectivity criterion, N = 4000 Nodes, R = 20 m, p = 0:75, multihop clusters d = 4.

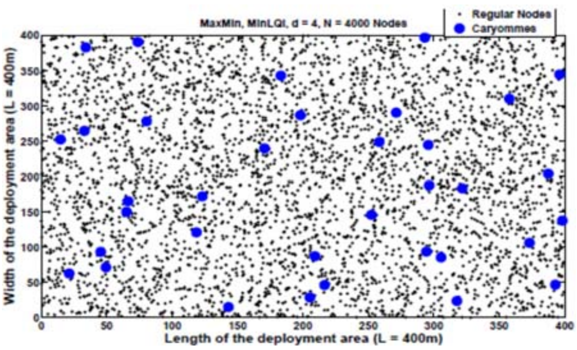

Fig. 26. MaxMin: Average clusterhead locations, MinLQI criterion, N = 4000 Nodes, R = 20 m, p = 0, multihop clustering d = 4.

For explanation, consider the example illustrated in (Fig. 28), in which we suppose that the sensor $\boldsymbol{C_i}$, although located closely to the preselected node PN, also forms a link of poor quality with PN, i.e., $\ell(PN;C_i) \leq \ell_{min}$. Thus C_i would be an "emissary node" of PN. However, even if C_i has a good link quality with C_j, i.e., $\ell(C_i;C_j) \geq \ell_{max}$, C_j will not become a "whipping boy node", relatively to C_i, because it is already clusterized and attached to PN as clusterhead [3].

In the same example (Fig. 28), the unreliability feature of the wireless links could also affect the quality of the link formed by the emissary node Ei with the sensor BE_i. Which might result in considering BE_ias a non-clusterized regular node which is not a "whipping boy node". However, in a dense WSN, BE_i could have some good links with other emissaries such as E_j or E_k. In this case, BE_i would become a "whipping boy node" (Fig. 28). This property could be less true in cases where the WSN is deployed with a low node density.

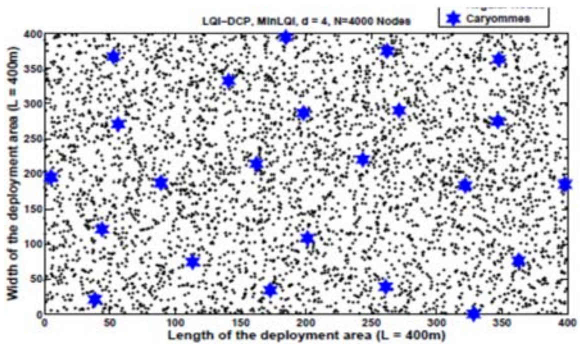

Fig. 27. LQI-DCP: Average clusterhead locations, MinLQI criterion, N = 4000 Nodes, R = 20 m, p = 0:75, multihop clustering d = 4.

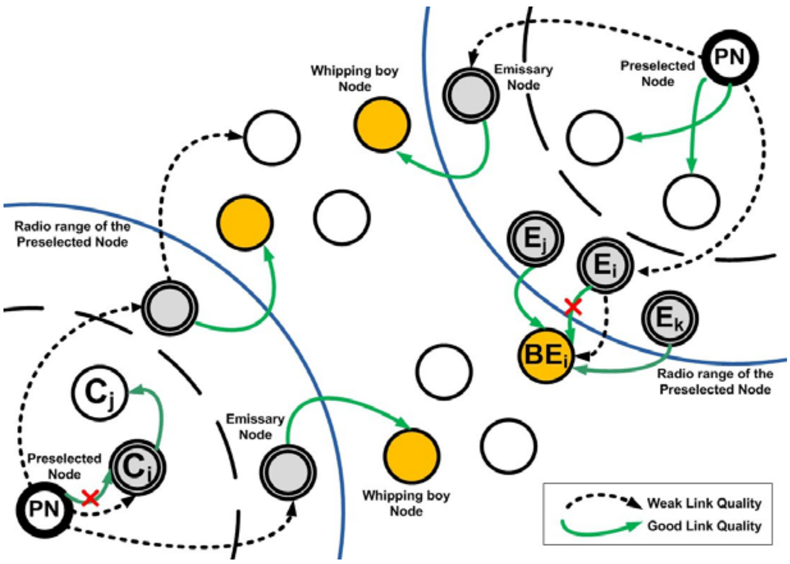

Fig. 28. Stability of LQI-DCP in unreliable link environments.

So, as we can see, in dense wireless sensor networks, our LQI-DCP protocol also supports the unreliability feature of the wireless links.

7. Energy Efficiency

LQI-DCP is designed for dense wireless sensor networks such as cold chain monitoring applications which consist of three main phases: the clustering formation phase, the clusterhead data collection phase and the routing phase (Fig. 29).

Since, the caryommes do not necessary form a connected backbone, all sensors wake up during the routing phase (Fig. 29) in which each caryomme aggregates the received alarms and then sends information towards the BS (Fig. 30). In the routing phase, only caryommes are sources of data packets. Other regular sensors are only participating in the routing effort by retransmitting received data towards the BS. The routing protocol used is the "Link Reliability based Routing Protocol" (L2RP) we have proposed in [23-24].

In the clustering formation phase LQI-DCP is composed of the first and second rounds, whereas MaxMin is composed of its clustering phases (initial, floodmax and floodmin phases), followed by the step of cluster formation with the SNCR mechanism.

The figure (Fig. 31) displays the clustering phase energy consumption for both protocols when the degree of connectivity criterion is used.

In the clustering phase, LQI-DCP provides lower energy consumption compared to MaxMin. This reflects the fact that LQI-DCP is an election in just two rounds, instead of $(2*d + 1)$ rounds for MaxMin. The emissary nodes are designated in the same packet which announces the preselected node, then the cost of the emissary selection mechanism is negligible. However, for the whipping boy node selection, an additional communication is necessary. But as the density of the first round elected nodes is low, and that the overall rate of caryommes is lower for LQI-DCP, this leads to lower energy consumption. It is the same for the data collection and routing phases as shown in [3].

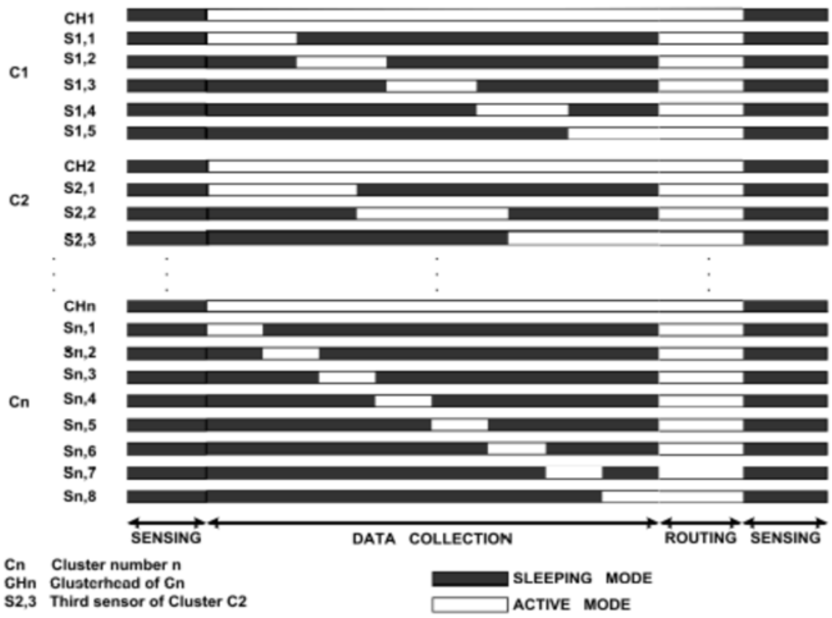

Fig. 29. Active/Sleep mode organization of the WSN [2].

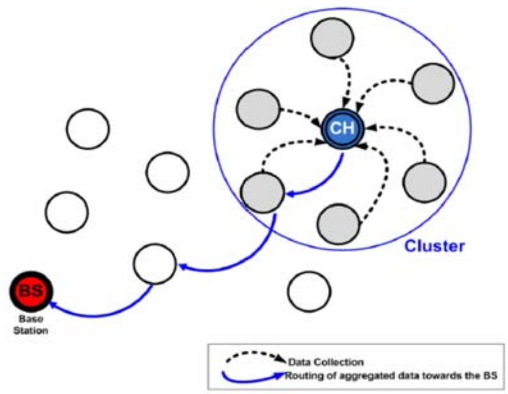

Fig. 30. Clusterhead data collection and routing toward the base station.

The Figs. 32 and 33 show for each protocol the ratio of the energy consumed by each phase during a complete cycle. For MaxMin and the routing phase, for example, it is the average energy consumed during the routing phase (caryommes produced by MaxMin) divided by the overall energy expenditure during one cycle for the same MaxMin protocol. This result depends on the selection criterion. The previous results in [3] have shown that MaxMin is more energy expensive whatever the phase considered and the selection criterion used. However, if one compares the phases within each protocol, the proportion spent by the routing phase (Figs. 32 and 33) is more important in LQI-DCP (60 %) than in MaxMin (55 %).

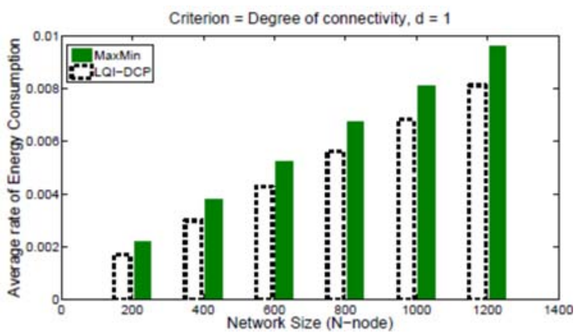

Fig. 31. Average rate of energy consumption (Clustering Phase, d=1).

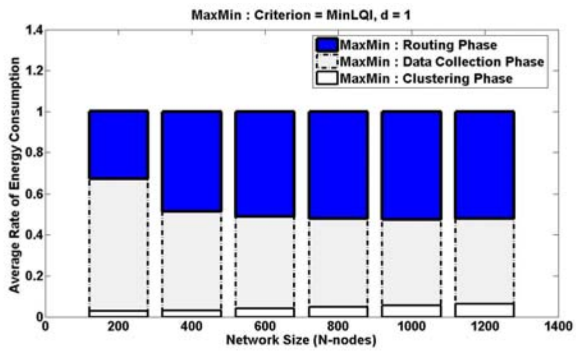

Fig. 32. MaxMin: Average ratio of energy consumption per phase (d=1).

This is due again to the fact that caryommes are better positioned in LQI-DCP than in MaxMin. Indeed, the weak position of caryommes produced by MaxMin has the effect of increasing the energy effort needed to collect data. The caryommes produced by MaxMin more often hear communications which are not intended to them. In LQI-DCP, as caryommes are more evenly distributed geographically, the proportion of energy needed to collect data is lower.

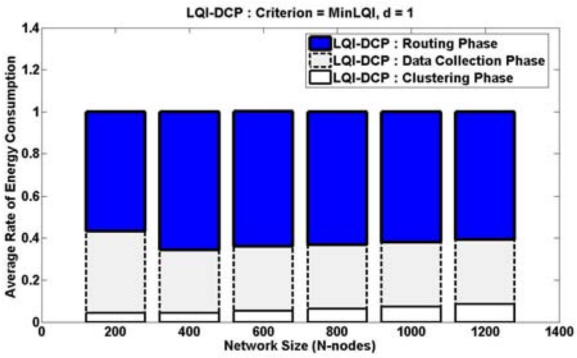

Fig. 33. LQI-DCP: Average ratio of energy consumption per phase (d=1).

7. Conclusions and Future Work

This paper complements our previous contributions in [1-3]. Firstly, there are many WSN deployment strategies. Each of which depends on the nature and the objective for which the application is designed for. However, the deployment strategy and clustering protocol efficiency are so closely bound together that good performance depend on how the protocol follows up the properties of the deployment topology.

Thus, we show how MaxMin is not fully compatible with the prevalent grid deployment topology. So, because of the smoothness of this topology, MaxMin fails with most of the criteria used in clusterhead selection such as "Degree of connectivity", "node id", "MinLQI", and "Proximity-BS". Then, the only way to use MaxMin in a grid deployment topology is to choose a randomized criterion function. However, in doing so, it becomes impossible to choose the most appropriate criteria for a specific application.

Then, we complete the LQI-DCP contribution with some results which show that this protocol fully supports the grid deployment topology. LQI-DCP is also high performance in environments subjected to high unreliabilities of the wireless links. This property is important for a LQI based multihop clustering protocol such LQI-DCP which is more energy efficient than MaxMin. In LQI-DCP, as caryommes are more evenly distributed geographically, the average of overall energy needed for network operations (clustering, data collection and routing processes) is less important than MaxMin.

Finally, it can be noted that security issues and solutions [25] have not been addressed here. Thus, in our future work, we will be interested in the aspects of securing the LQI-DCP protocol while taking care to minimize energy consumption.

Acknowledgements

This research was supported by:

- SAMOVAR CNRS Research Lab – UMR 5157; DeptRéseauxet Services de Télécommunications (RST); TélécomSudParis, Evry, France. I would like to thank Prof. Monique Becker and Prof. Michel Marot of TélécomSudParis. I am more than grateful to them for their help. (http://www.telecom-sudparis.eu/).
- Centre d'ExcellenceenMathématiques, Informatiqueet TIC (CEA-MITIC); UFR Sciences appliquées et de Technologies (UFR SAT), Université Gaston Berger, Saint-Louis, Sénégal. (http://www.ceamitic.sn/).

References

[1]. C. Diallo, Effects of the WSN deployment environment on MaxMin and LQI-DCP multihop clustering protocols, in *Proceedings of the 2nd International Conference on Advances in Sensors, Actuators, Metering and Sensing (ALLSENSORS'17),* Nice, France, March 2017, pp. 24-29.

[2]. C. Diallo, M. Marot, M. Becker, Single-node cluster reduction in WSN and energy-efficiency during cluster formation, in *Proceedings of the 9th IEEE/IFIP Annual Mediterranean Ad Hoc Networking Workshop, Med-Hoc-Net*, Juan-Les-Pins, France, June 2010, pp. 1-10.

[3]. C. Diallo, M. Marot, M. Becker, A distributed link quality based d-clustering protocol for dense ZigBee sensor networks, *in Proceedings of the Third IFIP/IEEE Wireless Days International Conference, (WD'10)*, Venice, Italy, October 2010, pp. 1-6.

[4]. N. Assad, Optimisation du déploiement des réseaux de capteurs sans fil: couverture de la zone de surveillance et connectivité du réseaudansune application de détectiond'intrusion, PhD Dissertation,*Faculté des Sciences de Rabat, Université Mohammed V Rabat*, 2015.

[5]. C. Diallo, Techniques d'amélioration du routage et de la formation des clusters multi-sautsdans les réseaux de capteurssans fil, PhD Dissertation, *TélécomSudParis,* 2010.

[6]. C. Diallo, M. Marot, M. Becker, Using LQI to improve clusterhead locations in dense ZigBee based wireless sensor networks, in *Proceedings of the 6th IEEE International Conference on Wireless and Mobile Computing, Networking and Communications (WiMob'10),* Niagara Falls, Canada, October 2010, pp. 137-143.

[7]. A. D. de Clauzade de Mazieux, M. Marot, M. Becker, Correction, generalisation and validation of the "Max-Min d-cluster heuristic", in *Proceedings of the IFIP/TC6/LNCS NETWORKING,* Atlanta, USA, May 2007.

[8]. A. Amis, R. Prakash, T. Vuong, D. Huynh, Max-Min d-cluster formation in wireless ad hoc networks, in *Proceedings of the 9thIEEE Annual Joint Conference on Computer and Communications Societies*, Vol. 1, 2000, pp. 32-49.

[9]. M. T. Sow, C. Diallo, Energy over-consumption induced by securing network operations, in *Proceedings of the 2nd IEEE International Conference on Frontiers of Sensors Technologies, IEEE-ICFST'17*, Shenzhen, China, April 2017, pp. 154-160.

[10]. A. Makhoul, Réseaux de capteurs: localisation, couverture et fusion de données, PhD Dissertation, *l'Université de Franche-Comté,* 2008.

[11]. A. Delye, Etude théorique des clusters multi-sautsdans les réseaux de capteurs sans fils, in Thèse de Doctorat*, Université(Paris VI),* France, 2007.

[12]. M. Marot, Conception etanalyse de méthodesd'agrégation et multiniveauxdans les réseaux, in Habilitation à Diriger des Recherches (HDR), *Université Pierre et Marie Curie (Paris VI),* 2009.

[13]. D. Baker, A. Ephremides, The architectural organization of a mobile radio network via a distributed algorithm, in *IEEE Transactions on Communications,* Vol. 29*,* No. 11, 1981, pp. 1694-1701.

[14]. A. Ephremides, J. Wieselthier, D. Baker, A design concept for reliable mobile radio networks with frequency hopping signaling, in *Proceedings of the IEEE,* Vol. 75, No. 1, 1987, pp. 56-73.

[15]. J. Blumenthal, R. Grossmann, F. Golatowski, D. Timmermann, Weighted centroid localization in ZigBee-based sensor networks, in *Proceedings of the IEEE International Symposium on Intelligent Signal Processing (WISP'07),* 2007, pp. 1-6.

[16]. M. Becker, A.-L. Beylot, R. Dhaou, A. Gupta, R. Kacimi, M. Marot, Experimental study: Link quality and deployment issues in wireless sensor networks, in *Proceedings of the NETWORKING'09, LNCS,* 5550, Aachen, Germany, 2009, pp. 14-25.

[17]. Tmote Sky datasheet, http://www.moteiv.com/products/docs/tmote-skydatasheet.pdf

[18]. C. Radio, http://www.chipcon.com

[19]. Wireless medium access control (MAC) and physical layer (PHY) specifications for low-rate wireless personal area networks (WPANs), IEEE Standard 802.15.4-2006, *IEEE Computer Society,* 2006.

[20]. ZigBee specification v1, *ZigBee*, June 2005.

[21]. S. S. World, http://www.sunspotworld.com.

[22]. E. W. S. Board, http://www.easysen.com/wieye.htm

[23]. C. Diallo, M. Marot, M. Becker, Link quality and local load balancing routing mechanisms in wireless sensor networks, in *Proceedings of the 6th Advanced International Conference on Telecommunications, (AICT'10),* Barcelona, Spain, May 2010.

[24]. C. Diallo, M. Marot, M. Becker, Efficiency benefits through load-balancing with link reliability based routing in WSNs, *International Journal on Advances in Networks and Services*, Vol. 3,No. 3-4, Feb. 2011.

[25]. C. Diallo, A. Sawaré, M. T. Sow, Security issues and solutions in wireless sensor networks, *International Journal of Computer Science and Information Security (IJCSIS),* Vol. 15, No. 3, March 2017.

Sensors & Transducers, Vol. 213, Issue 6, June 2017, pp. 24-29

Sensors & Transducers

Published by IFSA Publishing, S. L., 2017

http://www.sensorsportal.com

E-nose and E-tongue: an Analytical Tool for Quality Control and Management in the Pet Food Industry

[*] **Federica CHELI, Valentino BONTEMPO and Vittorio DELL'ORTO**

Department of Health, Animal Science and Food Safety, Università degli Studi di Milano, Via Trentacoste, 2, 20134, Milano

Tel.: +390250315734, fax: +390250315746

[*] E-mail: federica.cheli@unimi.it

Received: 30 May 2017 /Accepted: 28 June 2017 /Published: 30 June 2017

Abstract: In pet food production, the development of new products must take into account both nutritional and palatability aspects. Pet food palatability is related to the pet food sensory properties, such as aroma, flavour, texture shape, and particle size. The pet food industry may take advantage of a sensorial analysis as a powerful tool for quality control and management. The objective of this idea is to set up an electronic nose (e-nose) and tongue (e-tongue) as rapid quality control and research & development tools for the pet food industry. The final goal is to integrate e-nose and e-tongue with other sensing and imaging devices to 1) Ensure high pet food standards in terms of nutritional properties, palatability and acceptability; 2) Set up an instrumental protocol with good correlation to animal sensory properties in order to replace animal preference test, chemical and texture analysis.

Keywords: Pet food, Palatability, Electronic nose, Electronic tongue.

1. Introduction

The pet food industry offers a wide range of products to satisfy pet's and owner's requirements. Maintaining the health of dogs and cats by feeding wholesome nutritional diets is becoming an important component of responsible pet ownership [1]. In pet food production, the development of new products must take into account both nutritional and palatability aspects. Pet food palatability is related to the pet food sensory properties, such as aroma, flavour, texture shape, and particle size [2]. Pet food formulation is one of the factors affecting its aromatic profile that is strictly associated with palatability and acceptability. Sensorial analysis of pet food may be conducted by using several hedonic and analytical methods (Fig. 1) [3].

Although taste and olfactory perceptions are not completely similar, dogs and cats use both taste and smell in food detection and selection [2, 4]. Besides ingredient composition, pet food palatability may be affected by the use of palatability enhancers and food processing.

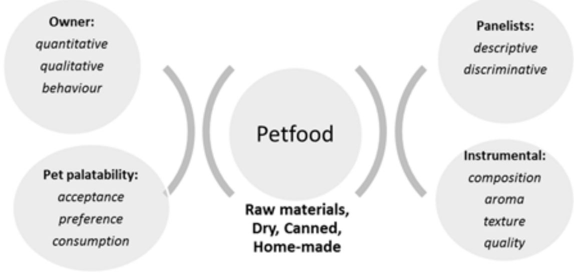

Fig. 1. Pet food sensory analysis research methods.

Microbial growth, oxidation, and the presence of undesirable compounds and contaminants represent risk factors responsible of changes in aroma, flavours, and loss of palatability [5]. At the industry level, adoption of a rapid, low-cost, high-throughput and on-line analytical approach is needed at all stages of pet food production and processing in order to guarantee and standardize the quality of the production.

The objective of this idea is to set up an integrated e-nose and e-tongue technology as a rapid quality control and research & development tool for the pet food industry, focusing on protein source characterization in pet food. To develop the idea, a step by step procedure must be designed: knowledge of e-nose and e-tongue characteristics and applications in the pet food industry, proper selection of an appropriate e-nose and e-tongue system for the specific application, and analysis of critical points for the use of the e-nose/e-tongue in an integrated system for quality control and research & development.

2. Pet Food Industry in the Society

The global market of the pet food industry has been a US$75 billion dollars business in 2016, with North America dominating the market [6]. Of that market, dog food accounts for over half and cat food 35 %. An overview of pet food industry and pet animals in Europe is reported in Table 1 [7].

Table 1. Europe: pet animals and pet food industry in society.

Main topics	Values
Dog population	80 million
Cat population	100 million
Estimated number of European households owning at least one pet animal	75 million
Number of pet food producing companies	650 plants
Employment	Direct employment pet food industry: 80.000 Indirect employment: 700.000
Annual sales of pet food products	Volume: 9 million tons Turnover: € 15 billion
Annual value of pet related products and services	€ 6.5 billion accessories € 8.5 billion services Total: € 15 billion
Annual growth rate of the pet food industry (average value over the past 3 years)	1.8 %

All these data support the need of analytical methods for a rapid analysis of pet food characteristics and properties. As many characteristics that directly determine the effective quality and/or safety of a pet food are often aspects of or described by its odour/aroma/taste, and we believe that electronic nose and tongue may be able to meet the requirements of the pet food industry.

3. The Electronic Nose and Electronic Tongue

E-nose and e-tongue have been increasingly used in the food industry as rapid and reliable tools for quality assessment [8]. The e-nose is an instrument that comprises an array of electronic chemical sensors, with partial specificity and an appropriate pattern recognition system, capable of recognizing simple or complex volatile organic compounds' (VOCs) patterns associated to a product odour [9]. The conventional aroma analysis by gas chromatography–mass spectrometry (GC–MS) is too time-consuming, complex and labour-intensive for routine quality application. Compared to GC-MS, e-nose presents several advantages for manufacturers and processors (portable, ease to use, rapid response and low costs), which make it a powerful tool for screening analysis to address the needs for routine quality testing in the food industry. Therefore, the major differences between e-nose and standard analytical chemistry equipment are that e-nose

1) Produces a qualitative output;
2) Can often be easier to automate;
3) Can be used in real-time analysis;
4) Can be easily integrated in current production processes.

The electronic tongue (e-tongue) has been developed in the last decade to evaluate the taste of liquid media. The common principle of the different e-tongue technologies is the application of an array of non-specific chemical sensors with partial specificity (cross-selectivity), coupled with chemometric processing, for recognizing the qualitative and quantitative composition of multispecies solutions [10]. To analyse results, similar pattern recognition techniques are needed for both the e-nose and e-tongue.

In literature, the applications of the e-nose and e-tongue in pet food analysis are very scarce. This could be attributed to the need to tune either the hardware and/or software to a specific application, or because data are kept confidentially by the product developers. E-nose associated or not with e-tongue has been used in studies for the standardization of a product development process, and in the quality control of the finished product [11-15]. In a study carried out in our department on commercial dry complete and dietetic dog and cat pet food, the e-nose was able to discriminate samples, although not completely, according to the species (dog *vs* cat), to the pet food formula (complete and balanced vs dietetic). Interestingly, e-nose was able to discriminate complete pet food for puppies or adult dogs (Fig. 2) [15].

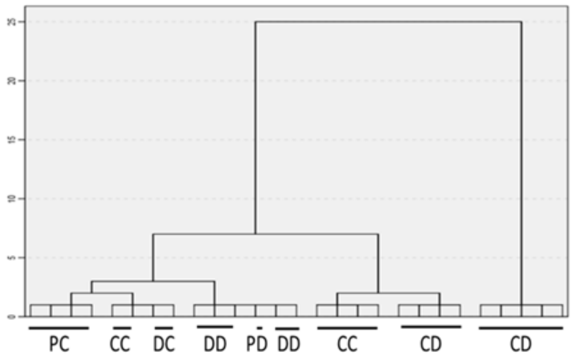

Fig. 2. E-nose for dry pet food analysis (PC: puppy complete; DD: dog complete; CC: cat complete; PD: puppy dietetic; DD: dog dietetic CD: cat dietetic) (adapted from [9]).

In a study on commercial canned dog and cat pet food, similar results have been reported, with no complete discrimination obtained with e-nose analysis. A combination of e-nose and e-tongue determined a better discrimination between samples [13].

Although inconsistent results have been reported, e-nose and e-tongue may represent rapid and sensitive instrumental techniques for pet food evaluation [16]. However, to represent an effective tool for a rapid quality control and research & development in the pet food industry, the analytical platform still needs several improvements, such as the definition of the best sensors' array, the development of data fusion analysis systems, and a better understanding of the industrial needs. The final aim of this idea is to develop an analytical sensory platform able to ensure high pet food standards in terms of nutritional properties, palatability and acceptability. The development of an instrumental protocol with good correlation to animal sensory properties could replace animal preference test, and chemical and texture analysis.

4. The Idea: e-nose and e-tongue for Protein Source Characterization in Pet Food

4.1. Set the e-nose and e-tongue for the Specific Application

The pet food industry traditionally utilizes a wide range of animal protein sources including meat and bone meals, poultry meals, poultry by-products meals, and fish by-products [17]. While traditional options such as beef, lamb, chicken, turkey, salmon and white fish continue to make up the bulk of pet food proteins, exotic sources are increasingly in evidence. Selection of high quality protein ingredients, consumption rates and digestibility are critical points affecting pet health and also the nutritional sustainability of pet food production. Moreover, a successful pet food must taste good. The most nutritious food in the world is useless if it will not be eaten. Ingredients and pet food formulation affect its aromatic profile that is strictly associated with palatability and acceptability.

A proper selection of an appropriate e-nose and e-tongue system for a particular application must involve an evaluation on a case-by-case basis. E-nose and e-tongue selection for a particular application must necessarily include: the assessment of the selectivity and the sensitivity range of individual sensor arrays for a particular target VOCs' profile (i.e., related to pet food components and target organoleptic properties of the products) and chemical substances showing the basic taste qualities, unnecessary (redundancy) sensors with similar sensitivities, as well as sensor accuracy, reproducibility, response speed, recovery rate, robustness, and overall performance. Most of these steps are common points in a validation procedure.

In order to configure an e-nose and e-tongue for protein source characterisation, the different steps of the analytical workflow must be must be considered and set-up (Fig. 3).

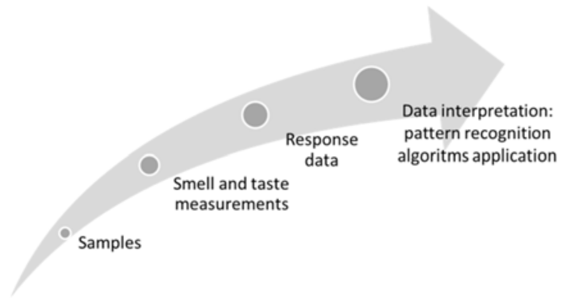

Fig. 3. E-nose and e-tongue analytical workflow.

The first step is the sample collection. Dry pet food containing different protein sources (poultry, mammalian, fish and no animal proteins) will be collected and divided into two subsets. One of the two subsets, training set, will be used to calibrate the model, and the other one, validation set, will be used to verify the robustness of the established model.

The second step is the set-up of a protocol for the analysis of the VOCs'profile and taste. VOCs analysis will be performed on a PEN3 model EN operating with an EDU2 enrichment and desorption unit (EDU) from Airsense Analytics GmbH (Schwerin, Germany) and equipped with a HSS 32 headspace autosampler (Perichrom Sarl, Saulx-Les-Chartreux, France). The sensor array consists of ten metal-oxide-semiconductors (MOS), which characteristics are listed in Table 2.

Samples will be analysed either with thermal desorption pre-treatments or without thermal desorption. All parameters involved in the headspace sampling and analysis will be optimized to obtain the best compromise between sensor responses and measurement time. The ratio G/G0 (where G and G0 are the resistance of a sensor in a detecting gas and in clean air, respectively) will be recorded by the e-nose dedicated software. For experimental purposes, three aliquots of each sample will be singularly analysed, and the mean value of the sensor signals from each aliquot will be calculated and recorded as a single odour profile.

Table 2. MOS Sensor Array of PEN 3.

Sensor name	Description	Reference
W1A - aromatic	Aromatic compound	Toluene, 10 mg/kg
W5B - broadrange	Broad range sensitivity reacts to nitrogen oxides and ozone very sensitive with negative signal	NO_2, 10 mg/kg
W3A - aromatic	Ammonia, used as sensor for aromatic compounds	Benzene, 10 mg/kg
W6B - hydrogen	Mainly hydrogen, selective (breath gases)	H_2, 100 mg/kg
W5A - arom-aliph	Alkanes, aromatic compounds, less polar compounds	Propane, 1 mg/kg
W1B - broad-methane	Sensitive to methane (environment) ca. 10 mg/kg. Broad range, similar to No. 8	CH_4, 100 mg/kg
W1C - sulphur-organic	Reacts on sulphur compounds H_2S 0.1 mg/kg	Sensitive to many terpenes and sulphur organic compounds, which are important for smell, limonene, pyrazine
W2B - broad-alcohol	Detects alcohols, partially aromatic compounds, broad range	CO, 100 mg/kg
W2C - sulphur-chlor	Aromatics compounds, sulphur organic compounds	H_2S, 1 mg/kg
W3B - methane-aliph	Reacts on high concentration > 100 mg/kg, sometimes very selective (methane)	H_4, 10 mg/kg

An Astree e-tongue (Alpha-MOS, Toulouse, France) with a liquid auto sampler unit will be used to measure the taste characteristics of the liquid samples. The sensor array consists of one reference electrode (Ag/AgCl) and 7 liquid cross selective sensors. All parameters involved in sample preparation and analysis will be optimized to obtain the best compromise between sensor responses and measurement time. For experimental purposes, for each sample three parallel measurements will be performed. The raw e-tongue sensor values will be saved in the form of relative resistance changes.

The last step is the feature extraction and data processing. Pattern recognition systems (principal component analysis - PCA; linear discriminant analysis - LDA) will be employed to select variables and build a model to improve the sample discrimination analysis and create models to be used as quality control process tools. Moreover, e-nose and e-tongue data will be dragged into a unique model. The results will be given as percentage of correctly classified samples.

Results from the e-nose and e-tongue will allow to identify the best analytical protocols for protein source in pet food, and to evaluate the capability of e-nose and e-tongue to classify pet food samples into different clusters based on different protein source components. Besides pet food composition, the set up and validation protocol could be used for enhancing the performance of the sensor system for a "total quality evaluation" extending the range of applications of e-noses in the food industry.

4.2. Pet Food Industry: Requirement and Critical Points for e-nose and e-tongue Analysis

When the pet food industry studies and designs new products, it must consider that there are two "consumers": the pet and the owner. A pet owner buying prepared pet food has two prime concerns: the product must provide a healthy diet and the pet must enjoy eating it. The second critical topic is the nutritional objective: a high quality pet food must be formulated and designed according to the type of pet, its size, age, activity and nutritional status. Pet food safety is another important topic, but safety is now a prerequisite for the pet food industry. Therefore, according to The European Pet Food Industry Federation, quality and safety, nutritional balance and palatability, variety and value for money, pet owner demands, and convenience are the important elements for pets and their owners [18]. Feed material selection, processing, production techniques for canned or dry products, and final product quality and palatability control represent the critical processing points, which need and may take advantage from a real-time monitoring by the use of e-nose and/or e-tongue. Besides quality control, e-nose and e-tongue may be used for research & development purposes in the pet food. Regarding this point, several hot topics may be suggested (Table 3).

4.3. E-nose and e-tongue in an Integrated System for Pet Food Evaluation

Domestic dogs and cats have different nutritional requirements and feeding behaviours, are sensitive to numerous palatability drivers, and differ in the food characteristics that they find desirable. Cats are strongly affected by the aroma of a food, and carefully smell a new food before tasting it. Dogs often prefer foods that are high in fat and include protein from animal sources. For both dogs and cats, the texture, size, and shape of food pieces are important aspects; scientists who study palatability refer to this as *"mouth feel"*. Therefore, e-nose and e-tongue should be integrated in an instrumental platform to develop the full potential of an electronic sense analysis of pet food. Multi-sensor data fusion is an available technology capable of combining information from several sources in order to form a unified picture that can be used as a "finger print" of a product. A practical and general data fusion system model capable of handling data from various applications must be established on the basis of feature extraction. The final goal is to create a high-level fusion, namely decision-making fusion, able to analyse the features from each analytical system first, and then to associate these features to produce a fused result.

Table 3. Pet food industry: e-nose and e-tongue for research & development.

Main topics	Application areas
Composition	Evaluation of protein sources (animal vs vegetal), lipid sources, …
Safety	Analysis of off-odours as markers of contamination (toxins, …), degradation, oxidation, … Measurement of product stability and shelf life
Palatants	Flavour profile of new palatants for pets and identifications of key aromas and taste attributes Development of new pet food palatants
Palatability	Replace animal preference test, chemical and texture analysis Development of highly palatable pet food for: puppies, senior pet, dietetic pet food, etc. Enhance palatability of pet food: dry, semi-dry, wet
Packaging	Effects on aroma and taste, evaluation of the shelf life
Brand	Characterisation of a quality brand

5. Conclusions

The pet food industry may take advantage of an appropriate e-nose and e-tongue system as a powerful tool for both quality control and research & development purposes. Future work is needed on the materials' side (sensors' array), on the data analysis side (better modelling, development of data fusion analysis for the process control system for a continuous quality assurance), and on the industrial side (better understanding of the industrial needs related to quality control and monitoring of food processing). Moreover, to develop the full potential of an electronic sense analysis of pet food, e-nose and e-tongue could be integrated in an instrumental platform including electronic sensors for colour, texture, size, and shape evaluation. Once properly set, this platform could replace animal preference test, chemical and texture analysis to assess pet food palatability.

References

[1]. V. Bontempo, Nutrition and Health of Dogs and Cats: Evolution of Petfood, *Veterinary Research Communication*, Vol. 29, Issue 2, 2005, pp. 45-50.

[2]. K. Koppel, Sensory analysis of pet foods, *Journal of the Science of Food and Agriculture*, Vol. 94, Issue 11, 2014, pp. 2148-2153.

[3]. G. C. Aldrich, K. Koppe, Pet Food Palatability Evaluation: A Review of Standard Assay Techniques and Interpretation of Results with a Primary Focus on Limitations, *Animals*, Vol. 5, Issue 1, 2015, pp. 43-55.

[4]. B. Di Donfrancesco, K. Koppel, E. Chambers Iv., An initial lexicon for sensory properties of dry dog food, *Journal of Sensory Studies*, Vol. 27, Issue 6, 2012, pp. 498-510.

[5]. K. Koppel, K. Adhikari, B. Di Donfrancesco, Volatile Compounds in Dry Dog Foods and Their Influence on Sensory Aromatic Profile, *Molecules*, Vol. 18, Issue 3, 2013, pp. 2646-2662.

[6]. D. Phillips-Donaldson, Global pet food sales update: ending 2016 on a high note, pet food industry 2016 (http://www.petfoodindustry.com/blogs/7-adventures-in-pet-food/post/6207-global-pet-food-sales-update-ending-2016-on-a-high-note).

[7]. FEDIAF The European Pet Food Industry, Facts & Figures, 2014 (http://www.fediaf.org/who-we-are/facts-and-figures.html).

[8]. A. R. Di Rosa, F. Leone, F. Cheli, V. Chiofalo, Fusion of electronic nose, electronic tongue and computer vision for animal source food authentication and quality assessment - A review, *Journal of Food Engineering*, in press, 2017.

[9]. J. W. Gardner, P. N. Bartlett, A brief history of electronic noses, *Sensors Actuators B: Chemical*, Vol. 18-19, Issue 1, 1994, pp. 210-211.

[10]. D. Ha, Q. Sun, K. Su, H. Wan, H. Li, N. Xu, F. Sun, L. Zhuang, N. Hu, P. Wang, Recent achievements in electronic tongue and bioelectronic tongue as taste sensors, *Sensors Actuators B: Chemical*, Vol. 207, Part B, 2015, pp. 1136-1146.

[11]. F. Cheli, A. Campagnoli, L. Pinotti, F. D'Ambrosio, A. Crotti, Electronic nose application in animal protein sources characterisation in pet food, in *Proceedings of the LXI Annual Meeting of the Italian Society for Veterinary Science, Salsomaggiore Terme (PR)*, Italy, 26-29 September 2007, pp. 26-29.

[12]. B. Oladipupo, J. Stough, N. Guthrie, Application of combined electronic nose and tongue technology in petfood flavor development and quality control, in *Proceedings of the AIP Conference,* New York City, (NY), USA, 2-5 May 2011, pp. 75-76.

[13]. V. Éles, I. Hullár, R. Romvári, Electronic nose and tongue for pet food classification, *Agriculturae Conspectus Scientificus*, Vol. 78, No. 3, September 2013, pp. 225-228.

[14]. V. Éles, *et al*., Electronic nose for evaluating cat food quality, in *Proceedings of the 16th International*

Symposium on Olfaction and Electronic Nose, June 2015, pp. 35-36.

[15]. D. Battaglia, M. Ottoboni, V. Caprarulo, L. Pinotti, F. Cheli, Electronic nose in commercial pet food evaluation, in *Proceedings of the II International Congress Food Technology, Quality and Safety and XVI International Symposium Feed Technology*, October 2014, pp. 28-30.

[16]. F. Cheli, M. Novacco, V. Bontempo, V. Dell'Orto, Pet Food Industry: E-nose and E-tongue Technology for Quality Control, in *Proceedings of the 2st International Conference on Advances in Sensors, Actuators, Metering and Sensing (ALLSENSORS 2017)*, Nice, France, 19-23 March, 2017, pp. 5-7.

[17]. A. Thompson, Ingredients: where pet food starts, *Top Companion Animal Medicine*, Vol. 23, Issue 3, 2008, pp. 127-132.

[18]. FEDIAF The European Pet Food Industry (http://www.fediaf.org/).

Sensors & Transducers, Vol. 213, Issue 6, June 2017, pp. 30-37

Sensors & Transducers
Published by IFSA Publishing, S. L., 2017
http://www.sensorsportal.com

Comparative Analysis of Shift Registers in Different Nanometer Technologies

Rajesh MEHRA, Ayushi GAGNEJA and Priya KAUSHAL
NITTTR Chandigarh, 160019, India
E-mail: rajeshmehra@yahoo.com, splendid.ayushi@gmail.com, pkaushal2407@gmail.com

Received: 8 May 2017 /Accepted: 8 June 2017 /Published: 30 June 2017

Abstract: In this paper, power and speed efficient registers have been designed using different nanometer technologies. Serial in Serial out (SISO) and Serial in Parallel out (SIPO) shift registers are designed using 180 nm and 90 nm technologies. Both the design are analyzed and compared based on power, delay and power-delay-product (PDP). Present portable real time system demands high performance in terms of speed along with low power consumption. The concept of technology scale down has been used to optimize power and delay in booth designs. The schematic of SISO and SIPO has been developed using Cadence Virtuoso software and analysis has been performed using Analog Design Environment. It has been observed from simulation analysis that 90 nm based SISO design shows an improvement of 68.61 % in power and 54.92 % in delay as compared to 180 nm technology. Likewise SIPO design has shown an improvement of 67.75 % in power and 53.32 % in delay as compared to 180 nm technology.

Keywords: CMOS, Flip Flop, Shift register, SISO, SIPO, VLSI.

1. Introduction

The new era of technology had a great impact on the field of Very Large Scale Integration (VLSI), which is constantly under examination by many researchers throughout the world. It involves mainly reduction of delay and power consumption [1]. Due to high demand for portable electronics devices, the major concentration is on the low power systems. The amount of components on a chip are continuously increasing, thus resulting in a need of higher packing density. So with there exists another problem of rising power consumption. Thus in order to enhance the amount of battery life in portable devices and avoid overheating problem, it is very much important to reduce the total consumption of power. Therefore, it has become an eminent task for the designers to acknowledge the power consumption in complex Integrated Circuits (ICs) along with the delay parameter as well as energy. Further, power has turned into a crucial parameter which needs the concern and understanding of developer while designing any circuit in modern VLSI applications, notably for those designs utilizing small scaled Complementary Metal Oxide Semiconductor (CMOS) technologies [2]. Most vital component of the ICs for temporary storage of data is a Flip Flop. It stores a logical condition of one or more input signals using external clock [3]. Flip-flops are used in majority of computational circuits to store the data and provide adequate processing time to different circuits inside a system. In CMOS circuits,

D Flip Flop (DFF) is essential building block and is responsible for the delay and total power dissipation calculations of any electronic system. Shift registers, which are created with the help of D flip-flops, have their intensive applications in various VLSI fields. The design of a shift register includes an N-bit shift register, made out of N number of Flip Flops [4]. While working with digital circuits, it is required to remember that register based execution has high speed processing. The power and speed of the processor is determined with the help of number of register that processor has and the size of each register [5].

A register is a circuit with two or more D Flip Flops connected together such that they all work exactly in the same way and a single clock synchronizes all the flip flops [6]. Each of these flip-flops has the ability of storing a single logic i.e., 0 or 1. There are limited compositions of 0 and 1 that can be stored into a register. These combinations are called the state of the register. Flip-Flops can store data in multiple sizes like 4, 8, 16, 32 or even 64 bits. Thus, several Flip Flops are combined to store whole data which form register [7]. So, a shift register is actually a collection of flip-flops. Utmost essential utilization in shifting and storage of data in computers, calculators and other electronics systems such as two binary numbers before they are added together or to shift the data from either a serial to parallel or parallel to serial form [8]. Serial data across small distances of tens of centimeters, utilize shift register to obtain data into and out of microprocessors. Various factors, along with analog to digital converter, digital to analog converters, memory (digital storage), and display drivers, utilize shift registers to lower the amount of wiring in the circuit board [9]. Some counter circuits literally utilize shift register to develop repeating waveforms. Large shift registers usually act as the support of feedback generators for long time, so that they might look like pseudo-noise, random noise. The particular data latch that produce up a single shift register are all directed by a same clock (CLK) signal form them synchronous devices. Shift register IC's are usually given with a clear or reset connection so that they can be "SET" or "RESET" as appropriate. Fully custom 4-bit CMOS shift register consumes less power and less area as compare to semi-custom and auto generated designs [10].

2. Shift Register

All flip-flop is a binary cell which is able to storing one bit of information. A Register is built up by a group of flip-flop. A register made up of n flip-flop is an n-bit register. Fundamental function of a register to store the information sequence in digital system so that during any computing process logic element access it easily. As long as there is finite number of flip-flop in a register and every register is able to store a single 0 or 1 bit, so that a register can store finite number of 0-1 combinations. All of those combinations is known as state or content of that register. By using flip-flop data can be store bitwise but generally data does not carry out as single bits. Rather it is familiar to store data words of n bit in register with general word lengths of 4, 8, 16, 32 or even 64 bits. Hence, to store whole data words a register is made up using several number of flip-flops [11].

In registers single clock line is used to control all flip-flops that's why it is a synchronous circuits. The shift register is particular sequential logic circuits that is utilize to store or transfer sequence of bits (data) in binary form and after that "shifts" the bits out once at each clock pulse. It mainly compose of certain single bit "D-Type Data Latches", for every bit (0 or 1) joined proper in a serial or daisy-chain layout so that output come out from one latch turn into the input of the next latch and go on. The data bits (0 or 1) can supply in or out of register serial manner, i.e. one follow the other from either the direction right or left, or in parallel, i.e. all composed [12].

2.1. Serial-in to Serial-out (SISO)

The number of bits to be stored in single shift register state the need for number of individual data latch used in that register. In serial shift register data is inserted serial form and read directly in a serial form from the output Q_D. In the circuit shown in Fig. 1, data are approved to progress over the register and out of the other end. Because there is only one output, the data go through the shift register one bit at a time in a serial pattern, accordingly the name Serial-in to Serial-Out Shift Register or SISO. The SISO structure is one of the easy configuration of the shift registers in that it has only three contact, the serial input (SI) which settle what enters the left hand flip-flop, the serial output (SO) which is caught from the output of the right hand flip-flop and the sequencing clock signal (Clk). Fig. 1 shows a generalized 4 bit serial-in serial-out shift register [13].

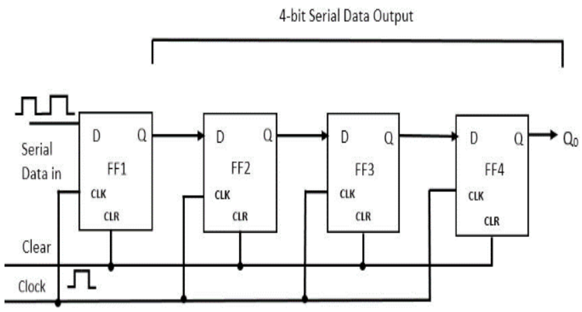

Fig. 1. Serial-In Serial-Out 4-bit Shift Register.

Assume that all the flip-flops (FFA to FFD) have just been RESET (CLEAR input) in Fig. 1 and that the output at logic level "0" i.e., no parallel data output. If a logic "1" is connected to the DATA input pin of FFA then on the first clock pulse the output is remain "0". The logic "1" has now moved or been "shifted" one place along the register to the right as it is now at QA. After the fourth clock "1" at the output will appear. Table 1 show propagation of logic "1".

SISO is the type of Shift Register that work as a temporary storage device or as a time delay device for the data, with the amount of time delay being controlled by the number of stages in the register, 4, 8, 16 etc. or by varying the application of the clock pulses [14].

Table 1. Movement of data through SISO shift register.

Clock Pulse No.	QA	QB	QC	QD
0	0	0	0	0
1	1	0	0	0
2	0	1	0	0
3	0	0	1	0
4	0	0	0	1
5	0	0	0	0

2.2. Serial-in to Parallel-out (SIPO)

Fig. 2 shows a 4-bit Serial-in to Parallel-out Shift Register. Initially RESET (CLEAR input) have been given to all flip-flops and then get logic level “0” at all the outputs Q_A to Q_B i.e., no parallel data output. If DATA input pin of FFA is connected to logic “1” then output of FFA is generated on first clock pulse and hence the output QA will be logic “1” set to HIGH along with the all other outputs still being at LOW logic “0”. Now suppose that the DATA input pin of FFA has restored LOW anew to logic “0” providing us one pulse or 0-1-0.

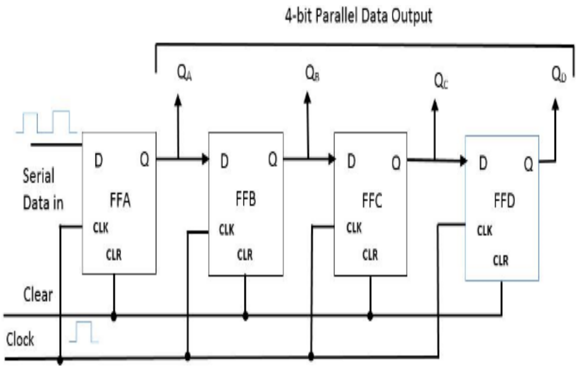

Fig. 2. Serial-In to Parallel-Out 4-bit Shift Register.

At second clock pulse output of FFA will change to logic “0” and the output of FFB i.e. QB HIGH to logic “1” as its input D has the logic “1” level on it from Q_A. Now the logic “1” has been “shifted” or moved one step in register to the right as it is now at Q_A. Whenever the third clock pulse came this logic “1” value shifted to the output of FFC (Q_C) and it goes on unless the fifth clock pulse arrive that set back again all the outputs QA to QD to logic level “0” as the input to FFA is maintained at logic level "0" [15].

The arrive of every clock pulse is to shift the data bits of each point one step to the right, and this is presented in below table unless the entire data sequence of 0-1-0-1 is saved in the register. Now, this data sequence can be get directly from Q_A to Q_B outputs. Hence data has been transformed from a serial data input to parallel data output. The truth table, shown in Table 2, shows the going on of the logics through the register from left to right with clock pulses. It is observe that after the fourth clock pulse, the 4-bits of data (0-1-0-1) are save in the register and will preserve rather providing clock of register has been stopped.

Table 2. Movement of data through SIPO shift register.

Clock Pulse No.	QA	QB	QC	QD
0	0	0	0	0
1	1	0	0	0
2	0	1	0	0
3	1	0	1	0
4	0	1	0	1
5	0	0	0	0

In practice the input data to the register may consist of various combinations of logic "1" and "0". The practical application of the serial-in/parallel-out shift register is to convert data from serial format on a single wire to parallel format on multiple wires for example to illuminate LEDs (Light Emitting Diodes) [16].

3. Schematic Design Simulation

Due to technology scaling the circuit of serial shift register is designed for different technology nodes in the Nano scale regime. The design also requires the use of different operating voltages for different technologies, like 1.8 V for 180 nm and 1.2 V for 90 nm technologies. Fig. 3 shows that these registers are constructed with the help of D flip flops, which again comprises of NAND gates.

D flip flops are connected serially so as to form the serial shift register, in which the input as well as output proceeds in a serial fashion. 4-bit SISO shift register schematic design is shown in Fig. 4 for all the technology nodes.

Analog simulation of designed SISO shift register has been performed for logic verification. The transient responses of proposed register, along with their power variations are shown in Fig. 5 and Fig. 6 for different nodes.

Fig. 7 and Fig. 8 show the DC response of SISO shift register for 90 nm and 180 nm technology nodes.

To improve the speed factor SIPO shift register schematic is designed as shown in Fig. 9. In this speed is more as the data is sent in a serial manner, while the output is taken out simultaneously, in a parallel fashion.

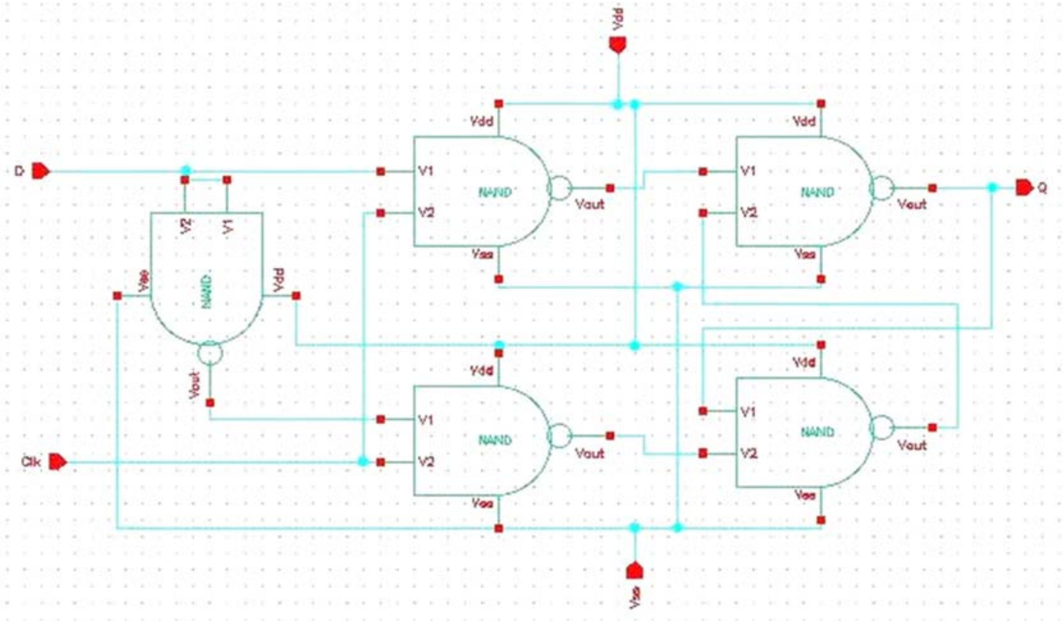

Fig. 3. Schematic Design of D Flip-Flop.

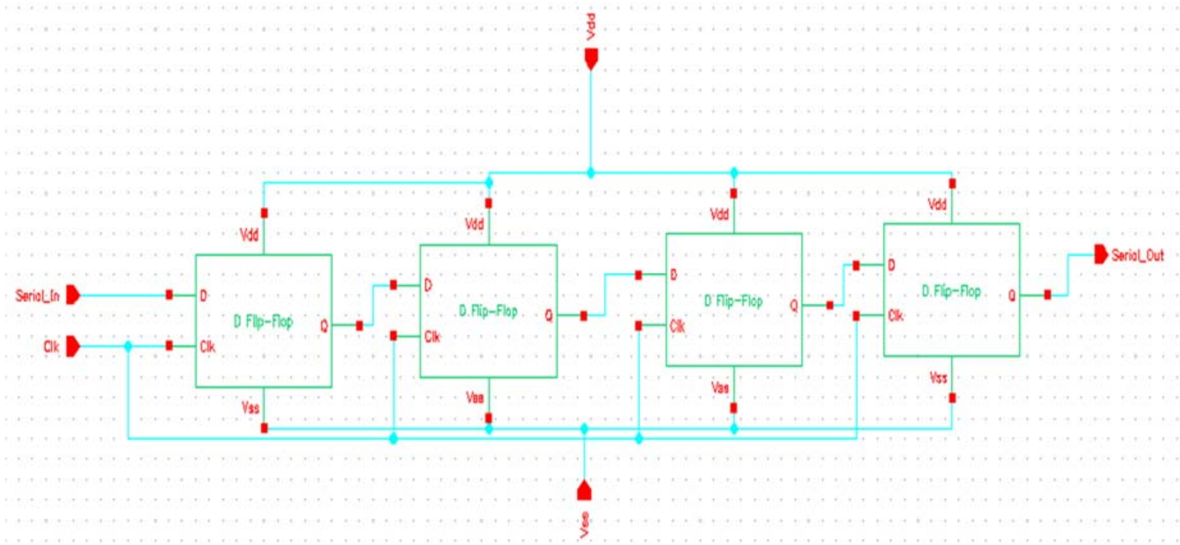

Fig. 4. Schematic of 4-bit SISO Shift Register.

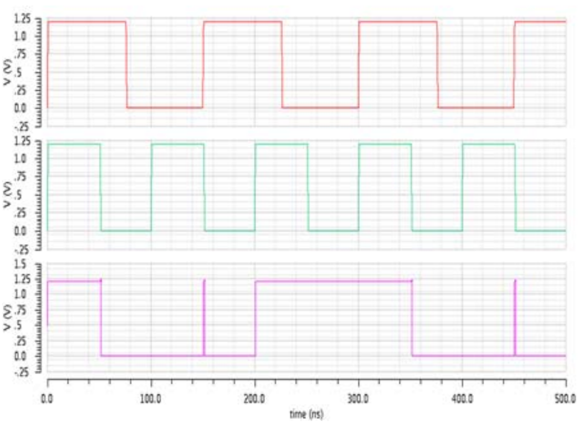

Fig. 5. Transient Response of SISO Shift Register in 90 nm Technology.

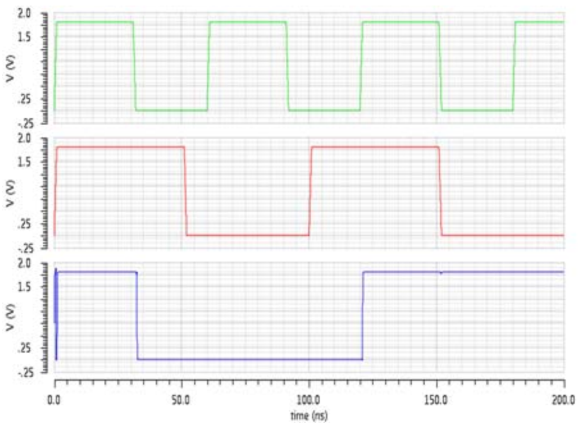

Fig. 6. Transient Response of Shift Register in 180 nm Technology.

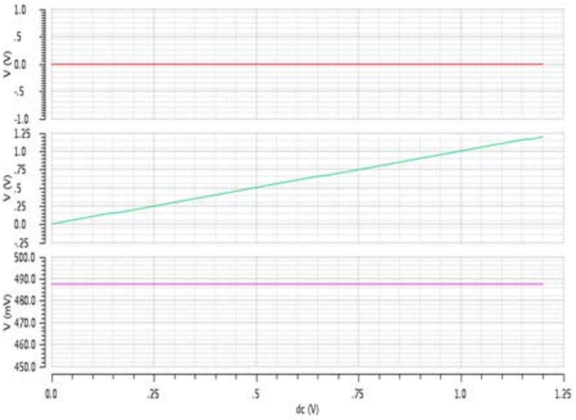

Fig. 7. DC Response of SISO Shift Register in 90 nm Technology.

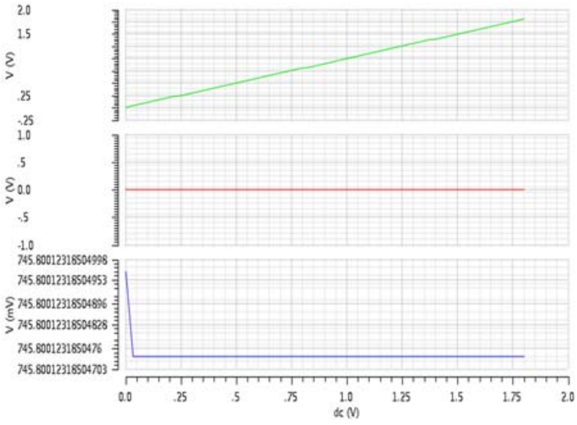

Fig. 8. DC Response of SISO Shift Register in 180 nm Technology.

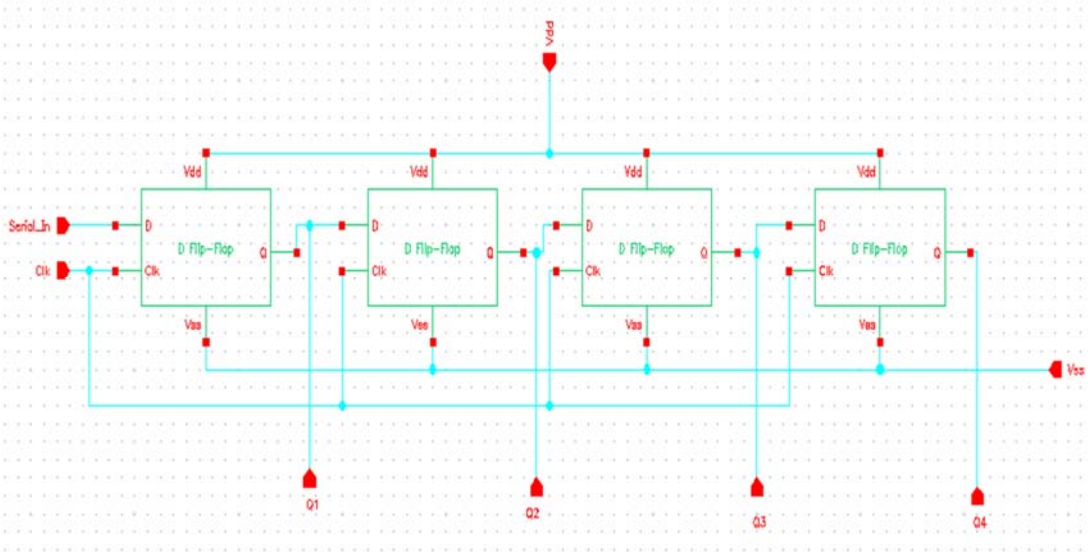

Fig. 9. Schematic of 4-bit SIPO Shift Register.

The logic of developed SIPO register has been verified using analog simulation. The transient responses of proposed SIPO register are shown in Fig. 10 and Fig. 11 for different nanometer technologies.

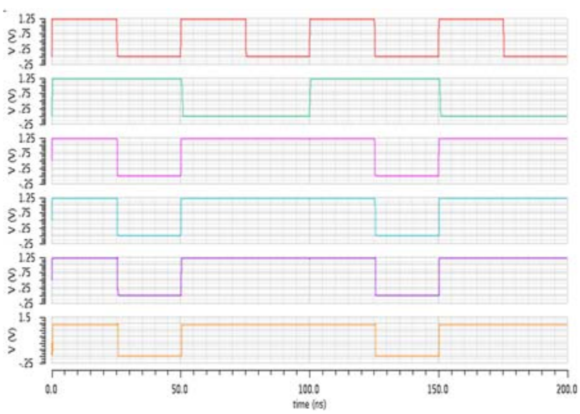

Fig. 10. Transient Response of SIPO Shift Register in 90 nm Technology.

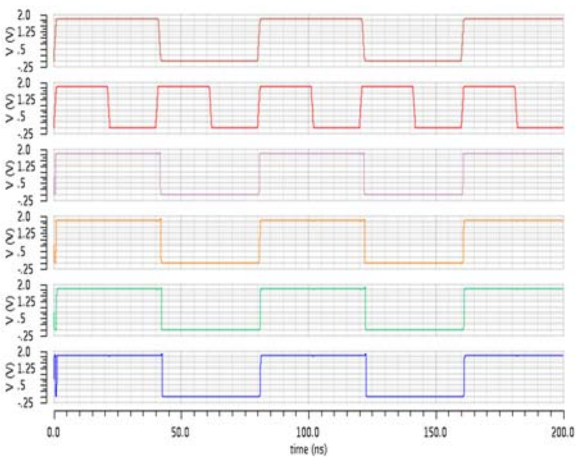

Fig. 11. Transient Response of SIPO Shift Register in 180 nm Technology.

Fig. 12 and Fig. 13 show the DC response of SIPO shift register for 90 nm and 180 nm technology nodes.

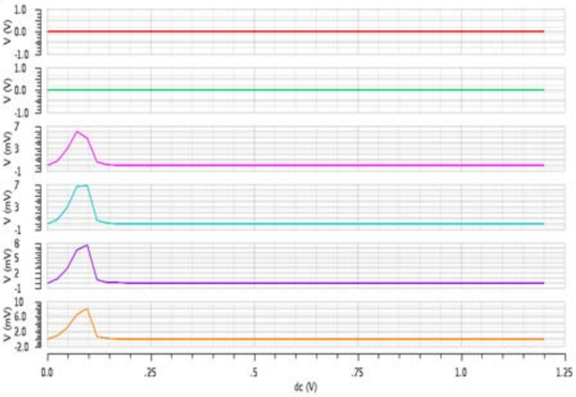

Fig. 12. DC Response of SIPO Shift Register in 90 nm Technology.

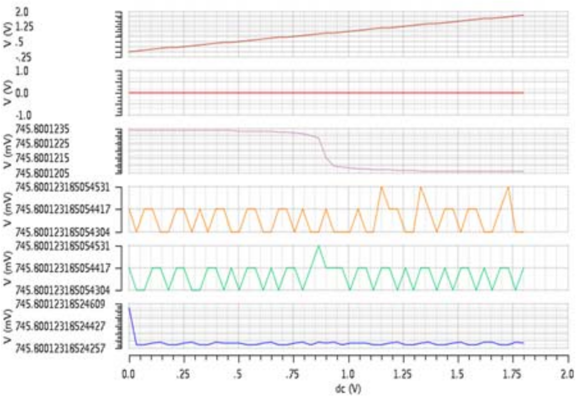

Fig. 13. DC Response of SIPO Shift Register in 180 nm Technology.

4. Performance Analysis

The schematic designs have been simulated for 90 nm and 180 nm technology nodes. Different parameters are taken into consideration for its evaluation. These are Power, Delay and Power-Delay-Product (PDP). The variation of the most essential parameter i.e., power with respect to time can be seen in Fig. 14 and Fig. 15 for SISO shift registers.

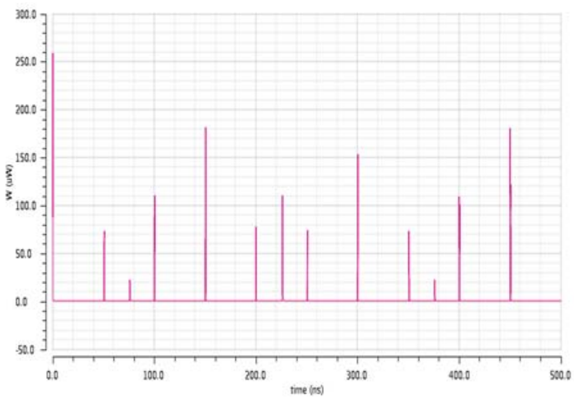

Fig. 14. Power Response of SISO Shift Register in 90 nm Technology.

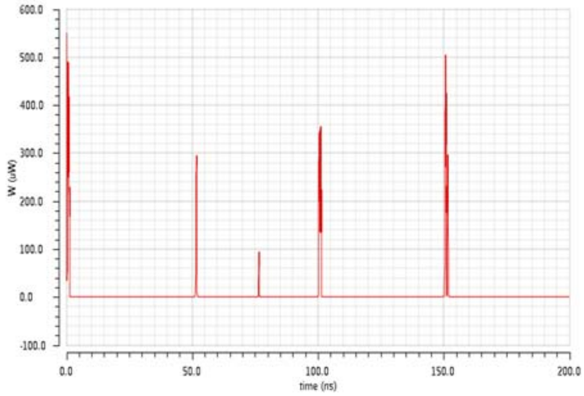

Fig. 15. Power Response of SISO Shift Register in 180 nm Technology.

Table 3 shows the parameter comparison for different technologies. It can be observed from the table that lower the technology node, lesser is the amount of power required by it and faster is the speed as the delay amount decreases significantly.

Table 3. Performance Analysis of Proposed SISO Design.

Parameter	180 nm	90 nm
Power	513 uW	161 uW
Delay	363.8 ps	164 ps
PDP	186.6 fJ	26.4 fJ

The parametric comparisons prove that SISO shift register works more efficiently for the 90 nm node. It thus shows that it consumes much less amount of power as compared to others and with also less amount of delay as well as PDP. The variation of power with respect to time is visualized in Fig. 16 and Fig. 17 for 90 nm and 180 nm technologies for SIPO shift register respectively.

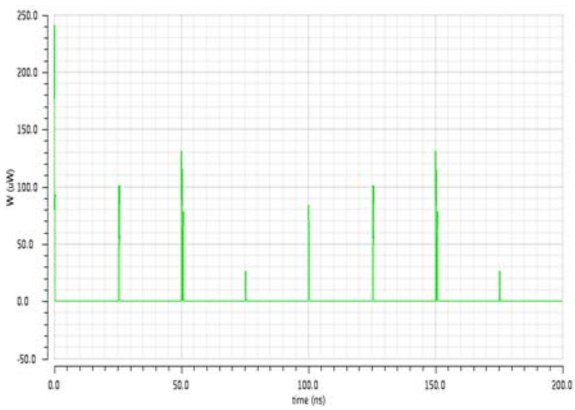

Fig. 16. Power Response of SIPO Shift Register in 90 nm Technology.

Fig. 18 shows that 90 nm design for SISO shift register has an improvement of 68.61 % power with respect to 180 nm technology. Fig. 19 depicts an improvement of 54.92 % delay from 180 nm technology. Fig. 20 represents that improvisation of 85.85 % in terms of PDP from 180 nm technology.

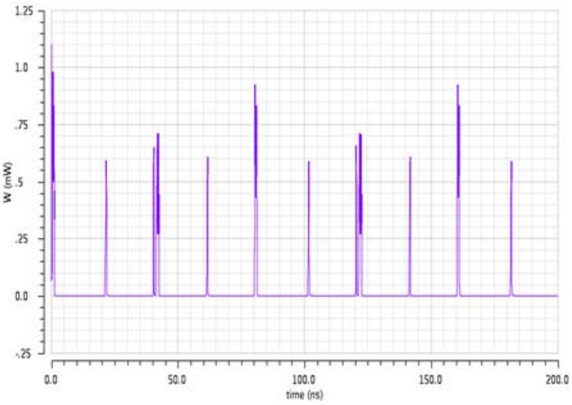

Fig. 17. Power Response of SIPO Shift Register in 180 nm Technology.

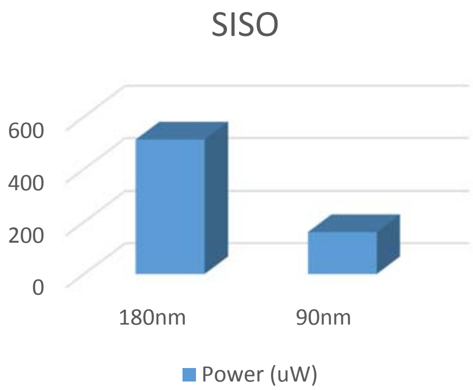

Fig. 18. Graphical comparison of Power consumption.

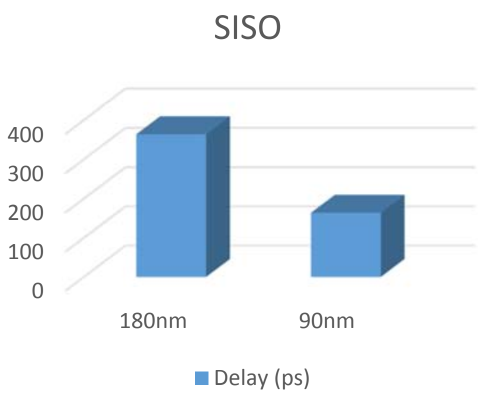

Fig. 19. Graphical comparison of Delay.

Table 4 shows parameter comparison of SIPO shift register for different nanometer technologies.

Fig. 21 shows that 90 nm design for SIPO shift register has an improvement of 67.75 % power with respect to 180 nm technology. Fig. 22 depicts an improvement of 53.32 % delay from 180 nm technology. Fig. 23 represents that improvisation of 84.97 % in terms of PDP with respect to 180 nm technology.

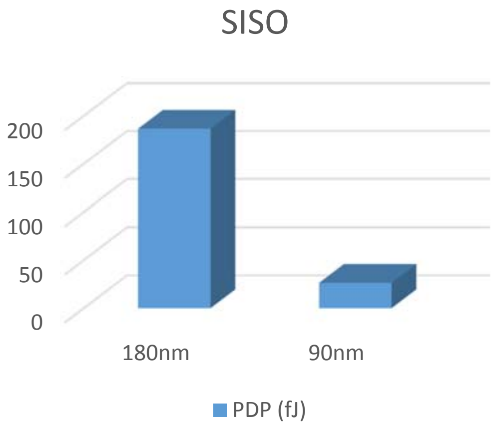

Fig. 20. Graphical comparison of PDP.

Table 4. Performance Analysis of Proposed SIPO Design.

Parameter	180nm	90nm
Power	549 uW	177 uW
Delay	321.4 ps	150 ps
PDP	176.4 fJ	26.5 fJ

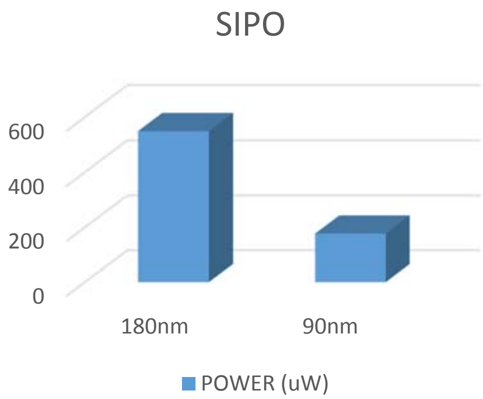

Fig. 21. Graphical comparison of Power.

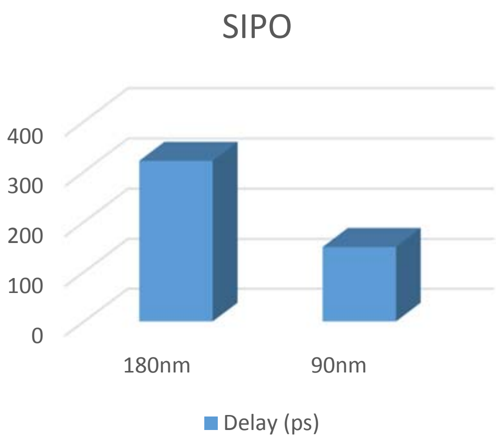

Fig. 22. Graphical comparison of Delay.

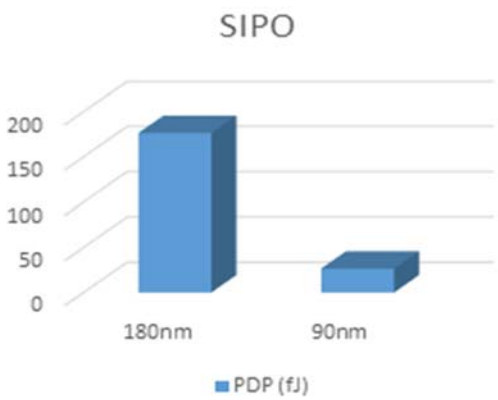

Fig. 23. Graphical comparison of PDP.

5. Conclusions

Power and delay optimized 4-bit serial shift registers are designed and analyzed by utilizing the concept of technology scaling. The proposed designs have been developed by using D Flip Flop modules based on optimized NAND gates. 90 nm technology based design shows vast improvement in terms of power, delay and Power-Delay-Product (PDP). The power consumption of 90 nm based SISO design is 161 uW as compared to 513 uW power in case of 180 nm technology. On the other hand 90 nm technology based SIPO design has shown 177 uW power consumption as compared to 549 uW in case of 180 nm technology. The SISO design has shown delay of 164 ps and 363.8 ps for 90 nm and 180 nm technologies respectively. The delay of SIPO based design are 150 ps and 321.4 ps for 90 nm and 180 nm technologies. So 90 nm technology based design show better results in terms of power consumption and delay.

References

[1]. R. Mehra, P. Kaushal, A. Gagneja, Area and Speed Efficient Layout Design of Shift Registers using Nanometer Technology, in *Proceedings of the 2nd International Conference on Advances in Sensors*, March 2017, pp. 58-62.

[2]. B. Nikoli´c, Design in the Power-Limited Scaling Regime, *IEEE Transactions on Electron Devices*, Vol. 55, Issue 1, January 2008, pp. 71-83.

[3]. S. Sharma, B. Kaushal, Shift Register Design Using Two Bit Flip-Flop, in *Proceedings of the IEEE Conference on Recent Advances in Engineering and Computational Sciences (RAECS)*, 2014, pp. 1-5.

[4]. D. J. Reddy, A. V. Paramkusam, A Novel Approach to Power Optimized Memory Organization by Using Multi-Bit Flip-Flops, *International Journal of Emerging Trends in Electrical and Electronics (IJETEE)*, Vol. 10, Issue 9, October 2014, pp. 2721-2725.

[5]. M. Arunlakshman, T. Dineshkumar, N. Mathan, Performance Evaluation of 6 Transistor D-Flip Flop based Shift Registers using GDI Technique, *International Journal of Advanced Research in Computer and Communication Engineering (IJARCCE)*, Vol. 3, Issue 3, March 2014, pp. 5858-5861.

[6]. P. K. Chakravarti, R. Mehra, Layout design of D Flip Flop for Power and Area Reduction, in *Proceeding of the Conference in International Journal of Scientific Research Engineering & Technology (IJSRET)*, March 2015, pp. 154-158.

[7]. B. D. Yang, Low-Power and Area-Efficient Shift Register Using Pulsed Latches, *IEEE Transactions on Circuits and Systems*, Vol. 62, Issue 6, June 2015, pp. 1564-1571.

[8]. N. Rapartiwar, V. Kapse, Design of Serial in Serial out And Serial in Parallel out Shift Register Using Double Edge Triggered D Flip Flop, *International Journal of Emerging Technology and Advanced Engineering (IJETAE)*, Vol. 4, Issue 7, July 2014, pp. 505-508.

[9]. F. Ahmad, M. Mustafa, N. A. Wani, F. A. Mir, A novel idea of pseudo-code generator in quantum-dot cellular automata (QCA), *International Journal for Simulation and Multidisciplinary Design Optimization (IJSMDO)*, Vol. 5, Issue 04, February 2014, pp. 1-8.

[10]. L. S. Kiran, M. Valarmathi, Design of Shift Registers using SEU tolerant Isolated-DICE latch, *International Journal of Engineering Research & Technology (IJERT)*, Vol. 4, Issue 4, April 2015, pp. 620-624.

[11]. M. A. S. Bhuiyan, H. N. B. Rosly, M. B. I. Reaz, K. N. Minhad, H. Husain, Advances on CMOS Shift Registers for Digital Data Storage, *TELKOMNIKA Indonesian Journal of Electrical Engineering*, Vol. 12, Issue 5, May 2014, pp. 3849-3862.

[12]. P. Srivastava, R. Mehra, Design Analysis of Area Efficient 4 Bit Shift Register Using CMOS Technology, *International Journal of Electrical and Electronics Engineering (IJEEE)*, Vol. 7, Issue 01, January 2015, pp. 26-30.

[13]. M. K. Singh, Rajeev Kumar, Simulation of Enhanced Pulse Triggered Flip Flop with High Performance Applications, *International Journal of Engineering Sciences & Research Technology (IJESRT)*, Vol. 4, Issue 1, January 2015, pp. 489-493.

[14]. D. I. Praveen, T. Ravi, E. Logashanmugam, Design and Analysis of High Performance Double Edge Triggered D-Flip Flop based Shift Registers, *International Journal of Emerging Technology and Advanced Engineering (IJETAE)*, Vol. 3, Issue 2, February 2013, pp. 274-278.

[15]. D. J Rennie, M. Sachdev, Novel Soft Error Robust Flip-Flops in 65nm CMOS, *IEEE Transactions on Nuclear Science*, Vol. 58, Issue 5, December 2011, pp. 2470-2476.

[16]. N. M. Nayeem, M. A. Hossain, L. Jamal, H. M. H. Babu, Efficient Design of Shift Registers Using Reversible Logic, in *Proceedings of the International Conference on Signal Processing Systems*, Singapore, May 2009, pp. 474-478.

Sensors & Transducers, Vol. 213, Issue 6, June 2017, pp. 38-45

Sensors & Transducers

Published by IFSA Publishing, S. L., 2017
http://www.sensorsportal.com

Study of Propylene Glycol, Dimethylformamide and Formaldehyde Vapors Sensors Based on MWCNTs/SnO_2 Nanocomposites

[1] Zaven Adamyan, [1] Artak Sayunts, [1] Vladimir Aroutiounian, [1] Emma Khachaturyan, [1] Arsen Adamyan, [2] Martin Vrnata, [2] Přemysl Fitl and [2] Jan Vlček

[1] Yerevan State University, Department of Physics of Semiconductors and Microelectronics, Center of Semiconductor Devices and Nanotechnologies, 1 A. Manoukian, 0025 Yerevan, Armenia

[2] University of Chemistry and Technology, Department of Physics and Measurement Technology, Technická 5, 166 28 Prague 6, Czech Republic

[1] Tel.: +37460710311, fax: +37460710355

[1] E-mail: kisahar@ysu.am

Received: 22 May 2017 /Accepted: 22 June 2017 /Published: 30 June 2017

Abstract: We present results of our research works related to the study of thick-film multiwall carbon nanotube/tin oxide nanocomposite sensors of propylene glycol (PG), dimethylformamide (DMF) and formaldehyde (FA) vapors derived using hydrothermal synthesis and sol-gel methods. Investigations of response/recovery characteristics in the 50-300 °C operating temperature range reveal that the optimal operating temperature for PG, DMF and FA vapor sensors, taking into account both high response and acceptable response and recovery times, are about 200 and 220 °C, respectively. A sensor response dependence on gas concentration in all cases is linear. The minimal propylene glycol and dimethylformamide gas concentrations at which the perceptible signal was registered by us were 13 ppm and 5 ppm, respectively.

Keywords: MWCNTs/SnO_2, Gas, Vapor, Sensor, Dimethylformamide, Propylene glycol, Formaldehyde.

1. Introduction

There are various harmful and hazardous matter vapors, which have a major role in diverse spheres such as environmental protection, industrial manufacture, medicine, as well as national defense. As an illustration, propylene glycol (PG) is an excellent solvent for many organic compounds and is used as an active ingredient in engine coolants and antifreeze, brakes, paints, enamels and varnishes, and in many products as a solvent or surfactant. It can also be found in cosmetics, perfumes, as well as in pharmaceuticals.

Another example is the dimethylformamide (DMF) which is used as a solvent in vinyl resins, adhesives, pesticide and epoxy formulations; which purifies and separates of acetylene, 1,3-butadiene, acid gases and aliphatic hydrocarbons, also in the production of polyacrylic or cellulose triacetate fibres and pharmaceuticals or in the production of polyurethane resin for synthetic leather [1].

Formaldehyde (FA) is a colorless, water-soluble gas with a pungent odor which used in making building materials and many household products such as particleboard, plywood and fiberboard, glues and adhesives, textiles, paper and their product coatings.

Besides, formaldehyde can serve an intermediate in the manufacture of industrial chemicals. It can also be found as a preservative in some foods and in products, such as antiseptics, medicines, and cosmetics [2].

DMF, PG and FA have a huge impact on human organs (e.g. liver, skin, eyes and kidneys [1-4]). PG can cause nausea and vomiting, headache, dizziness and fainting. Moreover, it is known as a combustible liquid, which can explode in fire. FA gas can cause burning sensations of the eyes, nose, and throat, coughing, wheezing, nausea, skin irritation. Besides, exposure to relatively high amounts of formaldehyde can increase the risk of leukemia and even cause to some types of cancer in humans.

Due to the information noted above, PG, DMF and FA gas sensors have a huge application for detecting and continuous monitoring of these gases, in the spheres where they are used.

As a result of our carefully conducted analysis of the literature data, we did not find any works related to research and development of resistive sensors of PG and DMF gases. There are only sensors working in other principle (for example sensors working on modification of color of the substance), which is incompatible for contemporary technic, while, resistive gas sensors made from metal oxides have advantages such as electric signal, measurement of concentration, small sizes, low power consumption, high sensitivity, and long reliability [5-7].

As opposed to this case, there are many various types of FA gas sensors. For instance, FA gas sensors based on graphene or polymers which are working at room temperature [8-9]. On the other hand, FA gas sensors based on metal-oxide materials have advantages mentioned above. However pure metal-oxide structures react on FA at higher operating temperatures (300-400 ^oC) [10-11] or at room temperature with the assistance of UV LED [12-13].

Nanomaterials, as carbon nanotubes (CNTs), metal-oxide nanoparticles, nanotubes, nanowires and other various nanopatterns formation [14-19] are widely used in gas sensing for their excellent responsive characteristics, mature preparation technology, and low cost of mass production. Due to the covering of CNTs walls with metal-oxide nanoparticles, specific surface area of such gas-sensitive nanocomposites increases more. Moreover, nanochannels in the form of hollows of CNTs promote penetration of gas molecules deeper down in the nanocomposite sensitive layer [20]. Hence, it can be expected that application in gas sensors technology of nanocomposite structures composed of metal oxide functionalized with CNTs should enhance the gas sensor parameters, such as gas response, response, recovery times, and operating temperatures.

Our recent works related to the study of gas sensors based on multiwall carbon nanotubes/tin oxide (MWCNTs/SnO_2) nanostructures are also argued in [17, 21-22]. The choice of tin oxide as a component of SnO_2/MWCNTs nanocomposite structure is conditioned by the fact that SnO_2 is well known and studied basic material for metal-oxide gas sensors (see, for example [5, 16, 23-24]). We expected that coating of functionalized MWCNTs with SnO_2 nanoparticles with admissible, (close to double Debay length) sizes [23-27] should provide the improved performance of the gas sensor and lowered the temperature of its operating.

Here, we present the characteristics of the PG, DMF and FA vapor sensors based on ruthenated thick-films MWCNT/SnO_2 nanocomposite structures. The choice of corresponding processing technique, treating conditions and regimes for CNTs functionalization, as well as modification of thick films surface with Ru catalyst, are described below in the second section. Results of the measurements of PG, DMF and FA vapor sensors and their discussions are given in the third section.

2. Experimental Development

MWCNTs/SnO_2 nanocomposite material processing and thick-film sensor manufacturing technology on the base of this nanocomposite are presented in this section. It is shortly described both the MWCNTs preparation and its covering with SnO_2 nanoparticles obtained by using the hydrothermal method. Ruthenium catalyst deposition technology is also shown here.

MWCNTs membranes which were used for the preparation of nanocrystalline MWCNTs/SnO_2 powder were kindly provided to us by our colleagues from the University of Szeged, Hungary. MWCNTs were prepared by the decomposition of acetylene (CVD method) using Fe, Co/$CaCO_3$ catalyst [28-29]. This growth procedure using $CaCO_3$ catalyst enables a highly efficient selective formation of clean MWCNTs, suitable for effective bonding between CNT and metal-oxide, particularly, for SnO_2 precursors.

For a functionalization of nanotube walls with oxygen-containing hydroxyl (OH), carbonyl (C=O), and carboxylic (COOH) functional groups, MWCNTs from the membranes were transferred to slurry in HNO_3/H_2SO_4 acids mixture during 1 h. Such a functionalization of the CNTs is very important and necessary for the following synthesis of SnO_2 nanoparticles on the MWCNTs walls since these oxygen-containing groups act as sites for the nucleation of nanoparticles. After rinsing with distilled water and drying at 80^{o}C, MWCNTs were poured and treated in deionized water in the ultrasonic bath for 5 min.

The preparation of nanocomposite materials with a hydrothermal method was carried out in two steps. Firstly, purified MWCNTs were dispersed in water via sonication. Then, a calculated amount of precursor of the $SnCl_2 \bullet 2H_2$ was dissolved in another beaker in water, whereupon 3 cm^3 HCl was added to the solution. The choice of water as a solvent, instead of e.g. ethanol, was preferably for us in the view of expected improvement in gas sensing characteristics, taking into account the fact that cover the overwhelming parts of CNTs with SnO_2 nanoparticles is ensured at that [30]. In the next step, the MWCNT's suspension and the solution of the precursor were mixed and sonicated for 30 min. For preparing the nanocomposites, we poured the above-mentioned solutions into autoclaves, where hydrothermal synthesis was carried out at 150 ºC for 1 day. At the end of this procedure, all obtained nanocomposite powders were filtered and dried at 90 ºC for 5 h. The final mass ratios of the nanocomposite MWCNTs/SnO_2 obtained with the hydrothermal method in this study were 1:200, respectively. The hydrothermal synthesis process is presented in details in [17, 31-32].

The paste for the thick film deposition made by mixing powders with α-terpineol ("Sigma Aldrich") and methanol was printed on the chemically treated surface of the alumina substrate over the ready-made Pt interdigitated electrodes. The thin-film Pt heater was formed on the back side of the substrate. Then, the obtained composite structures were cut into 3×3 mm pieces. After that, the drying and annealing processes of the resulting thick films were carried out in two stages: The first step is the heating of thick films up to 220 ºC with the 2 $^oC\times min^{-1}$ rate of temperature rise and holding for 3h and then increasing in temperature until 400 ºC with the $1^oC\times min^{-1}$ rate and holding for 3 h. In the second step, the thick-film specimens were cooled down in common with the oven.

After annealing and cooling processes, the surface of MWCNTs/SnO_2 thick films was ruthenated by dipping samples into the 0.01 M $RuOHCl_3$ aqueous solution for 20 min whereupon drying at 80 ºC for 30 min. Then, the annealing treatment was carried out again by the same method noticed above. The choice of the ruthenium as a catalyst was determined by its some advantages [17, 22, 31]. At the final stage, ruthenated MWCNT/SnO_2 chips were arranged in TO-5 packages and the gas sensors would be ready to measurements after bonding of leads.

3. Results and Discussions

Some results of the nanocomposite sensors have been presented during the international conference in Nice [33]. In this paper we introduce the extended version of our investigations. Surface morphology studies, as well as gas sensor characteristics, are shown in this section, but the performances of PG, DMF and FA sensors are separately considered. Also, the dependence of electrical resistance of the sensors on operating temperature, as well as values of responses, response and recovery times of the sensors at various operating temperatures or target gas concentrations are shown here too.

3.1. Material Characterization

The morphologies of the prepared SnO_2/MWCNT nanocomposite powders with diverse compounds were studied by scanning electron microscopy using Hitachi S-4700 Type II FE-SEM equipped with a cold field emission gun operating in the range of 5–15 kV. The presence of an oxide layer was confirmed by SEM-EDX. Furthermore, the crystalline structure of the inorganic layer was also studied by an X-ray diffraction method using the Rigaku Miniflex II diffractometer (angle range: 2θ [º]=10–80 utilizing characteristic X-ray (CuKα) radiation). Results of these investigations were presented in [17, 31] more detailed. Here, we are only noting that average crystalline size of SnO_2 nanoparticles estimated from SEM images and XRD patterns are less than 12 nm but the average diameter of non-covered by SnO_2 nanoparticles CNTs was about 40 nm.

3.2. Gas Sensing Characteristics

Gas sensing properties of the MWCNTs/SnO_2 nanocomposite structures were measured by home-made developed and computer-controlled static gas sensor test system [27]. The sensors were reheated and studied at different operating temperatures. When the electrical resistance of all studied sensors was stable, the vital assigned amount of compound in the liquid state for sensors testing was injected by a microsyringe in measurement chamber. Moreover, the target matters were introduced into the chamber on the special hot plate designed for the quick conversion of the liquid substance to its gas phase. After its resistance reached a new constant value, the test chamber was opened to recover the sensors in air. The sensing characteristics were studied in the 20-300 ºC operating temperature range and the gas response of the sensors determines as R_a/R_g, where R_a and R_g are the electrical resistances in the air and in target gas-air atmosphere, respectively. The response and recovery times are determined as the time required for reaching the 90 % resistance changes from the corresponding steady-state value of each signal.

3.3. PG Vapor Sensor Characteristics

Firstly, we should determine the operating temperature of the sensors. As a result of measurements of the sensor resistance in air and air/gas environment, the maximal response to 650 ppm PG vapor was revealed at 200 ºC operating temperature (Fig. 1 and Fig. 2).

Good repeatability of the sensor response can be seen from Fig. 3, where the electrical resistance change of PG sensor vs time measured upon cyclic exposure of 650 ppm PG vapors in air at 200 ºC operating temperature is presented.

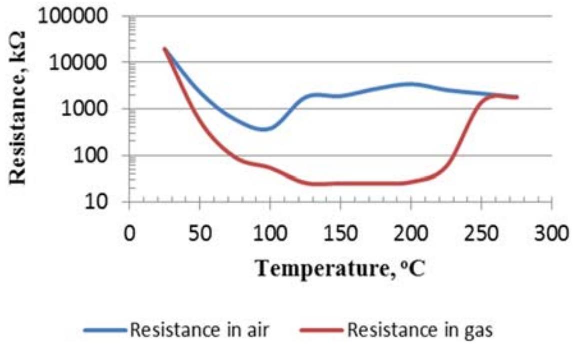

Fig. 1. Dependence of electrical resistance change of MWCNTs/SnO_2 thick-film sensors on operating temperature.

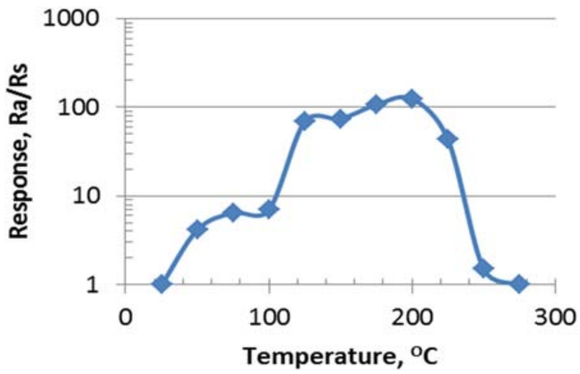

Fig. 2. Response of MWCNTs/SnO_2 thick-film PG sensors vs operating temperature.

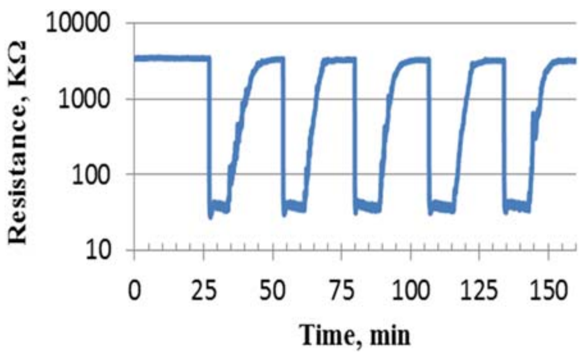

Fig. 3. The electrical resistance change of MWCNTs/SnO_2 thick-film PG sensors vs time measured upon cyclic exposure of 650 ppm PG vapors in air at 200°C operating temperature.

Changes of the response and recovery times depending on operating temperature are presented in Fig. 4 and Fig. 5.

Dependence of the resistance and response of MWCNTs/SnO_2 sensor on PG vapor concentration is shown in Fig. 6 and Fig. 7, respectively. As it is obvious from the figures, the sensor response occurs down to small target gas concentrations (13 ppm) but the response approximately linearly depends on the gas concentration.

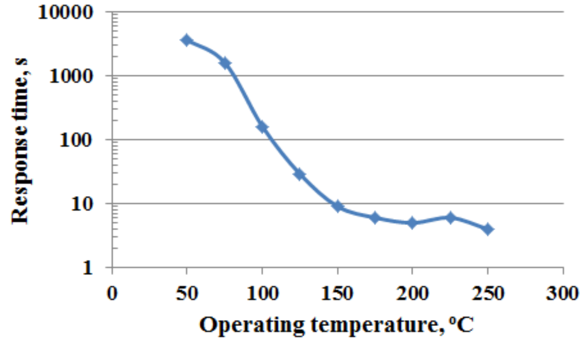

Fig. 4. Response time vs operating temperature.

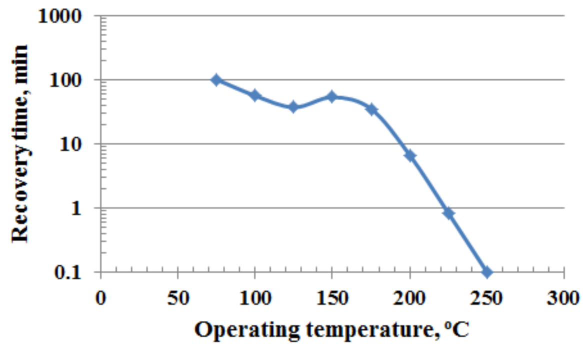

Fig. 5. Recovery time vs operating temperature.

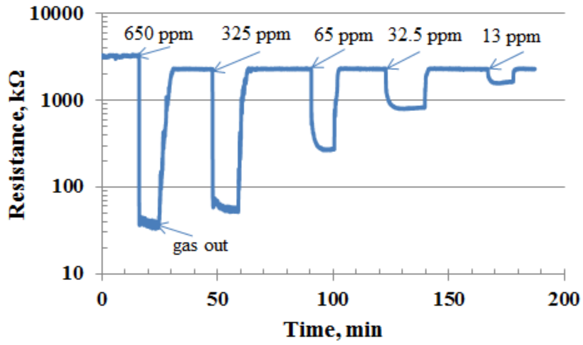

Fig. 6. The response/recovery curves observed at different PG concentrations exposure measured at 200°C operating temperature.

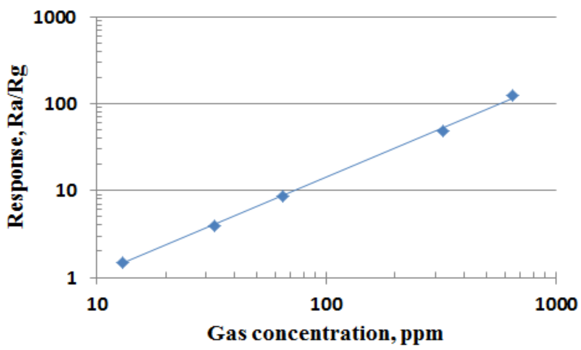

Fig. 7. Dependence of the response of MWCNTs/SnO_2 PG vapor sensor on gas concentration measured at 200°C operating temperature.

3.4. DMF Vapor Sensor Characteristics

The sensor response derived as a result of 500 ppm DMF vapor exposure versus operating temperature is presented in Fig. 8.

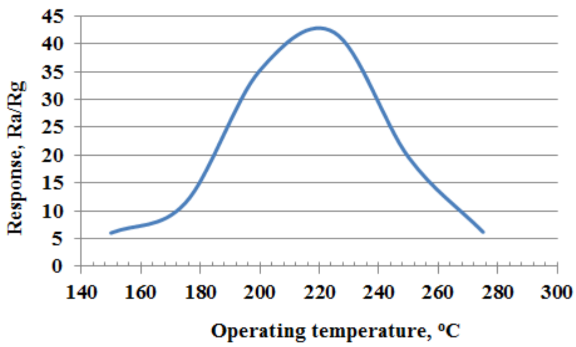

Fig. 8. Response vs operating temperature at 500 ppm DMF vapor exposure.

It can be seen that maximal response, in this case, is registered in the range of 210-225 °C. Dependence of the sensor response on versus DMF vapor concentration is also linear (Fig. 9).

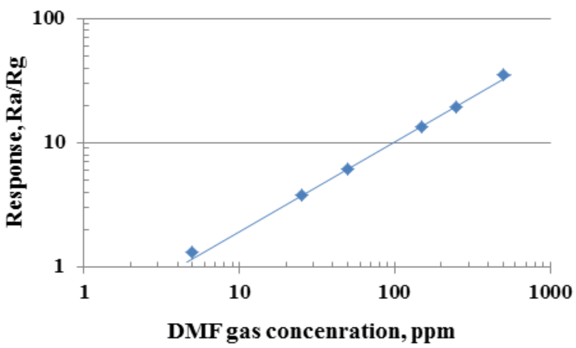

Fig. 9. Dependence of the response of MWCNTs/SnO_2 DMF vapor sensor on gas concentration measured at 200 °C operating temperature.

3.5. FA Vapor Sensor Characteristics

As a result of measurements of the sensor resistance in air and air/gas environment, the maximal response to FA vapor was revealed in the range of 200-225 °C operating temperatures (Fig. 10). Dependence of the response and recovery times of MWCNTs/SnO_2 FA vapor sensor on operating temperature is shown in Fig. 11.

Dependences of the resistance and response of MWCNTs/SnO_2 sensor on FA vapor concentration are shown in Fig. 12 and Fig. 13, respectively. As it is obvious from the figures, the sensor response increases with increasing concentration of the influencing FA gas, and this response rise occurs linearly.

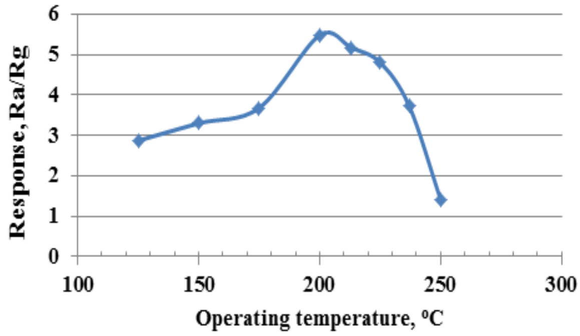

Fig. 10. Response of MWCNTs/SnO_2 thick-film FA sensors vs operating temperature.

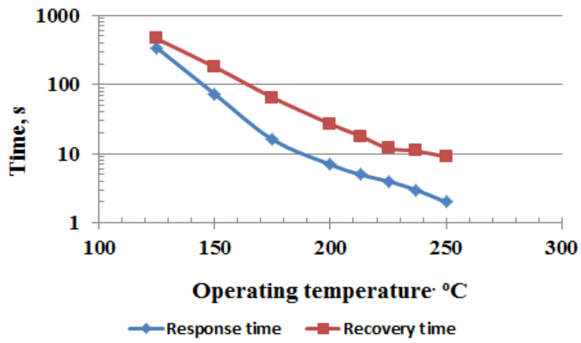

Fig. 11. Dependence of the response and recovery times of MWCNTs/SnO_2 FA vapor sensor on operating temperature.

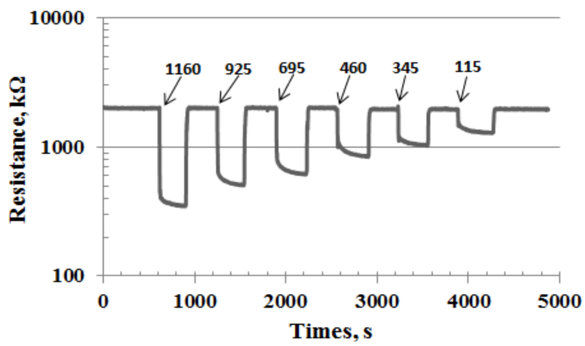

Fig. 12. The response/recovery curves observed at different FA gas concentrations exposure measured at 200 °C operating temperature.

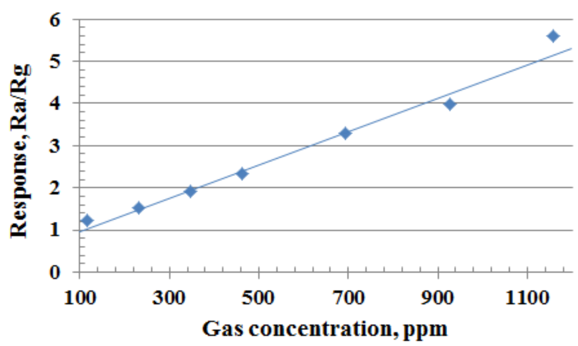

Fig. 13. Dependence of the response of MWCNTs/SnO_2 FA vapor sensor on gas concentration measured at 200 °C operating temperature.

3.6. Comparison

Comparison of responses of MWCNTs/SnO_2 sensors to 650 ppm PG, 500 ppm DMF and 1160 ppm FA vapors exposure vs operating temperature is shown in Fig. 14.

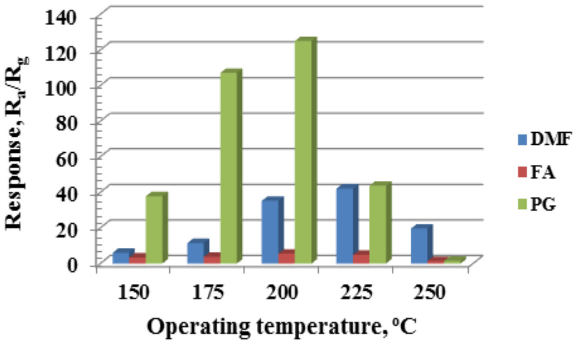

Fig. 14. Comparison of responses of MWCNTs/SnO_2 sensors to 650 ppm PG, 500 ppm DMF and 1160 ppm FA vapors exposure at various operating temperatures.

As it is shown from the Fig. 14, Sensors demonstrate the best response against PG and FA vapors at 200 °C operating temperature and against DMF vapor at 225 °C operating temperature.

3.7. On Possible Mechanism of Gas Sensitivity

It is known that the attachment of carboxyl groups on the surface of MWCNTs is effective in nucleation and trapping the other materials including tin oxide nanoparticles. As it was shown earlier, COOH groups attached on the surface of MWCNTs have a strong interaction with alcohol vapors resulting hydrogen bond between COOH groups and the OH groups of alcohol molecules [17-22]. This hydrogen bond should be removed by increasing the temperature, which contributes to long recovery times in MWCNTs/SnO_2 sensors.

The increase in response with an increase in the operating temperature of the sensor is observed until the maximum value is reached. With the subsequent increase in operating temperature, desorption of chemisorbed oxygen ions takes place and gas response decreases; the recovery time decreases, too.

MWCNTs nanochannels play a smaller role at relatively more content of SnO_2 in the nanocomposite (as in our case), as nanotubes are closed by plenty of SnO_2 nanoparticles. Due to it, accessibility of gas molecules penetration to MWCNTs nanochannels through the metal-oxide thick film is very difficult. Therefore, the gas response is mainly determined by a number of metal-oxide nanoparticles and a considerable amount of surface adsorption sites. MWCNTs only prevent the formation of agglomerates of SnO_2 and ensure the development of the surface because of repulsive forces between the carboxyl groups adsorbed on it.

The oxidation reaction of PG and DMF vapors on the nanocomposite surface could be represented as follows, respectively:

$$C_3H_8O_2(g) + 8O^- \rightarrow 3CO_2(g) + 4H_2O(g) + 8e^-$$

and

$$4C_3H_7NO(g) + 42O^- \rightarrow 12CO_2(g) + 4NO_2(g) + 14H_2O(g) + 42e^-$$

At the temperature corresponding to the highest response, the reactivity of the target gas molecules is proportional to the speed of diffusion into the sensing layer. Hence, the target gas has the chance to sufficiently penetrate into the sensing layer and react with an appropriate speed. The competition between the amount of adsorbed target gases and their oxidation rate supports the maximum response and its sharp decline. With the following increase in operating temperature, desorption of the adsorbed oxygen ions from the surface of the sensor is increased. It follows that less amount of oxygen ions presents on the surface of SnO_2, might take part in reaction with target gases at higher operating temperature. Therefore, the response falls at high operating temperatures. Furthermore, it influences the physical properties of the semiconducting sensor material. For instance, at higher temperatures the carrier concentration increases (resulting from the release of electrons back to the conduction band in consequence of desorption of adsorbed oxygen) and the Debye length decreases. This may also be one of the possible reasons for the rise in Rg curve in Fig. 1, which leads to the decrease in response at higher temperatures. Although molecular weights of both considered target gases are close to each other, the quantity of carbon atoms is the same. Nevertheless, the response from DMF vapors influences less due to many adsorbed oxygen ions, resulted from the chemical decomposition, which demands for the full oxidation reaction. Thus, the 1:200 weight ratios of the nanocomposite sensor components with relatively large amount of SnO_2 particles promote an initiation of a sufficiently large quantity of ionized adsorption centers, which ensure relatively high response to DMF gas exposure.

FA gas sensing mechanism is not fully researched so far. It is proposed that the HCHO sensing process can be described by the commonly accepted gas sensing mechanism for n-type semiconducting metal oxides including SnO_2. Namely, as a result of adsorption-oxidation and desorption processes sensor surface is covered by chemisorbed oxygen ions, such as O^- and O^{2-}. When sensor exposed with FA gas HCHO molecules interact with the adsorbed oxygen according to the following reactions.

$$HCHO + 2O^- \rightarrow H_2O + CO_2 + 2e^-$$

$$HCHO + 2O^{2-} \rightarrow H_2O + CO_2 + 4e^-$$

These reactions lead to enhance the free electron concentration which causes the decrease of the resistance of SnO_2.

As for selectivity, this nanocomposite sensor demonstrates cross-sensitivity to some alcohols, such as butanol, methanol and ethanol at 200 °C operating temperature [21, 31]. Unlike existing other type PG, DMF and FA sensors, presented nanocomposite sensor is able to measure the concentration of mentioned gases in the atmosphere.

4. Conclusions

In this paper, we have carried out the investigation of obtaining ruthenated MWCNTs/SnO_2 thick-film nanocomposite sensors using hydrothermal synthesis and sol-gel technologies. It is revealed that studied sensors give a sufficiently high response to such harmful and hazardous gases as PG, DMF and FA at relatively low operating temperatures. The fast response of the sensors (at the order of seconds) and acceptable recovery times are observed under all gas concentrations influence at 200 °C operating temperature. The minimal PG, DMF and FA gas concentrations at which the perceptible signal is registered are 13 ppm, 5 ppm and 115 ppm, respectively.

Due to the linear dependence of the response on the concentration of PG, DMF and FA vapors, it is possible to easily measure the concentration of mentioned gases in the atmosphere.

Acknowledgements

This work was supported by NATO EAP SFPP 984.597.

References

[1]. A. Fiorito, F. Larese, S. Molinari, T. Zanin, Liver function alterations in synthetic leather workers exposed to dimethylformamide, *American Journal of Industrial Medicine*, Vol. 32, No. 3, 1997, pp. 255-260.

[2]. M. A. Lefebvre, W. J. Meulingb, R. Engel, M. C. Coroamac, G. Rennerc, W. Pape, G. J. Nohynek, Consumer inhalation exposure to formaldehyde from the use of personal care products/cosmetics, *Regulatory Toxicology and Pharmacology*, Vol. 63, Issue 1, 2012, pp. 171-176.

[3]. G. Malaguarnera, E. Cataudella, M. Giordano, G. Nunnari, G. Chisari, M. Malaguarnera, Toxic hepatitis in occupational exposure to solvents, *World Journal of Gastroenterology*, 2012, Vol. 18, Issue 22, pp. 2756-2766.

[4]. H. Y. Chang, T. S. Shih, Y. L. Guo, C. Y. Tsai, P. C. Hsu, Sperm function in workers exposed to N,N-dimethylformamide in the synthetic leather industry, *Fertil Steril*, Vol. 81, Issue 6, 2004, pp. 1589-1594.

[5]. V. M. Aroutiounian, in Advanced Sensors for Safety and Security, A. Vaseashta, S. Khudaverdyan (eds.), *NATO Science for Peace and Security, Series B: Physics and Biophysics,* Chapter 9, 2012.

[6]. G. F. Fine, L. M. Cavanagh, A. Afonja, R. Binions, Metal oxide semi-conductor gas sensors in environmental monitoring, *Sensors*, Vol. 10, Issue 6, 2010, pp. 5469-5502.

[7]. G. Korotcenkov, S. H. Han, B. K. Cho, Material design for metal oxide chemiresistive gas sensors, *Journal of Sensor Science and Technology*, Vol. 22, No. 1, 2013, pp. 1-17.

[8]. W. Y. Chuang, S. Y. Yang, W. J. Wu, C. T. Lin, A Room-Temperature Operation Formaldehyde Sensing Material Printed Using Blends of Reduced Graphene Oxide and Poly(methyl methacrylate), *Sensors*, Vol. 15, No. 11, 2015, pp. 28842-28853.

[9]. J. Flueckiger, F. K. Ko, K. C. Cheung, Microfabricated Formaldehyde Gas Sensors, *Sensors*, Vol. 9, No. 11, 2009, pp. 9196-9215.

[10]. K. Xu, D. Zeng, S. Tian, S. Zhang, C. Xie, Hierarchical porous SnO_2 micro-rods topologically transferred from tin oxalate for fast response sensors to trace formaldehyde, *Sensors and Actuators B: Chemical,* Vol. 190, 2014, pp. 585-592.

[11]. H. J. Park, N. J. Choi, H. Kang, M. Y. Jung, J. W. Park, K. H. Park, D. S. Lee, A ppb-level formaldehyde gas sensor based on CuO nanocubes prepared using a polyol process, *Sensors and Actuators B: Chemical*, Vol. 203, 2014, pp. 282–288.

[12]. F. C. Chung, R. J. Wu, F. C. Cheng, Fabrication of an Au@SnO_2 core–shell structure for gaseous formaldehyde sensing at room temperature, *Sensors and Actuators B: Chemical*, Vol. 190, 2014, pp. 1-7.

[13]. X. Li, X. Li, J. Wang, S. Lin, Highly sensitive and selective room-temperature formaldehyde sensors using hollow TiO_2 microspheres, *Sensors and Actuators B: Chemical*, Vol. 219, 2015, pp. 158-163.

[14]. V. M. Aroutiounian, Gas sensors based on functionalized carbon nanotubes, *Journal of Contemporary Physics (Armenian Academy of Sciences)*, Vol. 50, No. 4, 2015, pp. 333-354. *Izvestiya NAN Armenii, Fizika*, Vol. 50, No. 4, 2015, pp. 448-475.

[15]. M. M. Arafat, B. Dinan, S. A. Akbar, A. S. M. A. Haseeb, Gas sensors based on one dimensional nanostructured metal-oxides: A Review, *Sensors*, Vol. 12, No. 6, 2012, pp. 7207-7258.

[16]. G. Korotcenkov, S. D. Han, B. K. Cho, V. Brinzari, Grain size effects in sensor response of nanostructured SnO_2 and In_2O_3-based conductometric thin film gas sensor, *Critical Reviews in Solid State and Materials Sciences,* Vol. 34, Issue 1-2, 2009, pp. 1-17.

[17]. V. M. Aroutiounian, A. Z. Adamyan, E. A. Khachaturyan, Z. N. Adamyan, K. Hernadi, Z. Pallai, Z. Nemeth, L. Forro, A. Magrez, E. Horvath, Study of the surface-ruthenated SnO_2/MWCNTs nanocomposite thick-film gas sensors, *Sensors and Actuators B: Chemical,* Vol. 177, 2013, pp. 308-315.

[18]. S. A. Feyzabad, A. A. Khodadadia, M. V. Naseh, Y. Mortazavi, Highly sensitive and selective sensors to volatile organic compounds using MWCNTs/SnO_2, *Sensors and Actuators B: Chemical,* Vol. 166–167, 2012, pp. 150-155.

[19]. N. V. Hieu, L. T. B. Thuy, N. D. Chien, Highly sensitive thin film NH_3 gas sensor operating at room temperature based on SnO_2/MWCNTs composite, *Sensors and Actuators B: Chemical*, Vol. 129, 2008, pp. 888-895.

[20]. X. Bai, H. Ji, P. Gao, Y. Zhang, X. Sun, Morphology, phase structure and acetone sensitive properties of

copper-doped tungsten oxide sensors, *Sensors and` Actuators B: Chemical*, Vol. 193, 2014, pp. 100-106.

[21]. V. M. Aroutiounian, Z. N. Adamyan, A. G. Sayunts, E. A. Khachaturyan, A. Z. Adamyan, Study of MWCNT/SnO_2 nanocomposite acetone and toluene vapor sensors, in *Proceedings of the 17th International Conference on Sensors and Measurement Technology (SENSOR'15)*, Nierenberg, Germany, 19-21 May 2015, pp. 836-841.

[22]. Z. N. Adamyan, A. G. Sayunts, E. A. Khachaturyan, V. M. Aroutiounian, Study of nanocomposite thick-film butanol vapor sensors, *Journal of Contemporary Physics (Armenian Academy of Sciences),* Vol. 51, Issue 2, 2016, pp. 143-149.

[23]. V. M. Aroutiounian, Metal oxide hydrogen, oxygen and carbon monoxide sensors for hydrogen setups and cells, *International Journal of Hydrogen Energy,* Vol. 32, Issue 9, 2007, pp. 1145-1158.

[24]. P. Shankar, J. Bosco, B. Rayappan, Gas sensing mechanism of metal oxides: The role of ambient atmosphere, type of semiconductor and gases - A review, *Science Letters*, Vol. 4/126, 2015, pp. 1-18.

[25]. C. Xu, J. Tamaki, N. Miura, N. Yamazoe, Grain size effects on gas sensitivity of porous SnO_2-based elements, *Sensors and Actuators B: Chemical*, Vol. 3, No. 2, 1991, pp. 147-155.

[26]. A. Z. Adamyan, Z. N. Adamyan, V. M. Aroutiounian, Preparation of SnO_2 films with thermally stable nanoparticles, *Sensors,* Vol. 3, 2003, pp. 438-442.

[27]. A. Z. Adamyan, Z. N. Adamyan, V. M. Aroutiounian, A. H. Arakelyan, J. Turner, K. Touryan, Sol–gel derived thin-film semiconductor hydrogen gas sensor, *International Journal of Hydrogen Energy*, Vol. 32, No. 16, 2007, pp. 4101-4108.

[28]. E. Couteau, K. Hernadi, J. W. Seo, L. Thien-Nga, Cs. Mikó, R. Gáal, L. Forró, CVD synthesis of high-purity multiwalled carbon nanotubes using $CaCO_3$ catalyst support for large-scale production, *Chemical Physics Letters*, Vol. 378, No. 1-2, 2003, pp. 9-17.

[29]. A. Magrez, J. W. Seo, R. Smajda, M. Mionić, L. Forró, Catalytic CVD Synthesis of Carbon Nanotubes: Towards High Yield and Low Temperature Growth, *Materials* Vol. 3, No. 11, 2010, pp. 4871-4891.

[30]. Z. Nemeth, B. Reti, Z. Pallai, P. Berki, J. Major, E. Horvath, A. Magrez, L. Forro, K. Hernadi, Chemical challenges during the synthesis of MWCNT-based inorganic nanocomposite materials, *Physica Status Solidi (B) Basic Research*, Vol. 251, Issue 12, 2014, pp. 2360-2365.

[31]. V. M. Aroutiounian, Z. N. Adamyan, A. G. Sayunts, E. A. Khachaturyan, A. Z. Adamyan, K. Hernadi, Z. Nemeth, P. Berki, Comparative study of VOC sensors based on ruthenated MWCNT/SnO_2 nanocomposites, *International Journal of Emerging Trends in Science and Technology (IJETST)*, Vol. 01, Issue 08, 2014, pp. 1309-1319.

[32]. Z. Nemeth, Z. Pallai, B. Reti, Z. Balogh, O. Berkesi, K. Baan, A. Erdohelyi, E. Horvath, G. Veréb, A. Dombi, L. Forró, K. Hernadi, Synthesis, Comparative Characterization and Photocatalytic Application of SnO_2/MWCNT Nanocomposite Materials, *Journal of Coating Science and Technology*, Vol. 1, No. 2, 2014, pp. 137-150.

[33]. Z. Adamyan, A. Sayunts, V. Aroutiounian, E. Khachaturyan, A. Adamyan, M. Vrnata, P. Fitl, J. Vlček, Study of Propylene Glycol and Dimethylformamide Vapors Sensors Based on MWCNTs/SnO_2 Nanocomposites, in *Proceedings of the Second International Conference on Advances in Sensors, Actuators, Metering and Sensing (ALLSENSORS 2017)*, Nice, France, 19-23 March 2017, pp. 44-49.

IFSA
www.sensorsportal.com

Sensors & Transducers
Published by IFSA Publishing, S. L., 2017
http://www.sensorsportal.com

Nanostructured Sensors for Detection of Hydrogen Peroxide Vapours

[1] Vladimir AROUTIOUNIAN, [1] Valeri ARAKELYAN, [1] Mikayel ALEKSANYAN, [1] Artak SAYUNTS, [1] Gohar SHAHNAZARYAN, [2] Petr KACER, [2] Pavel PICHA, [2] Jiri KOVARIK, [2] Jakub PEKAREK and [3] Berndt JOOST

[1] Department of Physics of Semiconductors and Microelectronics, Yerevan State University, 1 A. Manoogian St., Yerevan, 0025, Republic of Armenia
[2] University of Chemistry and Technology, Technická 5, 166 28 Prague 6, Czech Republic
[3] Institute for Pharmaceutical Technology, Fachhochschule Nordwestschweiz, Hochschulefür Life Sciences, Gründenstrasse 40, CH-4132 Muttenz, Switzerland
[1] Tel.: 374 60 710315, fax: 374 60 710355
[1] E-mail: kisahar@ysu.am

Received: 18 May 2017 /Accepted: 20 June 2017 /Published: 30 June 2017

Abstract: Solid-state sensors made from doped metal oxide ZnO<La> and SnO_2<Co> were prepared for detection of hydrogen peroxide vapours. Gas sensitive nanostructured films were manufactured by the high-frequency magnetron sputtering method. Thicknesses of deposited semiconductor nanostructured films were measured and its morphology was investigated. The average size of nanoparticles was equal to 18.7 nm for deposited films. The response of the prepared sensors was measured at different temperatures of the sensor work body and different concentrations of hydrogen peroxide vapours. It was found that both La-doped ZnO and Co-doped SnO_2 sensors exhibit a sufficient sensitivity to 10 ppm of hydrogen peroxide vapours at the operating temperature 220 °C and 200 °C, respectively. It was established that the dependencies of the sensor sensitivity on hydrogen peroxide vapours concentration at the work body temperature 150 °C have a linear characteristic for both prepared structures and can be used for determination of hydrogen peroxide vapours concentration.

Keywords: Sensor, Hydrogen peroxide vapours, Semiconductor, Nanostructured film, Doped metal oxide.

1. Introduction

Hydrogen peroxide (H_2O_2) is a chemical widely used in such fields as medicine, pharmacology, food and textile industry due to a wide spectrum of its antibacterial properties, low toxicity and ecological purity (it decomposes to produce neutral water and oxygen). However, pure H_2O_2 at large concentrations is explosive under certain conditions (for example, in the presence of transition metals). Therefore, concentrated solutions of H_2O_2 can cause burns in the case of the contact with skin, mucous membranes and respiratory tract. H_2O_2 is subsumed under the category of matters those are dangerous for man with certain maximum permissible concentration. Therefore, the development of sensors for determination of the H_2O_2 concentration in the environment is important and attracts interest of chemists, physicians, industrial engineers, etc. The H_2O_2 stable sensors can be used in analytical chemistry, in various fields of the industry (food, wood pulp textile, pharmacology), for the environmental control, in clinical diagnostic for prompt and reliable specification of diagnoses of different diseases and checking of a course of treatment.

Several techniques have been developed for a reliable and sensitive determination of H_2O_2, such as chemiluminescence, spectrophotometry, fluorimetric and colorimetric detection, liquid chromatography, electroanalytical and optical interferometry [1-5]. These techniques are complex, expensive and time consuming. Now the electrochemical sensors are used [4-9]. A large range of materials such as ferric hexacyanoferrate (Prussian blue) and other metal hexacyanoferrates, metallophthalocyanines and metalloporphyrins, transition metals and metal oxides have been employed for the manufacture of these sensors. The advantages of these sensors are simplicity of manufacturing, good response and capability of control in a real time. In recent years, nanotechnology progress is promoted advance in the field of manufacturing of the H_2O_2 electrochemical sensors. For example, carbon nanotubes and graphene can be used either as substrates with high specific area for catalytic materials or as electrocatalysts by themselves [10-13].

H_2O_2 serves as a disinfectant for medical equipment and surfaces as well as for sterilizing surgical instruments. Therefore, the correct selection of the H_2O_2 concentration during the sterilization of the equipment technological surfaces and also control of the H_2O_2 content in air after completion of disinfection cycle are very important. Note that the process of chemical decontamination can be carried out in two different ways: the first one is the wet approach using water or any other solutions of H_2O_2 (certain concentration) and the second one is the dry method using H_2O_2 in vapour phase [14]. Therefore, the development and manufacturing of stable and reproducible sensors sensitive to H_2O_2 vapours are extremely required [15-17]. The checking of H_2O_2 vapours phase is also crucially significant in connection with counterterrorism efforts. The sensors sensitive to H_2O_2 vapours may find application in the detection of peroxide-based explosives [18, 19].

The most used method is based on the determination of the concentration of H_2O_2 vapours after cooling down and being absorbed in the water. The near infrared spectrophotometry was used for the monitoring of the concentration of H_2O_2 vapours in the course of sterilization [20]. The chemiresistive films made from organic p-type semiconducting phthalocyanines metalized with elements of p-, d-, and f-blocks were sensitive to H_2O_2vapours [18]. An amperometric sensor for detection of H_2O_2 vapours made of an agarose-coated Prussian-blue modified thick-film screen-printed carbon-electrode transducer was investigated [21]. It was reported about organic single-wire optical sensor for H_2O_2 vapours made of organic core/sheath nanowires with wave guiding core and chemiluminogenic cladding [22].

The aim of the present paper is development of technology, manufacture and investigation of solid-state H_2O_2 vapours sensors made from semiconductor metal oxide nanostructured films.

Here, the necessities in the development of the H_2O_2 sensors and, in particular, sensors sensitive to H_2O_2 vapours are briefly described. The manufacturing technology of sensors made from semiconductor doped with metal oxide ZnO<La> and SnO_2<Co> nanostructures is given in the second section. The results of the investigations of prepared sensors sensitivity to H_2O_2 vapours are presented in the third section. In the fourth section, the conclusions are made and the directions of the future work are described.

2. Experiments

Ceramic targets made from metal oxide ZnO doped with 1 at.% La or SnO_2 doped with 2 at.% Co were synthesized by the method of solid-phase reaction in the air into the programmable furnace Nabertherm, HT O4/16 with the controller C 42. The following program of annealing for the compact samples of ZnO<La> was chosen: rise of temperature from room temperature up to 1300 °C for three hours, soaking at this temperature during four hours, further decrease in the temperature for three hours prior to room temperature. The annealing of the compacted samples SnO_2<Co> was carried out at 500 °C, 700 °C, 1000 °C and 1100 °C consecutively, soaking at each temperature during five hours. Then, the synthesized compositions were subjected to mechanical treatment in the air in order to eliminate surface defects. Thus, smooth, parallel targets with a diameter ~ 40 mm and thickness ~2 mm were manufactured.

The prepared ZnO<La> and SnO_2<Co> targets had sufficient conductance and were used for deposition of nanosize films. Multi-Sensor-Platforms (purchased from TESLA BLATNÁ, Czech Republic) are used as substrates. Chips can be kept at constant temperature using heat resistance. The platform integrates a temperature sensor (Pt 1000), a heater and interdigitated electrode structures with platinum thin film on a ceramic substrate. Heater and the temperature sensor are covered with an insulating glass layer. Gas sensitive layer made from ZnO doped with 1 at.% La or SnO_2 doped with 2 at.% Co was deposited onto the non-passivated electrode structures using the high-frequency magnetron sputtering method. The Multi-Sensor-Platforms are converted into gas sensors that way.

The following working conditions of the high-frequency magnetron sputtering were chosen: the power of the magnetron generator unit was equal to 60 W; the substrate temperature during sputtering was equal to 200 °C; the distance between substrate and target was equal to 7 cm; the duration of the sputtering process was equal to 15 minutes and 20 minutes for ZnO<La> and SnO_2<Co>, respectively. The sensing device was completed through the ion-beam sputtering deposition of palladium catalytic particles (the deposition time ~ 3 seconds). Further annealing of the manufactured structures in the air was carried out at temperature 250 °C to obtain homogeneous films and eliminate mechanical stresses.

The thicknesses of the deposited doped metal oxide films were measured by Ambios XP-1 profilometer. The morphology and chemical composition of the deposited SnO_2<Co> and ZnO<La> films were studied by scanning electron microscopy (SEM) using Mira 3 LMH (Tescan) and energy-dispersive X-ray spectroscopy using Quantax 200 with XFlash 6|10 detector (Bruker) with resolution of 127 eV, respectively.

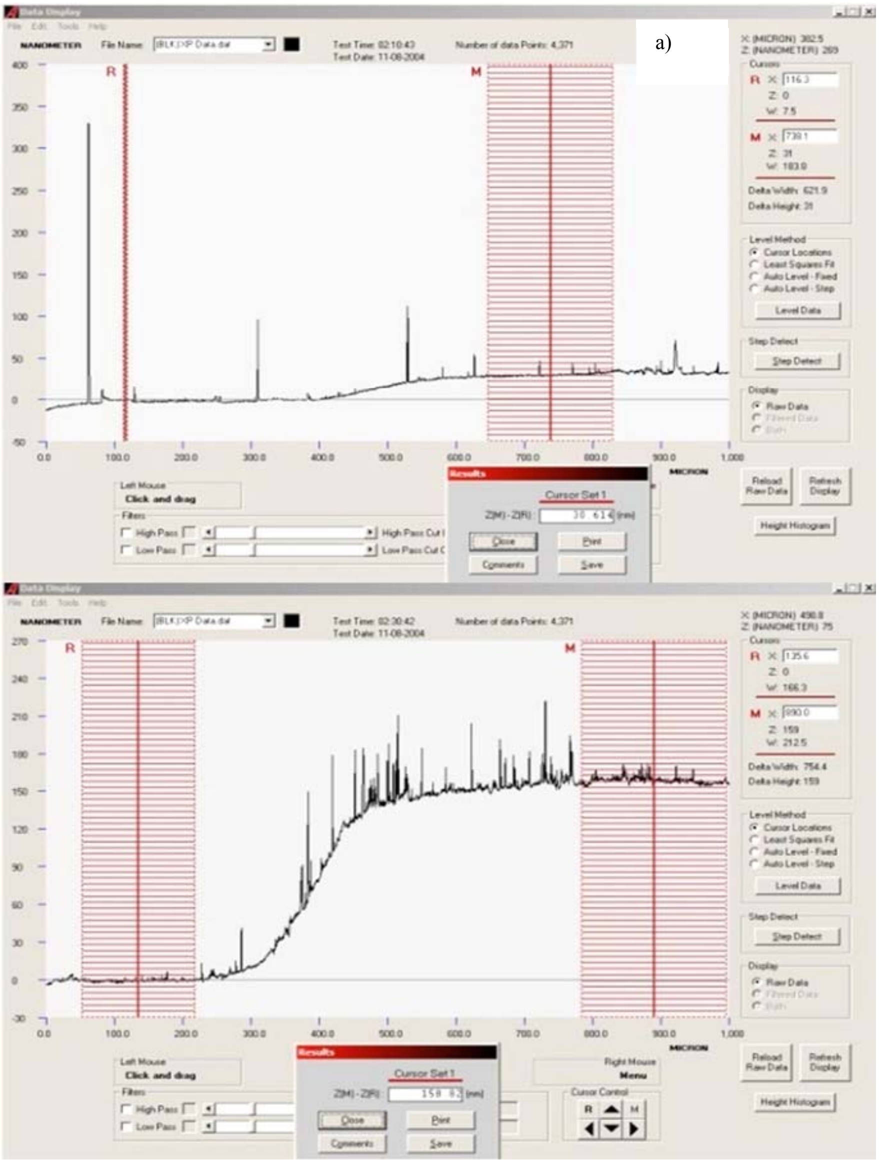

Fig. 1. The thicknesses measurements resultes for ZnO<La> (a) and SnO_2<Co> (b) films.

The gas sensing properties of the prepared sensors made from doped metal oxide films under the influence of H_2O_2 vapours were measured at Yerevan State University using a home-made developed system (see, for example, [23]). The sensors were placed in a hermetic chamber. A certain quantity of H_2O_2 water solution was placed in the chamber to reach a corresponding concentration of H_2O_2 vapours. The measurements of the manufactured sensors response (the sensor resistance changes under the H_2O_2 vapours influence) were carried out at different concentrations of H_2O_2 vapours (from 100 ppm up to 4000 ppm). The platinum heater on a front side of the sensor ensures a necessary temperature of the work body. The sensor work body temperature was varied from room temperature up to 350 °C. All measurements were carried out at the sensor applied voltage of 0.5 V. As a result of such measurements, the sensor sensitivity was determined as the ratio $R_{peroxide}/R_{air}$, where $R_{peroxide}$ is the sensor resistance in the presence of H_2O_2 vapours in the air and R_{air} is the sensor resistance in the air without H_2O_2 vapours.

The investigations of the sensitivity of the prepared sensors to H_2O_2 vapours with concentration lower than 100 ppm were carried out at University of Chemistry and Technology (Prague). In particular, the measurements of the response of the ZnO<La> sensors to 10 ppm H_2O_2 vapours were carried out by the following way. Firstly, an atmosphere containing 10 ppm of H_2O_2 vapours was prepared in a laboratory model of an isolator. This H_2O_2 vapours concentration decreased by spontaneous decomposition of H_2O_2. When a reference device (Dräger Sensor® H_2O_2 HC) could not detect any H_2O_2 vapours, the ZnO<La> sensor was inserted into the model isolator. Then, sensor responded immediately. When the maximum response was reached, the sensor was taken out into an atmosphere without any traces of H_2O_2 vapours. This process was repeated three times. The measurements of the response to 75 ppm H_2O_2 vapours were carried out for the SnO_2<Co> sensors in the same way.

The temperature dependence of sensitivity to 10 ppm H_2O_2 vapours were investigated for the SnO_2<Co> sensors. For these measurements, atmosphere in "Peroxybox" system, developed in the same Institute in Prague, was controlled (0-10 ppm H_2O_2 and 20-23% RH) and the sensor's temperature was changed. The final sensitivity was calculated as the response of sensor in "Peroxybox" system divided by the response of sensor in the air.

The temperature dependence of sensitivity to 100 ppm H_2O_2 vapours were investigated in the same way for the ZnO<La> sensors.

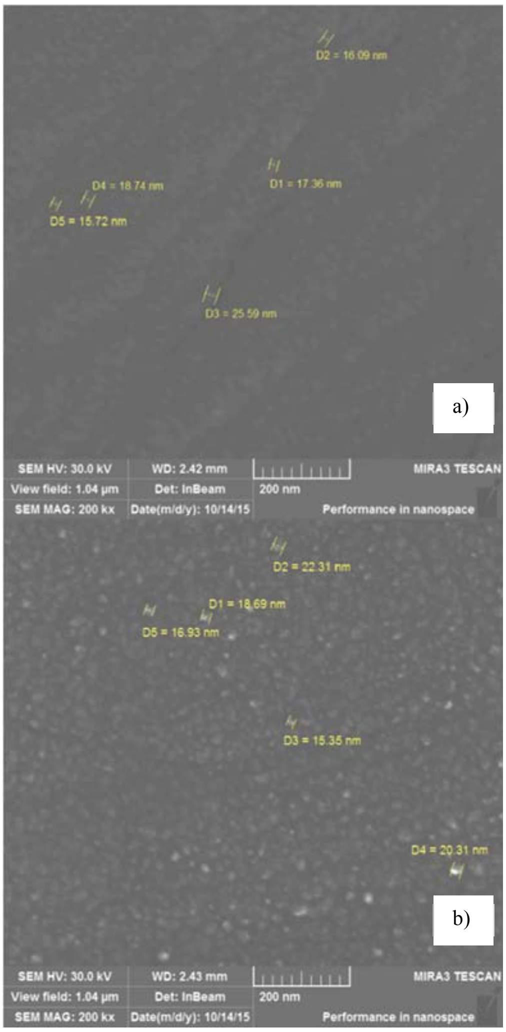

Fig. 2. The SEM images for SnO_2 doped with 2 at.% Co (a) and ZnO doped with 1 at.% La (b) films.

3. Results and Discussion

The thicknesses of the ZnO doped with 1 at.% La and SnO_2 doped with 2 at.% Co films were equal to 30 nm and 160 nm, respectively (Fig. 1).

The results of the study of morphology for the deposited doped metal oxide films are presented in Fig. 2. The average size of nanoparticles was equal to 18.7 nm for both compositions.

The sensors manufactured by us are resistive. The operation of this type of sensors grounds on the changes in the electrical resistance of gas sensitive semiconductor layer under the influence of H_2O_2 vapours due to an exchange of charges between molecules of the semiconductor film and adsorbed H_2O_2 vapours.

The H_2O_2 decomposes to produce water vapours and oxygen:

$$2H_2O_2 \rightarrow 2H_2O\uparrow + O_2\uparrow\ . \quad (1)$$

These adsorbed oxygen molecules capture the electrons from the semiconductor film:

$$O2 + e- \rightarrow O2-\ . \quad (2)$$

A variation of the sensor resistance takes place as a result of such exchange byelectrons. This variation of the resistance was fixed as a sensor response.

The sensor resistance variation under the H_2O_2 vapours influence was measured at Yerevan State University using the static gas sensor test program controlled a special home-made computer system. Typical curve demonstrating the change in the sensor resistance under the influence of H_2O_2 vapours at invariable temperature of the work body is presented in Fig. 3a. As mentioned above, the sensitivity of sensors was calculated as the ratio $R_{peroxide}/R_{air}$, where $R_{peroxide}$ and R_{air} are the sensor electrical resistances in the H_2O_2 vapours atmosphere and in the air, respectively. The ZnO<La> sensor sensitivity at different work body temperatures is presented in Fig. 3b.The response and recovery times were determined as the time required for reaching the 90% resistance changes from the corresponding steady-state value of each signal. For the ZnO<La> sensors the response and recovery times were equal to 6-8 and 10-12 minutes in average, respectively, at the temperatures more than 200 °C.

The results of such investigations for SnO_2<Co> sensors are presented in Fig. 4. For this structure both the response and recovery times were equal to 5 minutes at the temperatures more than 200 °C.

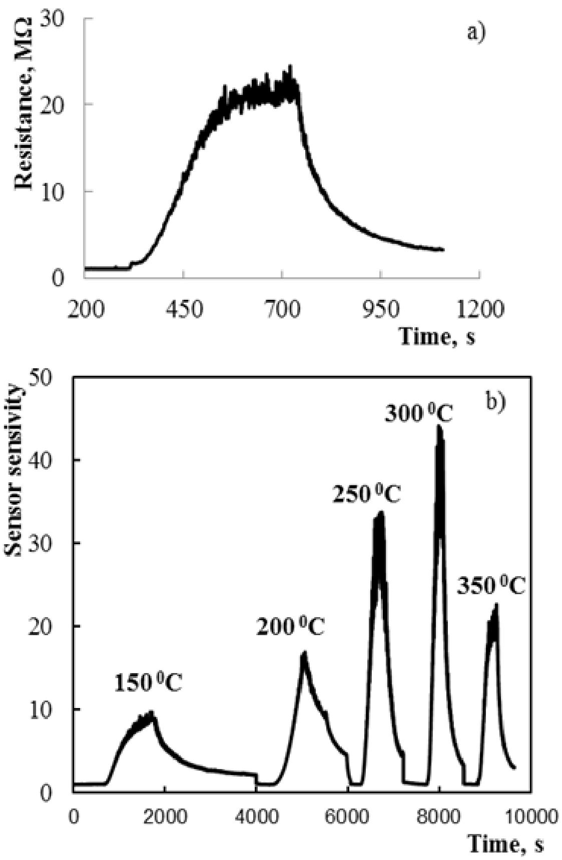

Fig. 3. a)The resistance change of the ZnO<La> sensor under the influence 1800 ppm of H_2O_2 vapours, work body temperature 350 °C;
b) The sensitivity to 1800 ppm of H_2O_2 vapours for ZnO<La> sensor at different work body temperatures.

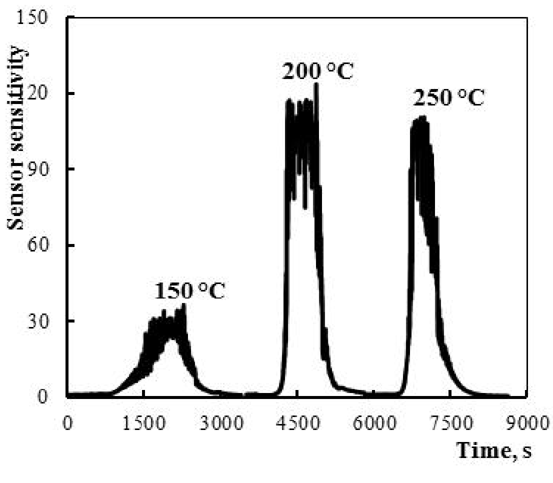

Fig. 4. The sensitivity to 100 ppm of H_2O_2 vapours for SnO_2<Co> sensor at different work body temperatures.

As shown in Fig. 3b and Fig. 4, the sensitivity of the sensors decreases for both structures, when the working body temperature excesses some certain value (300 °C and 250 °C for ZnO<La> and SnO_2<Co> sensors, respectively). The amount of vapour molecules adsorbed on a surface and generally held by Van der Waals forces (physical adsorption), decreases with the increasing of temperature. More intensive exchange of electrons between the absorber and the absorbed molecules takes place when the stronger chemical nature bond is established between its, originated at capping of electronic shells of both adsorbent and adsorbate atoms. The amount of chemisorbed centers increases with increasing the temperature. The desorption prevails over the adsorption when a temperature is increased above certain value and, therefore, the sensor sensitivity decreases. The temperature, above which the sensitivity decreasing occurs, for the sensors made of ZnO<La> structure is greater than for the sensors made of SnO_2<Co>structure. Probably, the chemical bonds between molecules of ZnO and H_2O_2 are stronger than that of between molecules of SnO_2 and H_2O_2. This is also testified by the fact that the recovery time for sensors made of SnO_2<Co> is less than that of for ZnO<La> sensors.

Note, the prepared sensors resistance has changed in order of magnitude under influence of H_2O_2vapours starting at operation temperature of 100 °C. However, a longer time was needed for recovery of the sensors parameters at such temperature. The pulsed increasing in the work body temperature is needed for decreasing of the recovery time of the investigated sensors.

As it has already been noticed, the H_2O_2 belongs to the type of materials dangerous for man with certain maximum permissible concentration. The permissible limit of exposure of 1,0 ppm has established by Occupational Safety and Health Administration (OSHA, USA) [16, 20]. It is immediately dangerous for life and health when its concentration reaches 75 ppm [3]. Therefore, the investigations of the prepared SnO_2<Co> and ZnO<La> sensors gas sensing properties to H_2O_2 vapours with concentration lower than 100 ppm were also carried out at University of Chemistry and Technology (Prague).

The results of these investigations are presented in Fig. 5 and Fig. 6. The investigations of the sensors sensitivity to very low concentrations (0-10 ppm) of H_2O_2 vapours show, that the structure made of SnO_2<Co> exhibits a response to 10 ppm of H_2O_2 vapours at the operating temperature starting at 50 °C (Fig. 6b). The sensitivity to 10 ppm of H_2O_2vapours was equal to ~ 3 for the SnO_2<Co> sensors at the work body temperature of 200 °C. The sensitivity to 10 ppm of H_2O_2 vapours was equal to ~ 2 for the ZnO<La> sensors at the work body temperature of 220 °C. Note that the DrägerSensor® H_2O_2 HC reference device is not sensitive to 10 ppm of H_2O_2vapours (Fig. 5a). These measurements were carried out at University of Chemistry and Technology (Prague).

The results of investigations of the prepared sensors sensitivity at different concentrations of H_2O_2 vapours are presented in Fig. 7.

As can see, these dependencies sensitivity on H_2O_2vapours concentration have a linear characteristic for both type of sensors and can be used for determination of H_2O_2 vapours concentration.

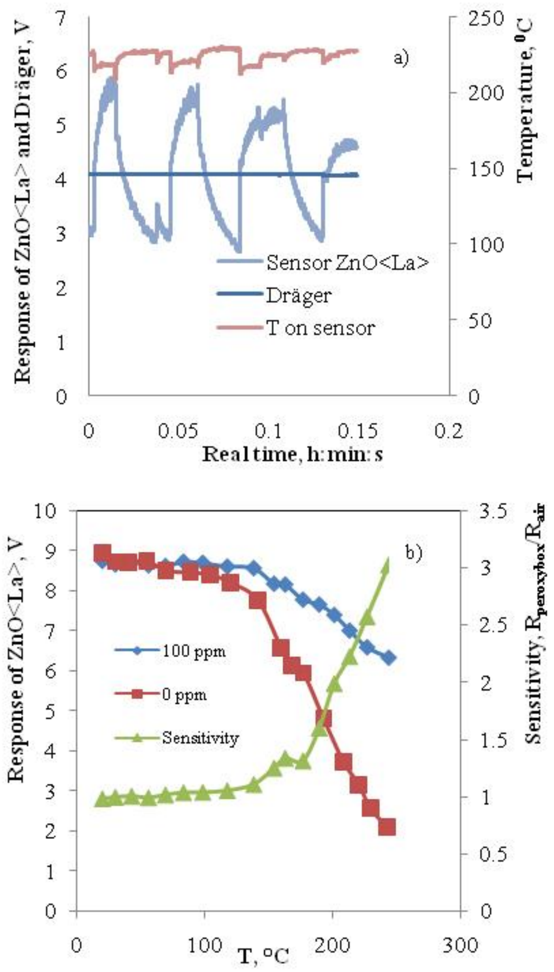

Fig. 5. The response to 10 ppm of H_2O_2 vapours at the operation temperature of 220°C (a) and the temperature dependence of sensitivity to 100 ppm H_2O_2 vapours (b) for ZnO<La> sensors.

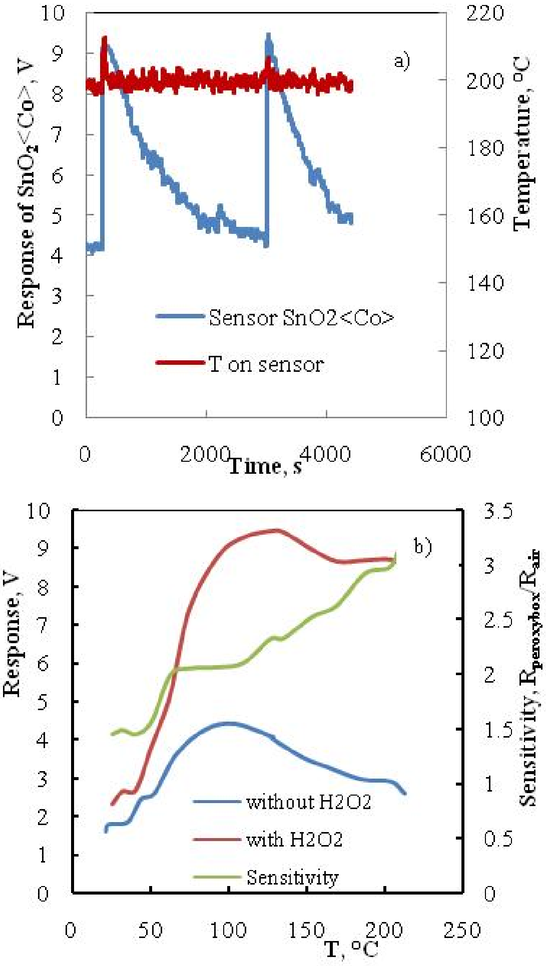

Fig. 6. The response to 75 ppm of H_2O_2 vapours at the operation temperature of 200°C (a) and the temperature dependence of sensitivity to 10 ppm H_2O_2 vapours (b) for SnO_2<Co> sensors.

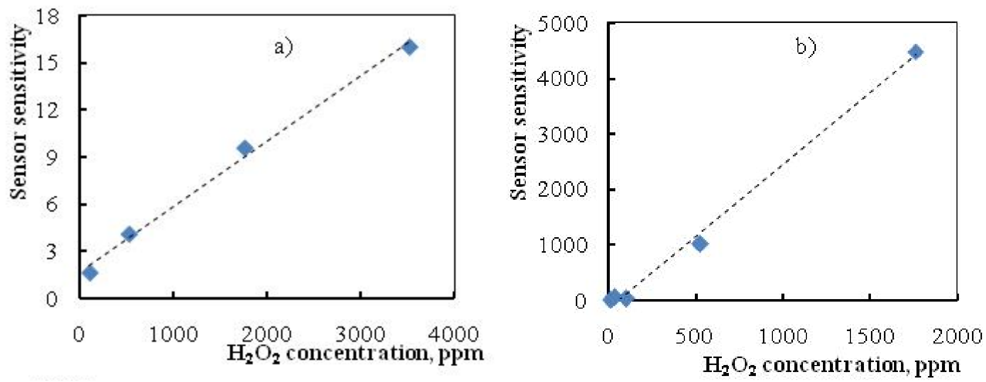

Fig. 7. The dependence of the sensitivity on H_2O_2 vapours concentration at operating temperature of 150 °C for ZnO<La> (a) and SnO_2<Co> (b) sensors.

7. Conclusions

The technology for the manufacturing of the semiconductor sensors made from ZnO doped with 1 at.% La and SnO_2 doped with 2 at.% Co nanostructured films was developed. The gas sensitive ZnO<La> and SnO_2<Co> layers were deposited onto the Multi-Sensor-Platforms using the high-frequency magnetron sputtering method. The thicknesses of the deposited doped metal oxide films were equal to 30 nm and 160 nm for ZnO<La> and SnO_2<Co>compositions, respectively. The average size of the nanoparticles was equal to 18.7 nm for both structures. Test specimens detecting H_2O_2 vapours were manufactured and investigated. The sensitivity of the prepared sensors was measured at different work body temperatures of the sensor and concentrations of H_2O_2vapours. It was found that both Co-doped SnO_2 and La-doped ZnO sensors exhibit a good response to H_2O_2 vapours at the operating temperature starting from 100 °C. The sensors made from SnO_2<Co> and ZnO<La> were sufficiently sensitive to 10 ppm of H_2O_2 vapours. It was established that the dependencies of the sensitivity on H_2O_2 vapours concentration at the work body temperature 150 °C have a linear characteristic for prepared structured and can be used for determination of H_2O_2 vapours concentration. Our future work will be directed to the long-time stabilization of sensors parameters and the improvements of such characteristics as operation speed and recovery time.

Acknowledgements

This investigation was supported by the Swiss National Science Foundation FNSNF within the framework of the SCOPES DecoComp project. Authors express gratitude to Dr. V. Kuzanyan for help in the measurements of thicknesses of our samples.

References

[1]. C.-C. Hsu, Y.-R. Lo, Y.-C. Lin, Y.-C. Shi, P.-L. Li, A spectrometric method for hydrogen peroxide concentration measurement with a reusable and cost-efficient sensor, *Sensors*, Vol. 15, 2015, pp. 25716-25729.

[2]. H. A. Rahim, B. C. Morat, R. A. Rahim, Non-invasive evaluation of hydrogen peroxide concentrations in a drinking bottle by near-linfrared spectrometry, *Sensors & Transducers*, Vol. 131, Issue 8, August 2011, pp. 83-90.

[3]. J. Sun, C. Li, Y. Qi, S. Guo, X. Liang, Optimizing colorimetric assay based on V_2O_5 nanozymes for sensitive detection of H_2O_2 and glucose, *Sensors*, Vol. 16, 2016, pp. 584-595.

[4]. C.-Y. Lin, C.-T. Chang, Iron oxide nanorods array in electrochemical detection of H_2O_2, *Sensors and Actuators B*, Vol. 220, 2015, pp. 695-704.

[5]. A.A. Ensafi, F. Rezaloo, B. Rezaei. Electrochemical sensor based on porous silicon/silver nanocomposite for the determination of hydrogen peroxide, *Sensors and Actuators B*, Vol. 231, 2016, pp. 695-704.

[6].E.A. Puganova, A.A. Karyakin, New materials based on nanostructured Prussian blue for development of hydrogen peroxide sensors, *Sensors and Actuators B*, Vol. 109, 2005, pp. 167-170.

[7]. W. Chen, S. Cai, Q.-Q. Ren, W. Wen, Y.-D. Zhao, Recent advances in electrochemical sensing for hydrogen peroxide: a review, *Analyst*, Vol. 137, 2012, pp. 49-58.

[8]. S. Chen, R. Yuan, Y. Chai, F. Hu, Electrochemical sensing of hydrogen peroxide using metal nanoparticles: a review, *Microchimica Acta*, Vol. 180, 2013, pp. 15-32.

[9]. X. Chen, G. Wu, Z. Cai, M. Oyama, Xi Chen, Advances in enzime-free electrochemical sensors for hydrogen peroxide, glucose, and uric acid, *Microchimica Acta*, Vol. 181, 2014, pp. 689-705.

[10]. B. Šljukič, C. E. Banks, R. G. Compton, Iron oxide particles are the active sites for hydrogen peroxide sensing at multiwalled carbon nanotube modified electrodes, *Nano Letters*, Vol. 6, Issue 7, 2006, pp. 1556-1558.

[11]. F. Pogacean, C. Socaci, S. Pruneanu, A.R. Biris, M. Coros, L. Magerusan, G. Katona, R. Turcu, G. Botodi, Graphene based nanomaterials as chemical sensors for hydrogen peroxide – A comparison study of their intrinsic peroxidase catalytic behavior, *Sensors and Actuators B*, Vol. 213, 2015, pp. 474-483.

[12]. X. Yang, Y. Ouyang, F. Wu, Y. Hu, Y. Ji, Z. Wu, Size controllable preparation of gold nanoparticles loading on grapheme sheets@cerium oxide nanocomposites modified gold electrode for nonenzymatic hydrogen peroxide detection, *Sensors and Actuators B*, Vol. 238, 2017, pp. 40-47.

[13]. Z.-L. Wu, C.-K. Li, J.-G. Yu, X.-Q. Chen, MnO_2/reduced graphene oxide nanoribbons: facile hydrothermal preparation and their application in amperometric detection of hydrogen peroxide, *Sensors and Actuators B*, Vol. 239, 2017, pp. 544-552.

[14]. P. Kačer, J. Švrček, K. Syslová, J. Václavík, D. Pavlík, J. Červený, M. Kuzma, Vapor phase hydrogen peroxide – method for decontamination of surfaces and working areas from organic pollutants, in: Organic pollutants ten years after the Stockholm Convention – environmental and analytical update, *InTech,* Chapter 17, 2012, pp. 399-430.

[15]. I. Taizo, A. Sinichi, K. Kawamura, Application of a newly developed hydrogen peroxide vapor phase sensor to HPV sterilizer, *PDA Journal of Pharmaceutical Science and Technology*, Vol. 52, Issue 1, 1998, pp. 13-18.

[16].J. Oberländer, P. Kirchner, H.-G. Boyen, M. J. Schöning, Detection of hydrogen peroxide vapor by use of mandanese(IV) oxide as catalyst for calorimetric gas sensors, *Physica Status Solidi A*, Vol. 211, Issue 6, 2014, pp. 1372-1376.

[17]. V. Aroutiounian, V. Arakelyan, M. Aleksanyan, A. Sayunts, G. Shahnazaryan, P. Kacer, P. Picha, J. Kovarik, J. Pekarek, B. Joost, Hydrogen peroxide vapours sensors made from ZnO<La> and SnO_2<Co> films, in *Proceedings of the Second International Conference on Advances in Sensors, Actuators, Metering and Sensing (ALLSENSORS'17)*, Nice, France, 19-23 March 2017, pp. 36-38.

[18]. F. I. Bohrer, C. N. Colesniuc, J. Park, I. K. Schuller, A. C. Kummel, W. C. Trogler, Selective detection of vapor phase hydrogen peroxide with phthalocyanine chemiresistors, *Journal of the American Chemical Society*, Vol. 130, Issue 12, 2008, pp. 3712-3713.

[19]. A. Mills, P. Grosshans, E. Snadden, Hydrogen peroxide vapour indicator, *Sensors and Actuators B*, Vol. 136, 2009, pp. 458-463.

[20]. S. Corveleyn, G.M.R. Vandenbossche, J.P. Remon, Near-infrared (NIR) monitoring of H_2O_2 vapor concentration during vapor hydrogen peroxide (VHP) sterilization, *Pharmaceutical Research*, Vol. 14, Issue 3, 1997, pp. 294-298.

[21]. J. Benedet, D. Lu, K. Cizek, J. La Belle, J. Wang, Amperometric sensing of hydrogen peroxide vapor for security screening, *Analytical and Bioanalytical Chemistry*, Vol. 395, 2009, pp. 371–376.

[22]. J. Y. Zheng, Y. Yan, X. Wang, W. Shi, H. Ma, Y. S. Zhao, J. Yao, Hydrogen peroxide vapor sensing with organic core/sheath nanowire optical waveguides,

Advanced Materials, Vol. 24, 2012, pp. OP194–OP199.
[23]. V. M. Aroutiounian, A. Z. Adamyan, E. A. Khachaturyan, Z. N. Adamyan, K. Hernadi, Z. Palai, Z. Nemeth, L. Forro, A. Magrez, E. Horvath, Study of the surface-ruthenated SnO_2/MWCNT nanocomposite thick-film gas sensors, *Sensors and Actuators B*, Vol. 177, 2013, pp. 308-315.

Sensors & Transducers, Vol. 213, Issue 6, June 2017, pp. 54-60

Sensors & Transducers

Published by IFSA Publishing, S. L., 2017
http://www.sensorsportal.com

Development of Quantum Dot-based Nanobiosensors against *Citrus Tristeza Virus* (CTV)

[1,*] Mohammad Reza SAFARNEJAD, [2] Fatemeh SAMIEE, [2] Meisam TABATABIE and [3] Afshin MOHSENIFAR

[1] Department of Plant Viruses, Iranian Research Institute of Plant Protection, Agricultural Research, Education and Extension Organization, 1454/19395, Tehran, Iran

[2] Department of Microbial Biotechnology and Biosafety, Agricultural Biotechnology Research Institute of Iran, 31359-33151, Karaj, Iran

[3] Department of Researches and Development, Nanozino, 16536-43181, Tehran, Iran

[*] Tel: +982122403012, fax:+982122403096
E-mail: mrsafarnejad@yahoo.com

Received: 5 June 2017 /Accepted: 28 June 2017 /Published: 30 June 2017

Abstract: Citrus tristeza is one of the most important diseases of citrus in the world. To avoid the destructive effect of the disease, early detection of infected plants is crucial. Therefore, simple and sensitive diagnosis tools are decisive. The main objective of the present study was developing nanobiosensors for detection of citrus tristeza based on the florescence emission of cadmium telluride quantum dots (CdTe-QDs). To achieve that, CdTe-QD particles were initially synthesized and effectively conjugated to CTV coat protein (CTV-CP) corresponding antibody. In a parallel reaction, rhodamine dye molecules were attached to the purified recombinant CTV-CP. Two independent approaches were explored for detection of the infected plants. First, in a fluorescence resonance energy transfer (FRET) based assay, the quenching ability of rhodamine molecules was applied for altering the QDs light emission. More specifically, donor-acceptor complexes (Ab-QD+CP-Rd) were created based on the affinity of antibody-antigen molecules. The resulting assembly brought Ab-QD (the donor) and the Rd-CP (the acceptor) into a close proximity and resulted in a substantial decrease in the intensity of QD light emission. Addition of free antigen into the solution resulted in the replacement of CP-Rd with free CP and a subsequent increase in the emission of QDs. In the second approach, a non-FRET based assay was performed through the addition of free antigen to the Ab-QD solution, which led to the aggregation of the Ab-QD conjugates and consequently a significant increase in the light intensity emission of the QD. To the best of our knowledge, this is the first time that the non-FRET based assay developed herein is being reported.

Keyworlds: Biosensor, Citrus, FRET, Quantum dot, Tristeza.

1. Introduction

Citrus tristeza is the most economically-destructive and widely-distributed viral disease in citrus plants worldwide [1]. The disease is caused by a flexuous rod shaped Citrus tristeza virus (CTV) [2]. The viral particles of 2000 nm in length and 12 nm in diameter, are naturally transmitted by aphids in a semi-persistent manner [3]. The CTV consists of a positive sense single-stranded RNA genome of approx. 19296 bp including 12 open reading frames encoding at least 17 proteins [4]. The viral particle consists of two capsid proteins identified as the major (p25) and minor (p27) proteins with molecular weights of 25 kDa and 27 kDa, respectively [5]. The disease symptoms are highly variable depending on some factors including virulence of the viral strain, host species, and environmental conditions. In general, the viral strains are mainly responsible for three kinds of symptoms including decline (quick and slow), stem pitting, and seedling yellows [3, 4].Protective control of CTV is mainly based on severe quarantine regulations and certification programs by grafting of virus-free scions onto CTV-tolerant rootstocks [6, 7]. Early detection is a significantly critical strategy for effective control of CTV by removing infected plants in nursery gardens and by preventing the transportation of infected plants into the clean area. Conventional detection methods suffer from a number of drawbacks and, therefore, there is an urgent need for simple, rapid, sensitive, and specific screening techniques to detect CTV at very early stages of infection. At present, the most common methods used for detection of CTV is enzyme-linked immunosorbent assay (ELISA) and polymerase chain reaction (PCR). These methods have some disadvantages limiting their application, as a case in point, ELISA based methods are time consuming and cannot detect low amounts of pathogens which is crucial for the detection of the disease in the preliminary stages of the infection [8, 9]. On the other hand, DNA based-methods are time consuming and not able to distinguish live pathogens from the dead ones [10]. More sensitive diagnostic approaches such as nanobiosensors have been proposed as alternating techniques to the conventional methods [8, 9, 11-13]. Nano-materials owing to their unique features including stable emissions and size-dependent properties have attracted a great deal of attention as transducers. Among these nanomaterials, fluorescent semiconductor nano crystals, also known as quantum dots (QDs), have been most widely used for disease diagnosis [12, 14-17]. Attractive properties of QDs as unique fluorescent label include high signal brightness, stability, size-tunable light emission, and resistance to photo-bleaching [18, 19]. These properties have been the driving reason behind the wide interest in using QDs in the development of biosensors and immune-histochemical kits [19, 20].

The present article describes two specific and sensitive QD-based biosensors for rapid detection of CTV infected plants.

2. Material and Methods

2.1. Plant Materials

Plant samples including shoots, fully expanded leaves, and peduncles were collected from different citrus trees growing in different orchards in northern part of Iran, i.e. Sari region in Mazandaran province. Young leaves were collected from four different locations around the canopy, placed in marked plastic bags, and were transferred to the laboratory on ice.

2.2. Initial Detection of Infected Plants

The presence of CTV in the collected plant samples were confirmed by a commercial DAS-ELISA kit (Bioreba, Switzerland) as described [21]. Briefly, a 96-wells microtiter plate was coated with purified anti-cp antibody diluted to 1/1000 in PBS and incubated at 37 °C for 2 h. The extraction of the plant sap from healthy and infected citrus trees was carried out by crushing 0.1 g leaves in liquid nitrogen followed by suspension in 1 ml extraction buffer (Tris buffer pH7.4 containing 137 mM NaCl, 3 mM KCl, 2 % PVP 24 kDa, 0.05 % Tween20 and 0.02 % NaN_3). The plant extracts and purified protein control (CP positive control) were added to the plate and incubated overnight at 4 °C. Subsequently, the alkaline-phosphatase conjugated anti-CP polyclonal antibody at a dilution rate of 1:1000 was added to the sample and incubated at 37 °C for 30 min. Finally, the absorbance values were read at 405 nm. The sample was positively identified if the mean DAS-ELISA (A405nm) value of the samples exceeded at least twice the mean values of the healthy control.

2.3. Preparation of CdTe-QDs

The preparation and synthesis of CdTe-QD particles was performed using the optimized protocol described earlier [22]. Briefly, in the presence of thiolglycolic acid (TGA), a fresh solution of Sodium hydrogen telluride (NaHTe) was added steadily to N_2-saturated $CdCl_2.2.5H_2O$. The mixture was then heated at 92 °C and stirred in a reflux system under nitrogen atmosphere. To remove the excess amount of Cd2+and TGA, the solution was washed three times with ethanol and spun at 4000×g for 15 min. The pellet was re-suspended again in 250 mL double distilled water and refrigerated.

2.4. Antibodies Preparation

To prepare specific antibodies against the CTV particles, purified recombinant CTV-CP was used for immunization of rabbits. The recombinant protein was prepared and affinity-purified as described in our previous report [23]. Two-month-old female white New Zealand rabbits were injected intramuscularly with the antigen. The first injection contained about 100 µg of the recombinant CP (20 µl) protein and 500 µl of Freund's complete adjuvant, mixed with 480 µl PBS 1× (137 mm NaCl, 2.7 mm KCl, 10 mm Na_2HP0O_4, 2mM KH_2Po_4 pH7.4) while incomplete Freund's adjuvant was used for the subsequent injections with 100 µg purified recombinant IMP diluted by an identical volume of Freund`s adjutant. Antibody purification from the serum was performed using protein A spin column according to the manufacturer's instructions (AbD serotec,UK). Concentration of the purified antibody was estimated on a SDS-PAGE.

2.5. Conjugation of Antibodies with QDs

In order to conjugate CTV antibodies and QD particles (Ab-QDs), 200 µg of QDs and 50 µg of the specific purified CTV immunoglobulins were mixed, pH 7.4 and the volume of solution was increased to 100 µl. After that, 150 µL of the freshly-prepared EDC solution (1-Ethyl-3-[3-dimethylaminopropyl] carbodiimide hydrochloride) (4.2 mg/mL) was added to the mixture and stirred 2 h at room temperature in the dark. The solution was then kept at 4 °C overnight. The prepared Ab-QDs conjugate subsequently separated by centrifugation at 20,000×g for 20 min. The pellet containing Ab-QDs conjugates was then dispersed by 1.5 mL of 1× PBS solution pH 7 and was stored at 4 °C in the dark.

2.6. Conjugation of CTV-CP with Rhodamine

The recombinant coat protein of the CTV was conjugated to rhodamine 123 molecules *via* aldehyde intermediates (CP-Rd). To achieve this, around 100 µl CP (5 µg/ml) was gently added to 360 µl Glutaraldehyde 10 %. Subsequently, 2 µl of dinitroprydin was added to the mixture under stirring and mixed for 30 min. Then 1 mg of $NaBH_4$ was added and the mixture was stored for 1 h at room temperature. The CP-Rd conjugates were then separated from the excess antigen *via* dialysis using 1× PBS pH 7. In fact, rhodamine 123 was used as a quencher in developed nanosensing system.

2.7. The Fluorometry Assay

A UV-VIS Spectrophotometer MultiSpec-1501 (Shimadzu, Japan) was used for fluorometric assays. The excitation of the CdTe QDs was adjusted at 380 nm. To cover the emission wavelength of the fluorophore molecules, the emission spectra were adjusted at between 500 and 640 nm. The bandwidth of the device was fine-tuned at 5 nm.

2.8. Nanobiosensor Fabrication and Evaluation

The major components of the developed nanobiosensor included the bio-conjugates of Ab-QD and CP-Rd. The presence of the antigen in the solution was estimated *via* two independent FRET- and non-FRET based approaches. In the first method, defined amounts of Ab-QD (2 µl) and CP-Rd (10 µl) diluted in 1×PBS were added into a 100 µl fluorometer well. The obtained spectrum showed that the baseline emission of QD particles was quenched by the rhodamin molecules. For detection of the native and/or recombinant antigen in the solution, 2 µl of the plant extract and/or recombinant CP was then added to the same fluorometer well and the second spectrum was acquired. In the presence of the foreign antigen, the emission intensity of the QD would be increased and the baseline would be recovered.

In the second non-FRET based approach, there was no need for the presence of CP-Rd, and the mixture only contained defined amounts of Ab-QD (2 µl) and antigen (2 µl) diluted in 96 µl of PBS. The sample was loaded in a fluorometer well and the presence of antigen was detected by improving of the light emitted by the QD particles. In the both mentioned approaches, the samples were marked as negative when no baseline shift was observed.

3. Results

3.1. Preparation of Antibody

A rapid immunoassay method employing QDs for detection of citrus tristeza is described herein. First, for preparation of specific polyclonal antibody against CTV particles, immunization of two rabbits was performed by intramuscularly injecting the purified recombinant CTV-CP. The antibody titer was determined after each boosting, and after 6 weeks when the antibody titer exceeded 1:65000, blooding was performed and the whole serum was obtained. An affinity column containing staphylococcus protein A was used for purification of the IgG molecules. The IgG purity and integrity was monitored by SDS-PAGE in which distinct bands with molecular weights of around 25kDa and 50kDa pertaining to the light and heavy chains, respectively, were observed (Fig. 1). Furthermore, the concentration of the IgG was measured at approx. 1mg. ml^{-1} by direct comparison with known amounts of a standard protein, i.e., BSA.

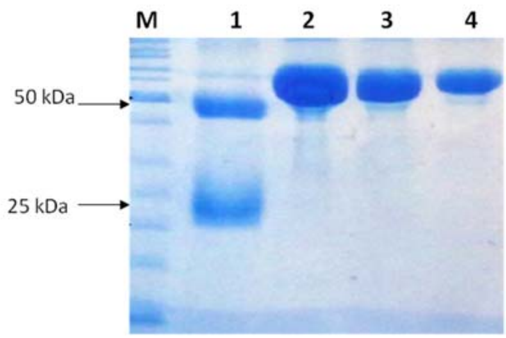

Fig. 1. SDS-PAGE analysis of the affinity purified immunogloboline. M: unstained protein molecular weight marker SM0431 (Fermentas, Vilnius, Lithuania); 1: purified antibody; 2: BSA 3500µg ml-1, 3: BSA 1700 µg ml-1, 4: BSA 750 µg ml-1.

The feasibility of the prepared antibody for detection of infected plants was analyzed by a serological approach. The results proved a high specificity against the recombinant CTV-CP protein as well as against the native virus particles within the infected plant samples (data not shown).

3.2. Construction of Biosensors

For developing of nanobiosensors, the QD particles were used as fluorophore and were conjugated to IgG molecules. For efficient coupling of Ab-QD, the surface of the CdTe QD particles were initially surface modified by thioglycolic acid (TGA). Then, purified IgG molecules against CTV were immobilized on their shells. This was accomplished thanks to the hydrophilic behavior of the QD particles resulting in the attraction of IgGs onto their surfaces [24]. The rhodamine 123 molecules were used as an acceptor for quenching the light emitted from QD particles. For this aim, the purified recombinant CTV-CP was used for conjugation to rhodamine *via* aldehyde intermediate using the 27 free amine groups (lysine) of the CTV-CP. Rhodamine 123 as a fluorescent molecule can be detected easily and inexpensively with fluorometers. The absorption and emission spectra of the pure solution of CdTe QDs and rhodamin are shown in Fig. 2. As presented, the maximum emission peak of the QDs takes place at 522 nm while the maximum emission peak of rhodamine is at 580 nm. Therefore, adddion a mixture of Ab-QD and CP-Rd into a same well would lead to a significant decrease in the emission light of the Ab-QD conjugates (Fig. 2 and Fig. 3.A). This is due to the quenching effect of rhodamine on the emitted light of QDs occurring in a FRET system where Ab-QD and CP-Rd are involved in a specific antigen-antibody interaction.

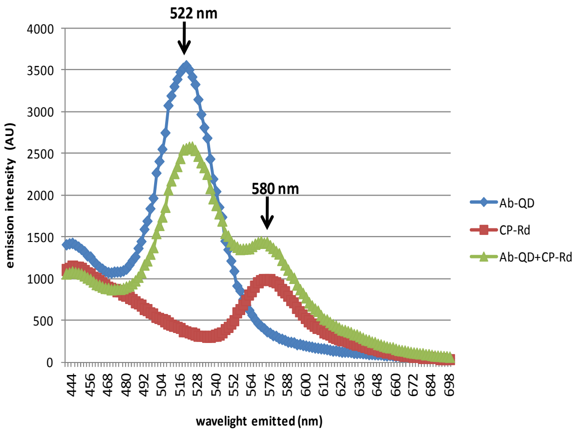

Fig. 2. Developing of FRET assay by applying of Ab-QD and CP-Rd. The excitation is done by a light with 390 nm wavelength and maximum value of emission obtained in 522 nm. The Y axis shows emission intensity by fluorescence arbitrary units (AU).

Ab-QD: The spectrum derived from excitation of Ab-QD particles.

CP-Rd: The spectrum derived from excitation of CP-Rd.

Ab-QD+CP-Rd: The spectrum derived from excitation of solution containing Ab-QD particles and CP-Rd.

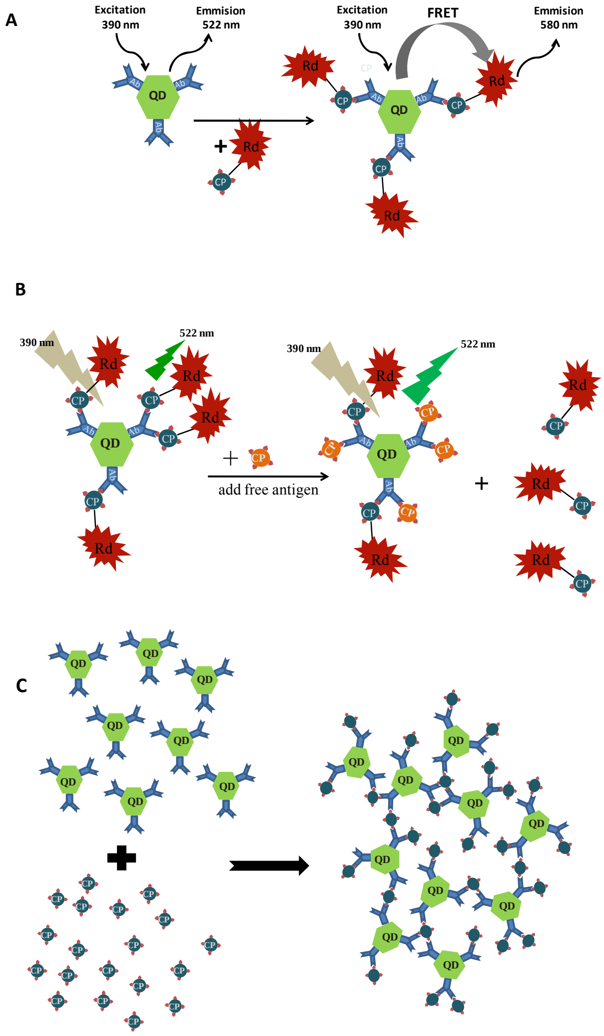

Fig. 3. Schematic presentation of specific CTV nanobiosensor: (A) Occurring of FRET in presence of Ab-QD and CP-Rd, (B) the FRET-based mechanism for detection of infected CTV plant, (C) Non-FRET based mechanism for detection of infected CTV plant.

3.3. The FRET based Nanobiosensor

In the first approach for detection of CTV, the FRET-based nanobiosensor was used in which the emission intensity of the Ab-QDs alone was measured at around 5700 AU; however, after the addition of Rd-CP, this value showed a downward shift peaking at 2200 AU (Fig. 4) and this was considered as base line spectra. Subsequently, the addition of the recombinant or native antigen (CTV-CP) led to a significant increase in the emission intensity from the base line curve. This was due to the loss of the quenching effect of rhodamine on QD particles (Fig. 3.B). In better words, this increase was ascribed to the separation of the CP-Rd from the Ab-QD in response to the presence of free antigens.

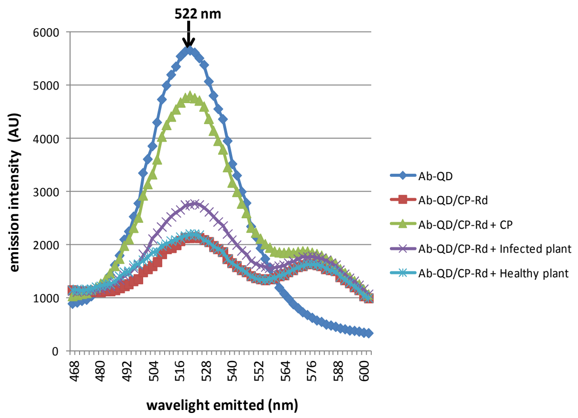

Fig. 4. Detection of infected plant by FRET based nanobiosensor. The excitation is done by a light with 390 nm wavelength and maximum value of emission obtained in 522 nm. The Y axis shows emission intensity by fluorescence arbitrary units (AU).

Ab-QD: The spectrum derived from excitation of Ab-QD particles alone

Ab-QD/CP-Rd: The spectrum derived from excitation of a solution containing Ab-QD particles and CP-Rd.

Ab-QD/CP-Rd + CP: The spectrum derived from excitation of a solution containing Ab-QD particles, CP-Rd and recombinant CTV-CP.

Ab-QD/CP-Rd + Infected plant: The spectrum derived from excitation of a solution containing Ab-QD particles, CP-Rd and extract of infected plant.

Ab-QD/CP-Rd + Healthy plant: The spectrum derived from excitation of a solution containing Ab-QD particles, CP-Rd and extract of healthy plant.

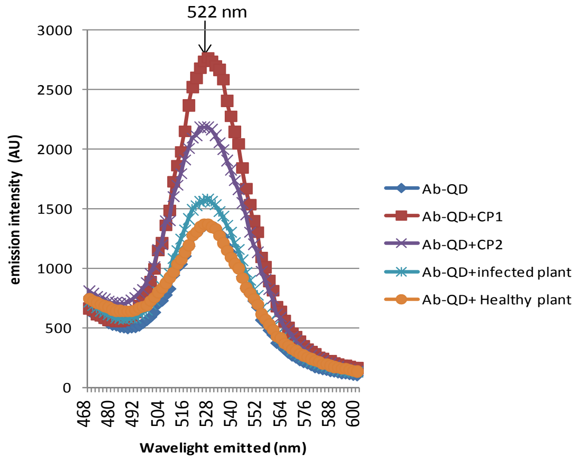

Fig. 5. Detection of infected plant by non-FRET based nanobiosensor. The excitation is done by a light with 390 nm wavelength and maximum value of emission obtained in 525 nm. The Y axis shows emission intensity by fluorescence arbitrary units (AU).

Ab-QDs: The fluorometric peak of Ab-QDs conjugates alone.

Ab-QD+CP1: The fluorometric peak of Ab-QDs conjugates and recombinant CTV-CP (700ng/ml) complex.

Ab-QD+CP2: The fluorometric peak of Ab-QDs conjugates and and recombinant CTV-CP (500ng/ml) complex.

Ab-QD+infected plant: The fluorometric peak of Ab-QDs conjugates and extract of infected plant.

Ab-QD+ Healthy plant: The fluorometric peak of a solution containing extract of healthy plant alone.

3.4. The Non-FRET based Nanobiosensor

In a separate assay, the non-FRET based nanobiosensor, i.e., the capability of the Ab-QD particles alone for the detection of infected plant samples without applying CP-RD, was evaluated. Herein, the detection was mainly based on the aggregation of Ab-QD particles by the addition of antigens. In this approach, the addition of the recombinant CTV-CP to Ab-QD solution would lead to aggregation of Ab-QD particles by CP molecules. Under this situation, the aggregates emitted lights of a higher intensity when exited at 390 nm (Fig. 3.C). Applying the recombinant CP and crude extract of the infected plants confirmed the specificity of the nanobiosensor for the detection of CTV infected plants (Fig. 5).

The comparative analysis of two above described approaches showed that the non-FRET based method is more sensitive for detection of CTV-CP in the solution. The limit of detection (LOD) was calculated based on LOD= 3S0/ K equation, here S0 is the standard deviation of blank measurements (*n*=6) and K is the slope of calibration curve. The detection limit of FRET and non-FRET based methods was estimated around 198 ng/ml and 246 ng/ml of purified CTV-CP, respectively. Based on our knowledge, this non-FRET based detection approach is firstly described here for detection of specific antigen in a solution.

4. Discussion

Present article describe construction of two specific and novel nanobiosensor s against CTV that could be easily used for efficient detection of infected plants. The bio-receptor part of these sensors comprised of specific antibody against the CTV-CP that is able to detect presence of cognate antigen, CTV, in a solution. It is believed that the attachment of antibody-antigen molecules are completed by several non-covalent interactions. These types of attachments are not so strong and in a distinct antibody-antigen complex, the antigen moiety could be replaced by free antigen molecules in the solution (Safarnejad et al., 2011).

Herein, the major part of the constructed biosensors is cadmium telluride quantum dot particle. These luminescent colloidal semiconductor nanocrystals are well-suited for sensing and biotechnological applications. These worth full particles do not suffer from current limitations of organic dyes and exhibit size-dependent tunable, having broad absorption with narrow fluorescence emission spectra. [25, 26].

The first developed nanobiosensor comprised of CP-Rd and Ab-QD which sense presence of foreign antigen, CTV, on a FRET-based mechanism (Fig. 2 and Fig. 3.A). More specifically, when a sample containing free coat proteins of CTV in a solution was added to the mixtures of pre-bound CP-Rd/Ab-QD, the CP-Rd moiety was replaced by the free CP in the investigated sample. This led to a decrease in the quenching ability of the CP-Rd against the Ab-QD leading to a recovery of the fluorimeteric curve in comparison with the curve previously obtained for the Rd-CP/Ab-QD conjugates. This could be explained through the optical quenching mechanism of the QD-Ab domain by the CP-Rd domain based on the Forster dipole–dipole interaction model [24]. In other words, the inorganic dye, i.e., rhodamine (a fluorescence acceptor) conjugated to the antigen (CTV-CP), occupied the peptide binding pocket of the antibody, i.e., anti-CTV polyclonal antibody. Therefore, when the free CTV-CP derived from the pathogenic agent was added, it displaced the rhodamine-CP domain in the Rd-CP/Ab-QD conjugates, resulting in a increase of fluorescence emission by the displaced Ab-QD which was no longer quenched by the CP-Rd molecules (FRET) (Fig. 2 and Fig. 3.A). Moreover, higher free native CTV-CP concentrations in the infected sample would be translated into fluorimeter curves peaking at higher photoluminescence (PL) intensity. FRET has been successfully applied for detection of several important plant pathogens and toxins [8, 27-30].

In the non-FRET based detection approach, the addition of the free antigen molecules into the reaction solution would lead to self-assembling of Ab-QD molecules into microscale aggregates in the presence of free CP subunits through antibody-antigen molecular recognition. This would lead to a higher intensity of the light emitted by the QD particles. Soman and Giorgio [31] used this approach in a flow cytometry assay for rapid and simultaneous detection of Angiopoietin-2 (Ang2) and vascular endothelial growth factor A (VEGF).

5. Conclusion

This designed nanobiosensor showed a high performance for detection of the infected plants. No cross reaction was detected by applying healthy citrus plants as well as those infected with other diseases such as witches broom disease of lime (WBDL) and citrus bacterial cankers. The developed nanobiosensor showed a complete accuracy in detecting the infected samples carrying the CTV particles. In general, the method described herein showed several advantages over the conventional detection methods, including simplicity and higher sensitivity in the detection of the pathogens in plant.

6. Acknowledgment

We appreciate the financial support of this work provided by Iran national science foundation (INSF).

References

[1]. Rocha-Pena, M. A., Lee, R. F., Lastra, R., Niblett, C., Ochoa-Corona, F. M., Garnsey, S. M., Yokomi, R. K, Citrus tristeza virus and its aphid vector toxoptera citricida: Threats to citrus production in the carribean and central and north america, *Plant Disease,* 79, 1995, pp. 437-445.

[2]. Bar-Joseph, M., Che, X., Mawassi, M., Gowda, S., Satyanarayana, T., Ayllón, M., Albiach-Martí, M., Garnsey, S., Dawson, W., The continuous challenge of citrus tristeza virus molecular research, in *Proceedings of the Proceedings of the 15th Conference of the International Organization of Citrus Virologists,* Paphos, Cyprus, 11-16 November 2001, pp. 1-7, ref. 37.

[3]. Bar-Joseph, M., Lee, R., Citrus tristeza virus, *AAB Descriptions of Plant Viruses* 1989, 353.

[4]. Niblett, C., Genc, H., Cevik, B., Halbert, S., Brown, L., Nolasco, G., Bonacalza, B., Manjunath, K., Febres, V., Pappu, H., Progress on strain differentiation of citrus tristeza virus and its application to the epidemiology of citrus tristeza disease, *Virus Research,* 71, 2000, pp. 97-106.

[5]. Moreno, P., Ambros, S., Albiach-Martí, M. R., Guerri, J., Pena, L., Citrus tristeza virus: A pathogen that changed the course of the citrus industry, *Molecular Plant Pathology,* 9, 2008, pp. 251-268.

[6]. Vidal, E., Yokomi, R., Moreno, A., Bertolini, E., Cambra, M., Calculation of diagnostic parameters of advanced serological and molecular tissue-print methods for detection of citrus tristeza virus: A model for other plant pathogens, *Phytopathology,* 102, 2012, pp. 114-121.

[7]. De Boer, S. H., López, M. M., New grower-friendly methods for plant pathogen monitoring, *Annual Review of Phytopathology,* 50, 2012, pp. 197-218.

[8]. Rad, F., Mohsenifar, A., Tabatabaei, M., Safarnejad, M., Shahryari, F., Safarpour, H., Foroutan, A., Mardi, M., Davoudi, D., Fotokian, M., Detection of candidatus phytoplasma aurantifolia with a quantum dots fret-based biosensor, *Journal of Plant Pathology,* 94, 2012, pp. 525-534.

[9]. Davarani, F. H., Safarpour, H., Safarnejad, M. R., Mohsenifar, A., Mahmoudi, S. B., Kakoueinejad, M., Tabatabaei, M., Large-scale high throughput screening of sugar beet germplasm using a nanobiosensor and its comparison with elisa method for resistance to polymyxabetae, *Euphytica,* 200, 2014, pp. 389-399.

[10]. Kingsnorth, C., Asher, M., Keane, G., Chwarszczynska, D., Luterbacher, M., Mutasa-Göttgens, E., Development of a recombinant antibody elisa test for the detection of polymyxa betae and its use in resistance screening, *Plant Pathology,* 52, 2003, pp. 673-680.

[11]. Kalarestaghi, A., Bayat, M., Hashemi, S. J., Razavilar, V., Highly sensitive fret-based fluorescence immunoassay for detecting of aflatoxin b1 using magnetic/silica core-shell as a signal intensifier, *Iranian Journal of Biotechnology,* 13, 2015, pp. 25-31.

[12]. Holzinger, M., Le Goff, A., Cosnier, S., Nanomaterials for biosensing applications: A review, *Frontiers in Chemistry,* 2, 2014, p. 63.

[13]. Khiyami, M. A., Almoammar, H., Awad, Y. M., Alghuthaymi, M. A., Abd-Elsalam, K. A., Plant pathogen nanodiagnostic techniques: Forthcoming

changes? *Biotechnology & Biotechnological Equipment,* 28, 2014, pp. 775-785.

[14]. Frasco, M. F., Chaniotakis, N., Semiconductor quantum dots in chemical sensors and biosensors, *Sensors,* 9, 2009, pp. 7266-7286.

[15]. Frasco, M. F., Chaniotakis, N., Bioconjugated quantum dots as fluorescent probes for bioanalytical applications, *Analytical and Bioanalytical Chemistry,* 396, 2010, pp. 229-240.

[16]. Barroso, M. M., Quantum dots in cell biology, *Journal of Histochemistry & Cytochemistry,* 59, 2011, pp. 237-251.

[17]. SalmanOgli, A., Nanobio applications of quantum dots in cancer: Imaging, sensing, and targeting, *Cancer Nanotechnology,* 2, 2011, pp. 1-19.

[18]. Pinaud, F., Michalet, X., Bentolila, L. A., Tsay, J. M., Doose, S., Li, J. J., Iyer, G., Weiss, S., Advances in fluorescence imaging with quantum dot bio-probes, *Biomaterials,* 27, 2006, pp. 1679-1687.

[19]. Xing, Y., Chaudry, Q., Shen, C., Kong, K. Y., Zhau, H. E., Chung, L. W., Petros, J. A., O'regan, R. M., Yezhelyev, M. V., Simons, J. W., Bioconjugated quantum dots for multiplexed and quantitative immunohistochemistry, *Nature Protocols,* 2, 2007, pp. 1152-1165.

[20]. Yezhelyev, M. V., Gao, X., Xing, Y., Al-Hajj, A., Nie, S., O'Regan, R. M., Emerging use of nanoparticles in diagnosis and treatment of breast cancer, *The Lancet Oncology,* 7, 2006, pp. 657-667.

[21]. Clark, M. F., Adams, A., Characteristics of the microplate method of enzyme-linked immunosorbent assay for the detection of plant viruses, *Journal of General Virology,* 34, 1977, pp. 475-483.

[22]. Shanehsaz, M., Mohsenifar, A., Hasannia, S., Pirooznia, N., Samaei, Y., Shamsipur, M., Detection of helicobacter pylori with a nanobiosensor based on fluorescence resonance energy transfer using cdte quantum dots, *Microchimica Acta,* 180, 2013, pp. 195-202.

[23]. Shahryari, F., Shams-Bakhsh, M., Safarnejad, M. R., Safaie, N., Ataei Kachoiee, S., Preparation of antibody against immunodominant membrane protein (imp) of candidatus phytoplasma aurantifolia, *Iranian Journal of Biotechnology* 11, 2013, pp. 14-21.

[24]. Zhou, M., Ghosh, I., Quantum dots and peptides: A bright future together, *Peptide Science,* 88, 2007, pp. 325-339.

[25]. Goldman, E. R., Mattoussi, H., Anderson, G. P., Medintz, I. L., Mauro, J. M., Fluoroimmunoassays using antibody-conjugated quantum dots, *NanoBiotechnology Protocols,* 2005, pp. 19-34.

[26]. Mattoussi, H., Mauro, J. M., Goldman, E. R., Anderson, G. P., Sundar, V. C., Mikulec, F. V., Bawendi, M. G., Self-assembly of cdse− zns quantum dot bioconjugates using an engineered recombinant protein, *Journal of the American Chemical Society,* 122, 2000, pp. 12142-12150.

[27]. Safarpour, H., Safarnejad, M. R., Tabatabaei, M., Mohsenifar, A., Rad, F., Basirat, M., Shahryari, F., Hasanzadeh, F., Development of a quantum dots fret-based biosensor for efficient detection of polymyxa betae, *Canadian Journal of Plant Pathology,* 34, 2012, pp. 507-515.

[28]. Shojaei, T. R., Salleh, M. A. M., Sijam, K., Rahim, R. A., Mohsenifar, A., Safarnejad, R., Tabatabaei, M., Detection of citrus tristeza virus by using fluorescence resonance energy transfer-based biosensor, *Spectrochimica Acta Part A: Molecular and Biomolecular Spectroscopy,* 169, 2016, pp. 216-222.

[29]. Mahdi, M., Mansour, B., Afshin, M., Competitive immunoassay for ochratoxin a based on fret from quantum dot-labeled antibody to rhodamine-coated magnetic silica nanoparticles, *Microchimica Acta* 183, 2016, pp. 3093-3099.

[30]. Ma, G., Cheng, Q., Manipulating fret with polymeric vesicles: Development of a "mix-and-detect" type fluorescence sensor for bacterial toxin, *Langmuir,* 22, 2006, pp. 6743-6745.

[31]. Soman, C., Giorgio, T., Sensitive and multiplexed detection of proteomic antigens via quantum dot aggregation, *Nanomedicine: Nanotechnology, Biology and Medicine,* 5, 2009, pp. 402-409.

Published by International Frequency Sensor Association (IFSA) Publishing, S. L., 2017 (http://www.sensorsportal.com).

Sensors & Transducers, Vol. 213, Issue 6, June 2017, pp. 61-67

Sensors & Transducers
Published by IFSA Publishing, S. L., 2017
http://www.sensorsportal.com

Implantable Medical Device for Measuring Electrocardiogram to Improve Human Wellness

Jong-Ha Lee
Dept. of Biomedical Engineering, Keimyung University, Daegu, South Korea
E-mail: segeberg@gmail.com

Received: 2 June 2017 /Accepted: 28 June 2017 /Published: 30 June 2017

Abstract: Prolonged monitoring is more likely to diagnose atrial fibrillation accurately than intermittent or short-term monitoring. In this study, an implantable electrocardiograph (ECG) sensor to monitor atrial fibrillation patients in real time was developed. The implantable sensor is composed of a micro controller unit, an analog-to-digital converter, a signal transmitter, an antenna, and two electrodes. The sensor detects ECG signals from the two electrodes and transmits these to an external receiver carried by the patient. Because the sensor continuously transmits signals, its battery consumption rate is extremely high; therefore, the sensor includes a wireless power transmission module that allows it to charge wirelessly from an external power source. The integrated sensor has the approximate dimensions 0.12 in × 1.18 in × 0.19 in, which is small enough to be inserted into a patient without the need for major surgery. The signal and power transmission data sampling rate and frequency of the unit are 300 samples/s and 430 Hz, respectively. To validate the developed sensor, experiments were conducted on small animals.

Keywords: wireless health monitoring; electrocardiography; implant sensor; body sensor network; biochip.

1. Introduction

There are numerous medical problems whose treatment requires the constant monitoring of vital signs from several body organs. Although patients are typically hospitalized and kept under observation using wired equipment to measure vital signs, remote patients must stay at home along with expensive monitoring equipment and dedicated medical staff, which increases medical expenditure and reduces human resources available at the hospital. Several studies have therefore been conducted recently in researching and developing wearable and implantable biomedical devices, and progress in this field has provided benefits in terms of lower costs, freer patient movement, and uninterrupted diagnostic data streams for medical monitoring. Wireless biomedical devices can provide enhanced mobility and efficiency with minimum disruption of monitored data [1], and networks based on biomedical sensors can create effective solutions for distributing patient information along multiple platforms.

Diabetes and cardiovascular diseases are two health conditions that require effective, round-the-clock monitoring. Twenty four percent of the population of developed countries has diabetes and related complications such as cardiovascular diseases, making this a widespread health issue that can only be addressed through active monitoring of blood glucose levels (BGL) [2].

The vital signs that are most often monitored in health diagnostics are:

- Blood glucose level;
- Blood pressure and pulse rate;
- Electrocardiograph (ECG);
- Respiration efficacy.

Advancements in the use of wireless technologies in biomedical implant design have opened avenues for marked improvement in medical care and diagnostic systems as wired equipment is replaced with implanted on-body sensors. Biomedical implant-based monitoring systems can wirelessly transmit data consisting of critical information related to patient health. Implant-based vital-sign monitoring allows for round-the-clock monitoring and health management, with updates provided on handheld devices using wireless protocols. A range of medical diagnoses can be performed using implants through the monitoring of parameters such as blood pressure, glucose level, and cardiac response. However, efficient invasive monitoring using wireless biomedical implants comes with numerous challenges that must be addressed beforehand.

Research on implants has progressed significantly in the last decade and is being actively pursued owing to the viability of implants in a broad range of applications including medicine, health, and sports. On-time diagnostics have become a major benefit for patients with chronic diseases as the continuous monitoring of health indicators can significantly assist in curtailing emergency events. The design of wireless biomedical implants is a difficult task, however, as there are many challenges that must be addressed for operational systems. Some important key issues are:

- Power Requirements: Biomedical implants vary in power requirements based on their operational issues. To improve implant lifetime and range of communication, and because excessive power dissipation by a medical implant can seriously increase the chances of tissue damage [3], low power consumption is generally sought. Implants can be powered using batteries or wireless power transfer; however, batteries are bulky, hazardous, and require recurrent replacement, while wireless power allows for continuous power transfer, making it more suitable for 24-hour monitoring systems.
- Sensors and Communication: Accurately reading and monitoring signals from a human body requires sensitive transducers and amplification units. Algorithms for the interpretation of signals must also be carefully designed to cater to any signal pattern anomalies in a timely manner. Wireless system must also be carefully designed to comply with power requirements and transmission ranges [4].
- Implant Size: Implant size has serious impacts on overall design [5]. Power requirements, carrier frequency, and transducer design are all primarily governed by the size of the implant, which in turn is governed by where in the body the implant is placed. Smaller implants also allow for minimally invasive surgical procedures.
- Reliability: The reliability and efficacy of an implantable medical device are paramount for enabling active monitoring and timely warning under emergency situations. In cardiac cases in particular, emergencies can be avoided through the use of implants that can produce reliable measurements. Good reliability will also reduce the need for periodic surgery in order to install replacements. To sustain future requirements ensuring the viability of biomedical implant technology, prolonged reliability is essential.

The above concerns must be kept in mind when designing an implant as they represent the major limiting factors for advances in implant technology. In this study, an implantable ECG sensor using wireless communication and power transmission was developed. With the increased pace of living in contemporary society and the related reliance on tobacco, alcohol, and caffeine, the number of patients with heart conditions such as arrhythmia is increasing. Arrhythmia (also known as cardiac dysrhythmia) is caused by an abnormal ejection fraction and presents as an irregular heartbeat that is either faster (tachycardia) or slower (bradycardia) than the usual heart rate. It can occur unexpectedly anytime and anywhere and can lead to shortness of breath, dizziness, and fainting; in serious cases, it can cause sudden cardiac arrest owing to non-contraction of the ventricles, resulting in a life-threatening myocardial infarction (heart attack). An electrocardiogram (or electrocardiograph) (ECG) can be used to detect cardiac abnormalities and thus predict arrhythmia. The ECG produces a graph on which changes in electrical potential associated with the pattern of the heartbeat are recorded. Measurements using an ECG can be performed with either patch- or insertion-type ECG sensors. The most widely used ECG sensor is the standard patch-type 12-lead ECG, in which electrodes are attached to the four limbs and to the anterior chest near the heart in order to measure and record ECG signals using standard limb, unipolar limb, and chest leads. However, in the case of arrhythmia a short-term ECG measurement is of little help because of the short duration of symptoms; it is therefore necessary to use an ECG device that can be carried by the patient and has electrodes attached to the body's surface. The heart rhythm can be recorded using either a Holter monitor or an implantable loop recorder (ILR) surgically inserted under the skin. Unfortunately, the Holter monitor is inconvenient as it disrupts daily activities because it must be worn constantly. Although the insertion-type ILR is more comfortable as it is implanted into the body and does not need to be carried, its use requires surgical intervention for implantation, which raises safety and confidence issues. In addition, a similar surgical procedure is necessary at the end of battery life to either replace or remove it, which again raises safety and cost issues.

The drawbacks of ILR can be overcome through the use of a quasi-permanent battery that is recharged via wireless power transmission. While this is technically possible, further investigation of effects on the human body must be conducted before such systems can be considered safe and reliable. Therefore, in this study an insertion-type wireless ECG sensor was developed and its performance within a human body phantom was tested using a thermal imaging camera. Further tests of the implanted sensor were then conducted on an animal model. Based on the results of these tests, it was possible to identify any potential problems that could occur in the use of a wireless ECG sensor.

In this study, a micro-sized implantable electrocardiogram (ECG) sensor was developed, as such devices generally provide a high diagnostic yield. The dimensions of the integrated sensor are approximately 0.12 in × 1.18 in × 0.19 in, which is an appropriate size for insertion by a cardiologist into a patient without the need for major surgery. The advantages of the use of this sensor include continuous monitoring ability and the capability for capturing all asymptomatic and symptomatic episodes as long as the unit is worn continuously. The proposed sensor was validated with shielding experiments that mimicked the action of the implant and the shielding of sensor effects. The sensor was placed into cylindrical cases composed of three different materials: quartz, titanium, and acryl. To mimic the generation of ECG signals, an ECG simulator was attached to the sensor. The experiments showed that the sensor transmits ECG signals correctly with all three different types of case material, with the quartz material producing the best results among the three by transmitting data with no distortion.

2. System Design Concepts

In this section, the design concept of the implantable ECG sensor are presented. Numerical simulations were performed to verify the principle behind sensor and tactile images of phantom tissue inclusions were obtained.

2.1. Cardiac ECG Measurement and Electrodes

Cardiac activity is normally monitored by recording electrocardiograph (ECG) signals in a clinical setting, which requires the physical presence of the patient at the facility. The ECG signal is composed of multiple electrical activities that begin from the sinus at the top of the right atrium. The signal is generated from the sinus node and propagates through the atrioventricular (AV) node. One cardiac cycle consists of a P wave, a T wave, and a QRS complex, all of which were identified by Willem Einthoven. When a sinus node releases an electrical impulse, it creates the basis for an atrial depolarization leading to atrial contraction, which is sensed as a P wave. The signal then passes through the AV node, where the QRS complex signal is induced by ventricular depolarization and is followed by generation of a T wave from the re-polarization of the ventricular.

Monitoring heart activity through ECG signals is carried out using at least three electrodes placed on specific points on the skin in order to sense electrical signals generated by heart constituents. The Holter monitor is one such diagnostic device and is commonly employed for active monitoring of heart activity after major heart procedures [6]. Holter monitors have proven technologically capable but are large, must be connected to electrodes using wires that limit free movement of the patient, and require continuous placement of electrodes for long term monitoring. Standard Holter monitors are therefore incapable of providing smooth and seamless unobtrusive continuous monitoring, and although Holter devices have evolved over the past few years into complete wire-free miniaturized modules, they still require further improvements to ensure totally unobtrusive monitoring architecture.

In this study, Ag/AgCl electrodes were used. An ECG traces the electrical potential differences between electrodes placed on the body's surface; however, the action potential that gives rise to the contraction and relaxation of the cardiac muscle is only about 1 mV, which is extremely difficult to measure. It is therefore necessary to amplify electrocardiographic data to make it easily perceivable to the human eye; this is done through the use of an operational amplifier (op-amp), which amplifies an input electrical potential in order to produce an output potential augmented to the level desired by the user. In this study, an instrumentation amplifier using op-amps was fabricated and configured to amplify the micro-fine ECG by a factor of about 100 using a band-pass filter (BPS). The current consumption of the proposed ECG sensor is about 11 mA and its noise generation is inversely proportional to the length of the wireless communication antenna inside the sensor.

2.2. Telemetry Methods

Currently used systems for health monitoring employ a variety of methods to relay information between the sensors and the data display module. Data are normally shared between these two units using wires, which increases the redundancy of the system and limits movement of the patient. Although wire-based equipment provides a robust means for communication in health monitoring systems and is low-cost, it reduces the ability for normal movement of a patient in her everyday routines.

Another problem arising in wired systems is the improper connection of wires for various reasons, which can seriously interrupt the system and pose serious consequences for the patient. Continuous improvisation and research is being carried out to develop smart health monitoring systems and many alternative communication techniques have emerged, with wireless communication being the most suitable communication method for curtailing the need for wired connections between sensors and equipment. Wireless technologies enable intra-body communication to complement systems for continual health monitoring without the need for admitting patients and attaching wires. Wireless communication allows for real-time monitoring of vital signs on an unwired display device in proximity to the patient as well as for remote observation by a doctor via the internet. Wireless connectivity can also help patients to track their own health indicators using smart-phones or PDAs connected to implants or wearable sensors in real-time. This can result in better health management and prompt alerts in the case of health related emergencies.

Biomedical implanting is a vibrant technology that has shown promise in improving real-time medical diagnostics. Research has shown that implants can be used to provide a feedback control; for example, an implant variant was used to record neural signals in brain–machine interfaces in order to control prostheses or paralyzed limbs, [6, 7]. Implants that use wireless communication have been shown to significantly reduce drawbacks attributed to wire connections, as has been reported with wired deep brain systems, implantable cardio-defibrillators, and pacemakers [8].

In this study, the medical Implant Communication Service (MICS) was used as a communications protocol. MICS operates in the frequency range of 402–405 MHz and is normally used for communication between body-worn monitoring systems and implants. Implantable antennas in this frequency range have been developed to transmit data from pacemakers and cardiac sensors; however, regulatory restrictions in hospitals have limited their full utilization in wireless body area networks (WBANs).

2.3. Wireless Power for Biomedical Implants

Supplying adequate power to bio-medical implants is currently the main challenge limiting functionality and performance in such devices. Power consumption affects many characteristics of an implant, including size, processing power, transmission range, and life span.

Batteries can power implants for long periods of time by exploiting design techniques that require extremely low power consumption. The average power consumption for a battery used in a pacemaker is about 8 μW and the typical battery comprises 90 % of the total size of the implant and requires periodic replacement through costly invasive surgery every few years [9, 10]. Power-hungry implants such as mechanical pump-based cardiac and orthopedic implants require significant amounts of power to function, making batteries an ineffective power source option for such implants [11, 12]. Thus, the prospects for and applicability of bio-medical implant technology are currently severely limited by the unavailability of adequate power sources, a problem that can be successfully addressed by using wireless power transfer techniques capable of delivering uninterrupted power to ensure continuous monitoring and communication by implants.

In this study, a near-field wireless power transmission system was used. It is assumed that the radiated fields produced by inductive coupling are not rapidly changing; as the displacement current at low frequencies does not affect the generated fields, it can be ignored. This is generally called the quasi-static approximation. Using this approximation, the magnetic field was found to be concentrated in the vicinity of the source. Problems such as these can be analytically solved using the Biot–Savart law or by finding a solution using the diffusion equation.

Many techniques for implementing coupled power links have been reported in the literature. In one study [13], the authors used coupled self-resonant coils to power a 60 W bulb over a distance of 2 m with an efficiency of 40 %. This was accomplished by non-radiating magnetic induction using resonant loops: employing two identical helical coils as coupling elements, a standard Colpitts oscillator with a single copper wire loop inductive element was used to generate frequencies in the MHz range. The copper loop coupled inductive power to the source coil for further transmission and a light-bulb served as the load of the power transfer system. Experimental results showed that power transfer using non-radiative magnetic coupling could be achieved over a range of 8~9 times the radius of the coils. The authors also presented a quantitative model with an accuracy of around 5% for explaining the power transfer.

2.4. Circuit Design

An ECG traces the electrical potential differences between electrodes placed on the surface of a body. However, the action potential that gives rise to the contraction and relaxation of the cardiac muscle is about 1 mV and thus extremely difficult to measure; in this design, operational amplifiers (op-amp) are used to amplify the electrocardiographic data. An op-amp amplifies an input electrical potential to the level desired by the user and produces an output potential augmented to this intended level. For this study an instrumentation amplifier was fabricated using op-amps and configured to amplify micro-fine ECG signals by a factor of about 100 using a band-pass filter (BPF). The proposed ECG sensor has a current consumption of about 11 mA and a noise generation inversely proportional to the length of the wireless communication antenna inside the sensor. Fig. 1.

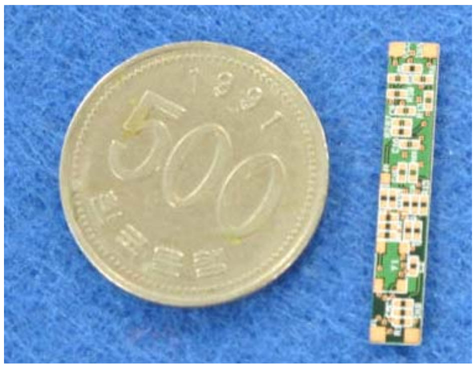

Fig. 1. Circuit design of implantable ECG sensor.

Shows the circuit design of the implantable ECG sensor.

2.5. Packaging

The packaging materials selected must be biocompatible to avoid causing inflammation or necrosis of human tissues. Additionally, they need to satisfy the strength standards of the insertion location and should not absorb electric waves passing through them. It is also necessary to take packaging design into account in order to avoid any risk of damage to tissues caused by sensor insertion and post-insertion movements. Foreign-body sensation needs to be minimized by reducing the size of the object. As feedthrough needs to meet several requirements, conductivity should be ensured between the internal circuit and electrodes, noise should be minimized, and air-tightness should be maintained. In this study, the elasticity of polymer films was exploited to develop electrode sealing methods.

ECG sensor electrodes must have an electrode-to-electrode distance of ≥40 mm, and an electrode width of ≥5 mm. In order to satisfy the requirements for electrodes, they were fabricated using titanium. The rigid packaging materials need to be coated to protect tissues and must be hermetically joined using a proper joining technique to completely block any interaction between the interior of the human body and the sensor environment; to accomplish this, either adhesives or a laser can be used. In this study, adhesives were used to produce a packaging prototype. Polydimethylsiloxane (PDMS) and medical epoxy are suitable adhesives, while PDMS, parylene, polyethylene, glycol, and silicone can be used as coating materials as their biocompatibilities have been verified in numerous studies. Fig. 2. shows the packaged implantable ECG sensor.

Fig. 2. Packaged implantable ECG sensor.

3. Experimental Results

3.1. Self-Sealing Air Tightness Testing

Testing for self-sealing air-tightness was performed in two steps. In the first step, the packaging was submersed in de-ionized (DI) water for one hour with no sensor included, and in the second test the packaging containing the sensor was submersed in DI water for five hours. Results of tests show that the materials joined with adhesives are air-tight. Fig. 3. shows the self-sealing test using the packaged sensor.

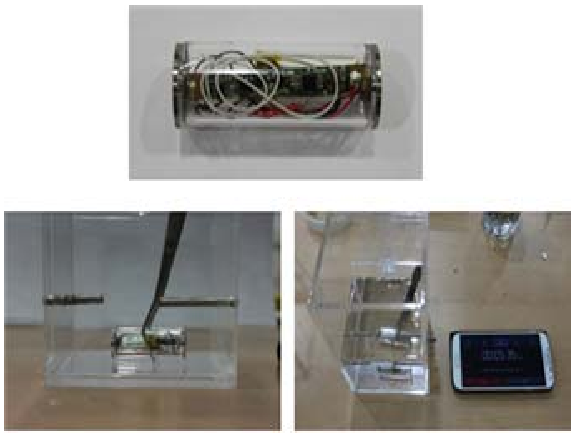

Fig. 3. Self-sealing test using the packaged sensor.

3.2. Thermal Testing

Coil charging was prepared in relation to the wireless power transmission to the ECG sensor. To establish a wireless network-driven environment for transmitting and receiving ECG data for measurement, a device was prepared that emitted an electric current identical to that of a real ECG and connected to the ECG sensor. An infrared temperature camera was then used to measure the temperature changes of the sensor itself; temperature changes were measured prior to the initiation of power transmission and then continued for one hour after transmission began with the aim of determining the average temperature change. Fig. 4 shows the thermal testing experimental setup.

Fig. 4. Thermal testing experimental setup.

From the experiments, we found that the baseline average temperature was 23.5 °C. The temperature then sharply rose by about 3.0 °C after about 10 minutes and continued to rise to reach 27.2 °C after one hour. As this temperature is far below 36.9 °C — the average temperature of the interior of the human body — it can be assumed that the packaged sensor will not undergo considerable temperature change once inserted into the human body.

3.3. Insertion Experiment Using Animal Model

Before using the sensor within a human body, it was necessary to test the in vivo safety of the instrument to ensure both the efficient operation of the insertion-type ECG measurement system in measuring physiological functions and its efficacy in receiving external signals. A pig was therefore used as a sensor-implanted animal model because the animal's physiological characteristics are similar to those of humans. The species selected was a Hanford mini pig because its heart size is very similar to that of a human. A female pig of specific pathogen free (SPF) quality with no history of pregnancy, 46–60 kg, and 50–57 weeks old, was purchased from Optipharm Medipig (Choongbuk, South Korea).

Fig. 5. Insertion experiment using animal model

The insertion surgery was performed in the Daegu High-Tech Medical Complex as follows. Anesthesia was induced using Zoletil (Tiletamine/Zolazepam) (2.5 mg/kg, IM) and Xylazine (2.3 mg/kg, IM) and maintained with Isoflurane (1–3 %). Lactated ringer's solution (5 ml/kg/h, IV) was administered intraoperatively. After the anesthesia, the left anterior corselet was depilated and disinfected with alcohol and povidone. An incision was made between the left 5th–7th ribs and separated using blunt dissection to a depth of 4 mm under the skin. The sensor was placed at the site, and the skin was sutured. On completion of the wireless ECG sensor implantation, the pig's ECG data were received by wireless network, as shown in Fig. 6.

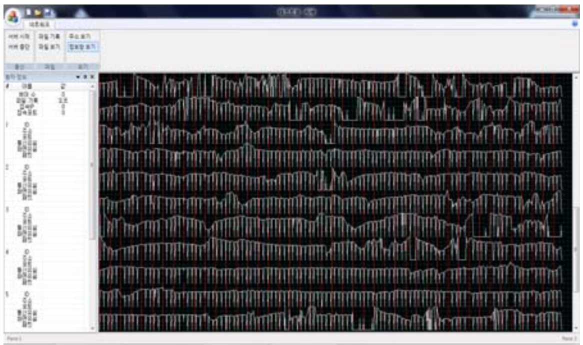

Fig. 6. ECG monitoring results using animal model.

4. Conclusion

This study demonstrated that the use of a quasi-permanent ECG employing a double loop coil-shaped magnetic resonance-type wireless power transmission system sensor eliminates the need for surgical replacement. An ultra-small antenna (20 mm in width, 10 mm in length) with a spiral-shape metal pattern was developed and used to minimize sensor size while securing a sufficient electric length. A human body phantom that had similar electrical properties to that of human skin within the MICS band, with a 10 % error range of measurement values (specific permittivity = 43.2, conductivity = 0701 S/m) was developed and used to verify the communication performance of the antenna. The hermetic joining of packaging using adhesives and biocompatibility were also experimentally verified. Finally, sensor insertion surgery was performed on a laboratory pig and successful ECG data were obtained via a wireless network.

Acknowledgements

This research was supported by the Bisa Research Grant of Keimyung University in 2017.

References

[1] Hao, Y., Foster, R., Wireless body sensor networks for health-monitoring applications, *Physiological Measurements*, 29, 2008, pp. R27–R56.

[2]. Newman, J. D., Turner, A. P. F., Home blood glucose biosensors: A commercial perspective, *Biosensors and Bioelectronics*, 20, 2005, pp. 2435–2453.

[3]. Recommended Practice for determining the spatial-peak specific ab-sorption rate (SAR) in the human body due to wireless communications devices: measurement techniques, *IEEE Standard 1528/D1.2,* 2003.

[4]. Pantelopoulos, A., Bourbakis, N. A., Survey on Wearable sensor-based systems for health monitoring

and prognosis, *IEEE Transactions on Systems Man and Cybernetics,* 40, 2010, pp. 1–12.

[5]. Malmivuo, J., Plonsey, R., Bioelectromagnetism, *Oxford University Press*, New York, USA, 1995.

[6]. Zimetbaum, P. J., Josephson, M. E., The evolving role of ambulatory arrhythmia monitoring in general clinical practice, *Annals of Internal Medicine*, 130, 1999, pp. 848–856.

[7]. Bergey, G. E., Squires, R. D., Sipple, W. C., Electrocardiogram recording with pasteless electrodes, *IEEE Transactions of Biomedical Engineering,* BME-18, 1971, pp. 206–211.

[8]. Searle, A., Kirkup, L., A direct comparison of wet, dry and insulating bioelectric recording electrodes, *Physiological Measurements*, 21, 2000, pp. 271–283.

[9]. Cho, G., Jeong, K., Paik, M. J., Kwun, Y., Sung, M., Performance evaluation of textile-based electrodes and motion sensors for smart clothing, *IEEE Sensors Journal*, 11, 12, 2011, pp. 3183-3193.

[10]. Muhlsteff, J., Such, O., Dry electrodes for monitoring of vital signs in functional textiles, in *Proceedings of the 26th IEEE Annual International Conference on Engineering in Medicine and Biology Society (IEMBS '04),* San Francisco, CA, USA, 2004, pp. 2212–2215.

[11]. Matthews, R., McDonald, N. J., Fridman, I., Hervieux, P., Nielsen, T., The invisible electrode zero prep time, ultra low capacitive sensing, in *Proceedings of the 11th International Conference on Human-Computer Interaction,* Las Vegas, NV, USA, 2005, pp. 22–27.

[12]. Chi, Y. M., Cauwenberghs, G., Wireless Non-contact EEG/ECG Electrodes for Body Sensor Networks, in *Proceedings of 2010 International Conference on, Body Sensor Networks (BSN)*, Biopolis, Singapore, 2010, pp. 297–301.

[13]. Droitcour, A. D., Boric-Lubecke, O., Lubecke, V. M., Lin, J., Kovacs, G. T. A., Range correlation and I/Q performance benefits in single-chip silicon Doppler radars for noncontact cardiopulmonary monitoring, *IEEE Transactions on Microwave Theory and Techniques,* 52, 2004, pp. 838–848.

First International Conference on Optics, Photonics and Lasers OPAL' 2018

2018 OPAL

9-11 May 2018
Barcelona, Spain
http://www.opal-conference.com

OPAL 2018 will incorporate the following three symposiums covering a broaden range in optics, photonics and lasers, and provide an excellent opportunity to exchange ideas and present latest advancements in these areas. The OPAL 2018 will be organized by IFSA in technical cooperation with The Institute of Photonic Sciences (ICFO) and Universitat Politècnica de Catalunya (UPC), Barcelona, Spain.

The conference is focusing any significant breakthrough and innovation in optics, photonics, lasers and its applications

- Optical and Fibre Optical Sensors and Instrumentation
- Micro-Opto-Electro-Mechanical Systems (MOEMS)
- Physical Optics
- Optoelectronic Devices, Photonics, Nanophotonics and Biophotonics
- Organic Optoelectronics and Integrated Photonics
- Optical Communications, Switching and Networks
- High-speed Opto-electronic Networking
- Optical Fiber Technology: Materials, Devices and Systems
- Optical Information Processing
- Holography
- Optical Metrology
- Optical Imaging Systems and Machine Vision
- Optical Computing
- Guided Wave Optics
- Optics in Condensed and Soft Matter
- Quantum Optics
- Lasers and Laser Applications
- Nonlinear Optics
- Nano and Micro Optics
- Matter Waves
- Quantum Information
- Bio and Medical Optics
- Optical Materials, Characterization Methods and Techniques
- Optical Methods for Process Control
- Microscopy and Adaptive Optics
- Lasers in Medicine and Biology
- Engineering Applications of Spectroscopy
- Optical Microscopy of Composites

Special Sessions:

Authors are welcome to organize and manage special sessions during the conference. Each session will contain 4-6 papers in a related field as specified above.

IFSA

Deadlines:

Submission (2-page abstract):	30 January 2018
Notification of acceptance:	28 February 2018
Registration:	15 March 2018
Camera ready (4-6 pages paper):	30 March 2018

Contribution Types:

Keynote presentations
Invited presentations
Regular papers
Posters

One event - three publications !

1. All registered abstracts will be published in the conference proceedings.
2. Selected extended papers will be published in Sensors & Transducers journal.
3. The best full-page papers will be recommended to extend to book chapters for 'Advances in Optics: Reviews' Book Series.

Chairman:

Prof., Dr. Sergey Y. Yurish (IFSA, Spain)

Advisory Chairmen:

Dr. Qiang Wu (Northumbria University, Newcastle Upon Tyne, UK)
Prof., Dr. Mahmoud Daoudi (National Center for Nuclear Sciences and Technologies, Tunisia)

Conference Manager:

Mrs. Tetyana Zakharchenko
(IFSA Publishing, S.L., Spain)

Theory:

Digital Sensors and Sensor Systems: Practical Design

and

Practice:

Development Board EVAL UFDC-1/UFDC-1M-16

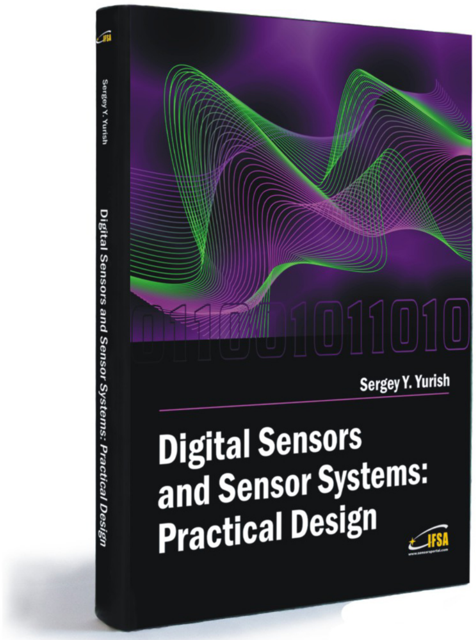

+

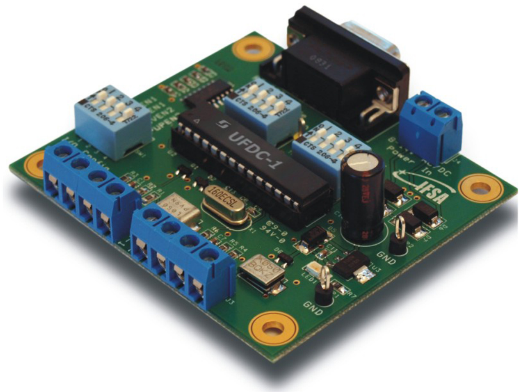

Buy book and Evaluation board together. **Save 30.00 EUR**

Development Board EVAL UFDC-1 / UFDC-1M-16

Full-featured development kit for the Universal Frequency-to-Digital Converters UFDC-1 and UFDC-1M-16. 2 channel, 16 measuring modes, high metrological performance, RS232/USB interface, master and slave communication modes. On-board frequency reference (quartz crystal oscillator). Operation from 8 to 14 V AC/DC. Development board software is included.

All existing frequency, period, duty-cycle, time interval, pulse-width modulated, pulse number and phase-shift output sensors and transducers can be directly connected to this 2-channel DAQ system. The user can connect TTL-compatible sensors' outputs to the Development Board, measure any output frequency-time parameters, and test out the sensor systems functions.

Applications:

- Digital sensors and sensor systems
- Smart sensors systems
- Data Acquisition for frequency-time parameters of electric signals
- Frequency counters
- Tachometers and tachometric systems
- Virtual instruments
- Educational process in sensors and measurements
- Remote laboratories and distance education

Order online:
http://www.sensorsportal.com/HTML/BOOKSTORE/Digital_Sensors_and_Board.htm

IFSA

International Frequency Sensor Association Publishing

www.sensorsportal.com

ISSN 1726- 5479

9 771726 547001